UNIVERSITÉ DE SHERBROOKE

Faculté de génie

Département de génie civil

Axial-flexural Performance of HSC Columns Reinforced with GFRP and BFRP Bars and Ties

Étude du comportement de colonnes en béton à haute résistance armé d'armature longitudinale et latérale en matériaux composites de PRFV et PRFB soumises à des charges axiales et de flexion

Thèse de doctorat

Spécialité : génie civil

Ashraf Salah-Eldin Mohamed

Sherbrooke (Québec) Canada

June 2019

MEMBRES DU JURY

Prof. Brahim BENMOKRANE

Directeur

Prof. Omar CHAALLAL

Évaluateur

Prof. P. VIJAY

Évaluateur

Prof. Charles-Philippe LAMARCHE

Rapporteur

ABSTRACT

Fiber-reinforced-polymer (FRP) bars are considered as alternative to steel bars to avoid corrosion problems and ensure that structures lave long service lives. Using high-strength concrete (HSC) with glass-fiber-reinforced polymer (GFRP) and basalt-fiber-reinforced polymer (BFRP) as internal reinforcement can allow designers to reduce member size and increase the structure's life span. Given HSC's brittle nature, its use-especially in columns-should be investigated to prevent undesirable brittle failure. This research takes charge of providing experimental database as well as comparing the results with normal strength concrete (NSC) columns with similar dimensions tested in the literature. The main objective of this research is to investigate the structural performance of HSC columns reinforced with FRP under eccentric loading. Full-scale columns were tested under monotonic loading with different levels of eccentricity. Test variables included eccentricity to depth ratio; reinforcement type (GFRP and Basalt FRP vs. steel); concrete strength (HSC vs NSC) and longitudinal reinforcement ratio. All specimens measured 400 × 400 mm square cross section and 2000 mm height.

The experimental results are reported in terms of axial load-deflection behavior, mode of failure, maximum tensile and compressive strains developed in rebars and moment-curvature. The test results showed that HSC can be effectively integrated with both GFRP and BFRP reinforcement with HSC and the specimens reached their peak strength with no damage to GFRP or BFRP rebar on either side of the tested specimens. Using HSC allowed the columns to reach higher peak load and develop higher tensile strain in the rebars compared to columns made with NSC. Columns reinforced with GFRP or BFRP behaved in a similar manner at all the tested levels of eccentricity. The failure of FRPRC columns were classified into three different zones depending on the curvature achieved at the peak load. Moreover, an analytical model has been developed by using a layer-by-layer approach to predict the axial-flexural interaction diagram and the moment-curvature relationship for square FRP-RC columns using different concrete strengths. The model predictions were in a good agreement with the experimental results.

Keywords: concrete, FRP bars; square; HSC; columns; axial-flexural strength; Moment-curvature; Basalt.

RÉSUMÉ

Les barres d'armature en polymère renforcé de fibres (PRF) sont considérées comme une alternative aux barres d'armature en acier face aux problèmes de corrosion, afin de garantir aux structures une longue durée de vie utile. L'utilisation de béton à haute résistance (BHR) avec des barres d'armature en polymère renforcé de fibres de verre (PRFV) et en polymère renforcé de fibres de basalte (PRFB) comme armatures internes peut permettre aux concepteurs de réduire la taille des éléments et d'augmenter la durée de vie des structures. Étant donné la fragilité du BHR, son utilisation en particulier dans les poteaux doit être étudiée afin d'éviter une rupture fragile indésirable. Ce projet de recherche a pour objectif de fournir une base de données expérimentales et de comparer les résultats expérimentaux aux résultats de poteaux en béton de résistance normale (BRN), de dimensions similaires rapportés dans la littérature. L'objectif principal de ce projet de recherche est d'étudier les performances structurales de poteaux en BHR armé d'armatures en PRF et soumis à un chargement excentrique. Des poteaux pleine grandeur ont été testés sous chargement monotone avec différentes excentricités. Les paramètres d'essais comprenaient le rapport excentricité/côté, le type d'armature (PRFV, PRFB, acier), la résistance en compression du béton (BHR, BRN) et le taux d'armature longitudinal. Tous les spécimens avaient une section transversale carrée de 400 x 400 mm une hauteur de 2000 mm.

Les résultats expérimentaux sont présentés selon le comportement charge axiale – flèche, les modes de rupture, les déformations maximales en traction et en compression développées dans les barres d'armature et la réponse moment-courbure. Les résultats des essais ont montré que le BHR peut être utilisé efficacement avec les armatures en PRFV et en PRFB et que les spécimens ont atteint leur résistance maximale sans endommagement des armatures en PRFV ou en PRFB des deux côtés des spécimens testés. L'utilisation du BHR a permis aux poteaux d'atteindre une charge maximale plus élevée et de développer une déformation en traction plus élevée dans les barres d'armature par rapport aux poteaux fabriqués avec du BRN. Les poteaux avec armatures en PRFV et en PRFB ont eu des comportements similaires pour les mêmes niveaux d'excentricités. La rupture des poteaux en béton armé de PRF a été classée en trois zones différentes en fonction de la courbure correspondante à la charge maximale. De plus, un modèle analytique a été développé en utilisant une approche couche par couche pour prédire le diagramme d'interaction et la réponse

moment-courbure des poteaux carrés en béton de différentes résistances en compression armé de PRF. Les prévisions du modèle concordent bien avec les résultats expérimentaux.

Mots clés : béton, barres d'armature de PRF ; section carrée ; BHR ; poteaux ; résistance à la flexion axiale ; moment-courbure ; basalte.

ACKNOWLEDGEMENTS

All praise and gratitude be to ALLAH the Most Gracious, the Most Merciful. With utmost gratitude, I wish to express my deep gratitude to everyone who made this research possible. The author is indebted to prof. Brahim BENMOKRANE for his supervision, guidance and constructive criticism throughout all stages of the research program. His encouragement and willingness to help in every possible way is greatly appreciated.

I am also very grateful to Dr. Hamdy Mohamed for the encouragement to pursue this topic, his valuable assistance with planning, experimental work, testing and analysis, and for the countless hours of discussions on the subject and guiding me through this process and his continuous support for me and his patience.

Moreover, I would like to express the special thanks and gratitude to the Natural Science and Engineering Research Council of Canada (NSERC), the NSERC Industrial Research Chair in FRP Reinforcement for Concrete Infrastructure, the Tier-1 Canada Research Chair in Composite Materials for Civil Structures, and the Fonds de la recherche du Quebec–Nature et Technologie – (FRQ-NT) for funding this research. Also, I would like to thank TUF-BAR Canada for providing the GFRP reinforcement and the technical staff of the Structural and Materials Lab in the Department of Civil Engineering at the University of Sherbrooke.

TABLE OF CONTENTS

ABSTRACT ..... **I**

RÉSUMÉ ..... **III**

ACKNOWLEDGEMENTS ..... **I**

TABLE OF CONTENTS ..... **II**

LIST OF TABLES ..... **VII**

LIST OF FIGURES ..... **VIII**

CHAPTER 1 INTRODUCTION **1**

1.1. GENERAL BACKGROUND 1

1.2. OBJECTIVES AND SCOPE 2

1.3. METHODOLOGY 3

1.4. THESIS ORGANIZATION 4

CHAPTER 2 LITERATURE REVIEW **5**

2.1. GENERAL 5

2.2. BACKGROUND 5

2.2.1. History of FRPs *5*

2.2.2. Behaviour of FRP bars: *6*

2.2.3. The physical and mechanical properties *7*

2.3. BEHAVIOR OF HSC 9

2.3.1. Stress strain behavior in compression *10*

2.3.2. Elastic modulus *12*

2.3.3. Poisson's ratio *12*

2.4. GFRP REINFORCED COLUMNS 13

CHAPTER 3 EXPERIMENTAL WORK **24**

3.1. INTRODUCTION 24

3.1.1. General *24*

3.2. OBJECTIVES 25

3.3. EXPERIMENTAL PROGRAM 25

3.1.1 Proposed test parameters *25*
3.1.2 Material properties *26*
3.4. SPECIMEN DESIGN 29
3.5. SPECIMENS PRODUCTION 29
3.5.1. Cage Assembling *29*
3.5.2. Instrumentation *31*
3.5.3. Formwork construction *32*
3.5.4. Concrete casting *32*
3.5.5. Test setup *33*

CHAPTER 4 FULL-SCALE HIGH STRENGTH CONCRETE COLUMNS REINFORCED WITH GFRP BARS AND TIES SUBJECTED TO ECCENTRIC LOADS 35

4.1. INTRODUCTION: 36
4.2. OBJECTIVES: 39
4.3. MATERIALS 39
4.3.1. GFRP reinforcement *39*
4.3.2. Steel reinforcement *40*
4.3.3. Concrete properties *40*
4.4. STRESS-STRAIN RELATIONSHIP FOR HSC: 42
4.5. CONSTRUCTION METHOD: 42
4.6. SPECIMEN DESIGN: 43
4.7. TEST SETUP AND INSTRUMENTATION 44
4.8. TEST RESULTS AND OBSERVATIONS: 45
4.8.1. Cracking pattern: *45*
4.8.2. Axial and lateral deformation: *50*
4.8.3. Concrete strain: *52*
4.8.4. Longitudinal GFRP-bar strain profiles: *53*
4.9. DISCUSSION 56
4.9.1. Influence of test parameters *56*
4.9.2. Efficiency of using high strength concrete: *56*
4.9.3. Eccentricity to depth ratio *57*
4.9.4. Reinforcement type: *58*
4.10. EXPERIMENTAL P-M INTERACTION DIAGRAMS: 59
4.11. THEORETICAL PREDICTION: 60
4.11.1. Development of theoretical interaction diagrams: *63*
4.12. COMPARING THE EXPERIMENTAL AND THEORETICAL RESULTS: 64

4.13. PARAMETRIC INVESTIGATION: 65
4.13.1. Effect of increasing the longitudinal reinforcement ratio: 65
4.13.2. Effect of the concrete strength: 65
4.13.3. Effect of ignoring the contribution of bars in compression: 66
4.14. CONCLUSIONS: 68

CHAPTER 5 AXIAL–FLEXURAL PERFORMANCE OF HSC BRIDGE COMPRESSION MEMBERS REINFORCED WITH BFRP BARS AND TIES: EXPERIMENTAL AND THEORETICAL INVESTIGATION 71

5.1. ABSTRACT 71
5.2. INTRODUCTION 72
5.3. ADVANCES IN RESEARCH ON BFRP-REINFORCED CONCRETE MEMBERS 74
5.4. AIMS AND OBJECTIVES OF THE STUDY 75
5.5. EXPERIMENTAL WORK 76
5.5.1. Material Properties 76
5.5.2. Concrete 78
5.5.3. Test Specimens 79
5.5.4. Instrumentation and Test Setup 80
5.6. TEST RESULTS AND OBSERVATIONS 82
5.6.1. Low Eccentricity (e = 80 mm) 83
5.6.2. High Eccentricity (e = 240mm). 87
5.7. DISCUSSION 91
5.7.1. Effect of Test Parameters 91
5.7.2. Initial Eccentricity and Induced Moment 92
5.7.3. Efficiency of Using HSC 93
5.7.4. Reinforcement Type 94
5.8. THEORETICAL ANALYSIS 96
5.8.1. Experimental and Theoretical Development of the P–M Interaction Diagrams 96
5.8.2. Theoretical Prediction of P-M Interaction Diagrams 97
5.8.3. Comparing the Experimental and Theoretical Results 100
5.8.4. Parametric Investigation 101
5.9. MOMENT–CURVATURE BEHAVIOR 104
5.10. DUCTILITY 105
5.11. EFFECTIVE FLEXURAL STIFFNESS (EI_{SEC}) 106
5.12. COMPARATIVE STUDY ON DIFFERENT ESTIMATIONS OF SECTION FLEXURAL STIFFNESS 107
5.13. HYBRID COLUMNS 109
5.14. CONCLUSIONS 110

CHAPTER 6 EFFECT OF GFRP-REINFORCEMENT RATIO ON THE STRENGTH AND EFFECTIVE STIFFNESS OF HIGH-STRENGTH CONCRETE COLUMNS: EXPERIMENTAL AND ANALYTICAL STUDY 113

6.1. ABSTRACT 113
6.2. INTRODUCTION 114
6.3. RESEARCH SIGNIFICANCE 116
6.4. EXPERIMENTAL INVESTIGATION 117
6.4.1. Materials 117
6.4.2. Specimen Design and Fabrication 118
6.4.3. Instrumentation 120
6.5. OBSERVED BEHAVIOR AND TESTS RESULTS 122
6.5.1. Cracking and Failure Modes 122
6.5.2. Concrete and GFRP-Bar Strain Behavior 125
6.6. DISCUSSION 128
6.6.1. Effect of Reinforcement Ratio 128
6.6.2. Effect of Compression Reinforcement 130
6.6.3. Effect of Using HSC 130
6.7. MOMENT–CURVATURE RELATIONSHIP 132
6.8. DUCTILITY 134
6.9. ANALYTICAL APPROACH 135
6.9.1. Modeling of the Materials 135
6.10. DEVELOPMENT OF THE M–Ψ RELATIONSHIP 136
6.10.1. Procedure to Determine Moment and Curvature 137
6.11. COMPARISON BETWEEN THE ANALYTICAL MODEL AND THE EXPERIMENTAL RESULTS 139
6.11.1. Effect of Reinforcement Ratio and Concrete Strength on the Column Effective Stiffness 139
6.11.2. Comparative Study on I_e/I_g 140
6.12. CONCLUSION 143

CHAPTER 7 SUMMARY, CONCLUSIONS AND RECOMMENDATIONS 145

7.1. SUMMARY 145
7.2. CONCLUSIONS 145
7.2.1. Strength, General Behavior and Failure Mode 146
7.2.2. Flexural Stiffness 148
7.2.3. Analytical Modelling 148
7.2.4. Parametric Investigations 149
7.3. RECOMMENDATIONS FOR FUTURE WORK 149
RÉSUMÉ 149

7.4. CONCLUSIONS 150
7.4.1. Résistance, comportement général et modes de rupture 150
7.4.2. Rigidité en flexion 153
7.4.3. Modélisation analytique 154
7.4.4. Études paramétriques 154
7.5. RECOMMANDATIONS POUR LES TRAVAUX FUTURS 154
REFERENCES 156

LIST OF TABLES

Table 2-1: Advantages and Disadvantages of FRP (ACI 440.1R-15) 6
Table 2-2: The average physical properties for the reinforcing bars* 7
Table 2-3*: The average tensile properties for the reinforcing bars* (ACI 440.1R-15) 8
Table 2-4: Poisson's ratio of HSC reported by different studies 13
Table 3-1 Mechanical properties of FRP bars* 27
Table 3-2: Mechanical properties of Steel bars* 28
Table 3-3: Test Matrix 30
Table 4-1 – Mechanical properties of GFRP and Steel reinforcement 40
Table 4-2– Concrete mix properties 41
Table 4-3 – Test matrix 43
Table 4-4– Test matrix and summary of results 46
Table 5-1 – Mechanical properties of the BFRP and steel reinforcement 78
Table 5-2 – Concrete mix properties 78
Table 5-3 – Specimen details. 80
Table 5-4 – Test matrix and summary of test results 83
Table 6-1– Mechanical properties of the GFRP reinforcement 117
Table 6-2– Test matrix 121
Table 6-3 – Summary of results 131

LIST OF FIGURES

Figure 1-1 – Flow chart of the research program 3
Figure 2-1– Comparison of stress-strain relationships for GFRP in tension or Compression, reinforcing steel, and plain concrete.(Tikka et al. 2013) 9
Figure 2-2– Stress strain curve for different concrete strength. (Wight and MacGregor (2009), reproduced from Whittaker (2012) 10
Figure 2-3– *Specimen detail, [XUE et al., 2014]* 19
Figure 3-1–GFRP and BFRP cages 27
Figure 3-2– Steel cages 28
Figure 3-3 – Instrumentation 31
Figure 3-4 – Form work used 32
Figure 3-5 – Concrete casting 33
Figure 3-6 – Test setup: a) elevation of test setup, b) 3d drawing of test setup, c) lower end cap and applied eccentricity and d) data acquisition system. 34
Figure 4-1 (a) Reinforcement details for column GFRP and steel reinforced columns. (b) overview of GFRP bars and ties. 41
Figure 4-2 – Test setup elevation and side view. 45
Figure 4-3 – Failure mode for group GFRP and steel reinforced columns series on tension side. 49
Figure 4-4 – Failure mode for group GFRP and steel reinforced columns series on compression side. 49
Figure 4-5 – Side view for the failure mode for group GFRP and steel reinforced columns series. 50
Figure 4-6 – Load versus axial displacement for GFRP and steel reinforced columns. 51
Figure 4-7 – Load versus lateral mid-height displacement. 52
Figure 4-8 – Load versus concrete strain on the compression side. 53
Figure 4-9 – Load versus outermost compressive bar strain at mid-height for GFRP and steel bars. 54

Figure 4-10 – Load versus outermost tensile bar strain at mid-height for GFRP and steel columns. 54
Figure 4-11 – Experimental results for GFRP and steel reinforced columns series. 60
Figure 4-12 – Strain profile at peak load for G series under different eccentricities. 61
Figure 4-13 – Stress and strain assumption for strip method analysis. 63
Figure 4-14 – Axial-Moment interaction diagram for experimental vs predicted results. 64
Figure 4-15 – Theoretical interaction diagram for square section (400×400) (a) considering te contribution of GFRP bars in compression (b) ignoring the contribution of GFRP bars in compression. 67
Figure 5-1 – Compression test for BFRP bars (a) test setup, (b) typical crushing failure, (c) stress–strain relationship for all the BFRP bars tested under compression, (d) average stress–strain used for tension and compression. 77
Figure 5-2 – (a) Configuration of BFRP- and steel-reinforced columns and reinforcement details and (b) overview of BFRP bars and ties. 82
Figure 5-3 – Overview of the test setup. 82
Figure 5-4 – Overview of cracking pattern for three sides of the tested columns. 85
Figure 5-5 – Load versus concrete strain on the compression side. 86
Figure 5-6 – Load versus axial displacement for the BFRP- and steel- reinforced columns. 86
Figure 5-7 – Load versus lateral displacement at mid-height. 87
Figure 5-8 – Load versus outermost bar strain at mid-height. 88
Figure 5-9 – Load versus outermost bar strain at quarter-height. 89
Figure 5-10 – Ties strains for columns tested with e = 80 mm. 90
Figure 5-11 – Ties strains for columns tested with e = 120 mm. 90
Figure 5-12 – Ties strains for columns tested with e = 160 mm. 91
Figure 5-13 – Ties strains for columns tested with e = 240 mm. 91
Figure 5-14 – Experimental results for (a) BFRP- and (b) steel-reinforced concrete columns. 95
Figure 5-15 – Strain profile for the BFRP-reinforced columns at peak load for the tested eccentricities. 97
Figure 5-16 – Stress and strain assumption for strip-by-strip method of analysis. 98
Figure 5-17 – Axial-moment interaction diagram for experimental vs predicted results. 101

Figure 5-18 – Theoretical interaction diagram for a square section (400×400 mm) (a) ignoring the contribution of the BFRP bars in compression and (b) considering the contribution of the BFRP bars in compression. 102
Figure 5-19 – Moment curvature for all BFRP-reinforced concrete columns at four different eccentricities. 105
Figure 5-20 – Influence of P/P_0 and *e/h* on the section stiffness (EI_{sec}/EI_g) for the tested BFRP-reinforced concrete columns. 106
Figure 5-21 – Comparing relative flexural stiffness of BFRP-reinforced concrete members using theoretical equations and experimental data (a) at the ultimate- and (b) service-load levels. 109
Figure 6-1 – Overview of the (a) GFRP cages and (b) GFRP bars, ties, and crossties used. 118
Figure 6-2– Dimension and details of four groups (G1, G2, G3, and G4T) 119
Figure 6-3 – Test setup. 122
Figure 6-4 – Failure mode for all the tested specimens for compression side, side view, and tension side, respectively 124
Figure 6-5 – Axial load–axial displacement at mid-height. 126
Figure 6-6 – Axial load–lateral displacement at mid-height. 126
Figure 6-7 – Axial load–reinforcement strain @ mid-height for series (a) G1, (b) G2, and (c) G3, and G4T. 126
Figure 6-8 – Strain profile for all the tested columns at peak load. 128
Figure 6-9 – Strength of the tested columns for series G1, G2, and G3 (a) Axial–flexural strength of columns; (b) axial load versus eccentricity-to-depth ratio. 129
Figure 6-10 – Comparison of the experimental and analytical M-ψ for series G1 and G2. 133
Figure 6-11 – Influence of changing the applied eccentricity and P/P_o on EI/EI_g for series G1 and G2. 134
Figure 6-12 – Stress and strain profiles of FRP-RC square cross section. 137
Figure 6-13 – Analytical study showing the effect of changing (a) reinforcement ratio ρ, and (b) concrete strength ($f_c^{'}$) on the relative flexural stiffness of FRPRC members as a function of eccentricity-to-depth ratio. 140
Figure 6-14 – Influence of changing the applied eccentricity and P/P_o on EI/EI_g for series G1 and G2. 143

CHAPTER 1 INTRODUCTION

1.1. General background

Concrete strength used in practice has been increasing gradually over the years. Recently, high strength concrete (HSC) were used in many application including precast elements, and different structural members such as beams and columns. HSC offers economy and superior performance when used in columns, piers and piles. Increased strength results in smaller member sizes while acquiring higher young's modulus. Additional benefits can also be realized through improved performance relative to durability and corrosion resistance.

Aggressive climate and environmental changes stimulate the manufacturing and industrial improvement of existing technology. Fiber-reinforced polymer (FRP) reinforcement have been introduced as a replacement to steel reinforcement to avoid corrosion. Past years have seen valuable research work and widespread applications of different concrete elements to increase the trust and further improve the FRP reinforcement. Integrating FRP reinforcement with HSC would result in more cost effective and durable structural elements. However, using FRP bars as reinforcement for HSC, especially in columns, is still a relevant issue to be addressed and not covered by design codes such as ACI 440.1R-15 and CSA S806. Moreover, the contribution of compressive FRP reinforcement in columns is questioned and under study. Only limited studies investigated the behavior of HSC columns reinforced with FRP under eccentric and concentric columns in which their findings demonstrated the feasibility of using FRP reinforcement in columns.

This research intended to originally examine the performance of FRP reinforcement with HSC columns/piles under eccentric compression to set the limits and the boundaries of using FRP bars under high compression forces developed by using HSC.

1.2. Objectives and Scope

This study investigates the behavior of high strength concrete columns reinforced with fiber reinforced polymer bars as a primary reinforcement under eccentric loading and to better determine its viability as a potential construction alternative. High strength concrete will be used to gain a better understanding of the performance of GFRP and BFRP reinforced full-scale concrete columns. The performance of FRP rebar and ties were compared to steel reinforcement. The behaviour of these columns were quantified by plotting interactions diagrams for axial-moment and axial deflection response analysis. The research also discussed the issue of considering the contribution of FRP rebar in the light of the data provided by the ACI 440.1R (2015), in which recommendations were drawn. The behavior of HSC columns was evaluated by comparing their behavior with similar columns with the same dimensions made with NSC. Moreover, the failure mechanism of these columns were also be identified and quantified. The behavior was also assessed by comparing the moment curvature behavior and flexural stiffness during loading. Ultimately, design recommendations will be developed to the use of FRP bars with high strength concrete.

The general objective of this study is:
Addressing the feasibility and applicability of FRP bars in eccentric columns and evaluating their behavior by comparing with steel reinforced column and columns made with NSC.

The following points summarized the specific objectives:

1. Investigating the behavior and failure mode mechanisms of GFRP-RC and BFRP-RC columns subjected to combined flexural moment and compression load.
2. Developing interaction diagrams for GFRP and BFRP-RCC members experimentally.
3. Correlating strength predictions with the experimental results yielded by adopting layer by layer method.
4. Determining the effective stiffness of the tested specimens and compared with the available expressions.

1.3. Methodology

To achieve the above-described objectives, a research plan including experimental program and theoretical studies was conducted. The experimental program included testing of full-scale circular members reinforced with glass and carbon FRP as well as steel reinforcement. The results were discussed in terms of general behavior, effect of test parameters, and interaction diagrams. On the other side, theoretical studies were prepared to analytically develop the interaction diagrams of the tested specimens along with parametrical investigation. The stress block parameters of HSC members were also investigated. Moment - curvature relationships were developed using through an analytical model to predict and propose expressions for the effective stiffness. The following flow chart, Fig 1.1, summarized the methodology prepared for this work.

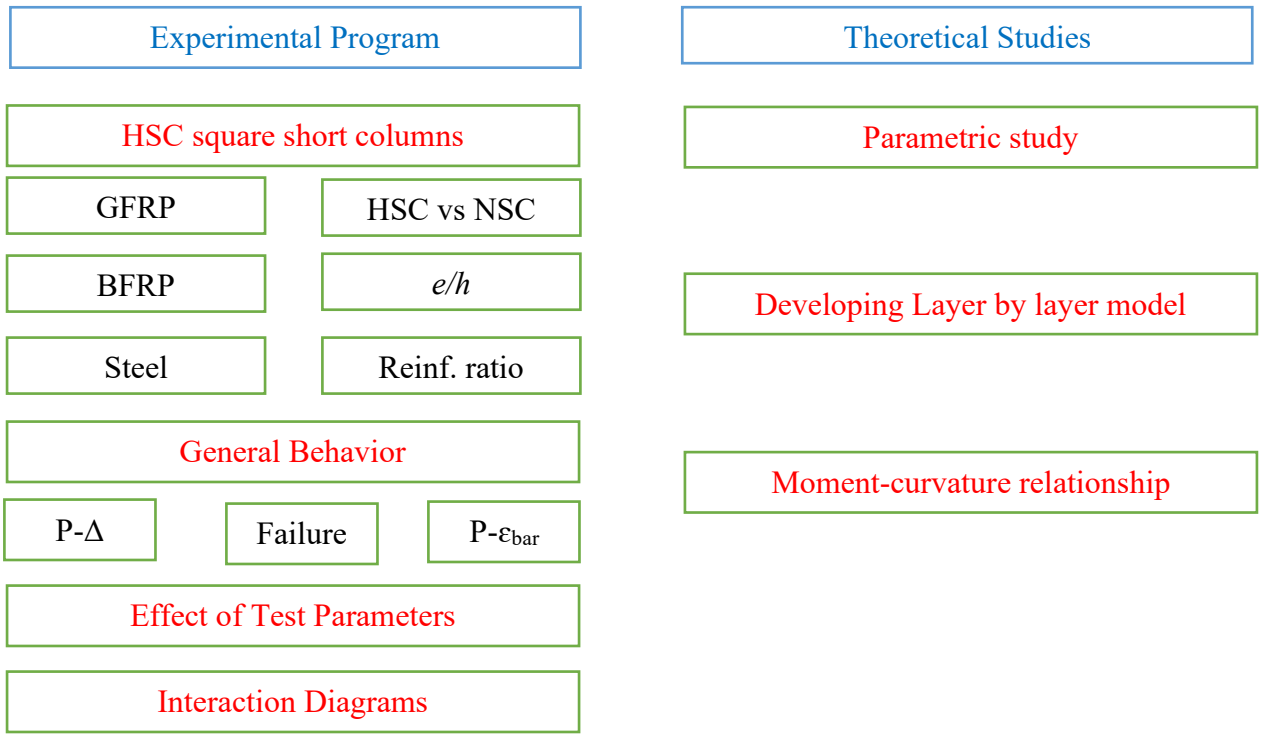

Figure 1-1 – Flow chart of the research program

1.4. Thesis organization

The thesis first begins commonly with a short review in Chapter 2 of presenting pertinent studies to this work in a chronological order.

Chapter 3 (1st article) presents the results of an experimental investigation on the eccentric behavior of square GFRP-RC HSC column. The axial force–moment interaction diagrams were predicted using layer by layer method and internal force equilibrium and following the recommendations of the available design standards/guidelines and recent research work on GFRP-RC columns.

Chapter 4 (2nd article) presents test results of an experimental program to investigate the structural performance of square HSC-RC columns reinforced with basalt-FRP (BFRP) bars and ties. Based on the test results, a detailed sectional analysis and plane section analysis were then conducted. Furthermore, a comprehensive parametric investigation was performed to generate numerous nominal axial force-bending moment interaction diagrams and investigate the effective stiffness response of the tested columns.

Chapter 5 (3rd article) presented a state-of-art review on the compressive-strength contribution of GFRP reinforcement. The lowest and highest bounds of the mechanical properties of GFRP reinforcement reported in the ACI 440.1R (2015) were included in analytical study employing different concrete strengths and reinforcement ratios to develop sets of axial force–bending moment interaction diagrams and indicative guide charts. In addition, the minimum GFRP longitudinal reinforcement ratio to prevent tension failure (GFRP-bar rupture) was investigated.

Chapter 6 presents summary, conclusions, and the recommendations for future study.

CHAPTER 2 LITERATURE REVIEW

2.1. General

This chapter provides a brief summary of the main characteristics and properties of the Fiber reinforced polymer (FRP) materials used as internal reinforcement. This is followed by a demonstration of the main studies that investigated the axial and axial-flexural behavior of concrete columns reinforced with FRP bars. The code provision that related to flexural behavior and serviceability of FRP reinforced concrete members are also presented.

2.2. BACKGROUND

2.2.1. History of FRPs

FRP composites are results of the idea of making better composite materials by combining different materials (Nanni, 1999), that can be traced back to the utilizing of straw in bricks as reinforcement. In early 1950's composite materials were used in automotive and aerospace industry as a light weight material with acceptable stiffness and strength. In 1960's these materials were considered for use as reinforcement of concrete in high way bridges as a replacement to conventional steel reinforcements which experience extensive corrosion as a result of applying deicing salt or being exposed to marine environment (almost 10% of the high way bridges in US are structurally deficient or functionally no longer in use, ASCE report card 2005). The FRP reinforcing bar was introduced on the market in the late 1970's as a viable alternative to steel as reinforcement for concrete due to the incompatibility of thermal expansion characteristics between polymer concrete and steel.

2.2.2. Behaviour of FRP bars:

The mechanical properties of FRP bas are quite different from those of steel bars and depend mainly on both matrix (resin) and fibers type as well as volume fraction. The fibers include aramid, polyvinyl, carbon and improved glass fibers. Table 2.1 lists some of the advantages and difference between FRP reinforcement compared to conventional steel reinforcement, as reported by ACI 4401R-15.

Table 2-1: Advantages and Disadvantages of FRP (ACI 440.1R-15)

Advantages of FRP reinforcement	**Differences between steel and FRP**
High longitudinal tensile strength (varies with sign and direction of loading relative to fibers)	FRP is linear elastic to failure whereas steel yields
Corrosion resistance (not dependent on a coating)	Low transverse strength (varies with sign and direction of loading relative to fibers)
Non magnetic	Low modulus of elasticity (varies with type of reinforcing fiber), that's why design for serviceability often controls
High fatigue endurance (varies with type of reinforcing fiber)	Susceptibility of damage to polymeric resins and fibers under ultraviolet radiation exposure
Lightweight (about 1/5 to 1/4 the density of steel)	Low durability of glass fibers in a moist environment
Low thermal and electric conductivity (for glass and aramid fibers)	Low durability of some glass and aramid fibers in an alkaline environment
	High coefficient of thermal expansion perpendicular to the fibers, relative to concrete
	Endurance time in fire is less than the steel depending on matrix type and concrete cover thickness

2.2.3. The physical and mechanical properties

The density and coefficient of thermal expansion have a significant effect on the material use. The density of the material directly affects the cost and ease of transportation and also the workability. FRP bars have density ranging from one fifth to one forth than that of steel; this makes the FRP easier in handling and weight much less than steel bars (ACI committee 440, 2001).

The longitudinal coefficient of thermal expansion is dominated by fiber properties while the transverse coefficient is dominated by resin. Typical values for the coefficient of thermal expansion in longitudinal and the transverse directions are reported in Table 2.2. The higher value for the transversal coefficients of thermal expansions combined with the Poisson's effect in the case of compressed reinforcement can be responsible for circumferential tensile strength that causes the formation of cracks in the radial direction that may weakens the concrete-FRP bond.

Table 2-2: The average physical properties for the reinforcing bars*

Material	Density (Kg/m3)	Coefficient of thermal expansion	
		Longitudinal (α_L)	Transversal (α_T)
Steel	7900	$11.7x10^{-6}$ □c	$11.7x10^{-6}$ □c
GFRP	1700	$8x10^{-6}$ □c	$22x10^{-6}$ □c
CFRP	1600	$-5x10^{-6}$□□c	$90x10^{-6}$ □c
AFRP	1300	$-4x10^{-6}$ □c	$70x10^{-6}$ □c

*The negative sign in the coefficient of thermal expansion means a contraction action.

The **tensile**, **compressive**, **shear** and **bond** strengths have a great importance on the structural behavior. It should also be noted that the manufacturing quality control affects the mechanical characteristics of the bar [Wu 1990]. The tensile properties of FRP are what make them a good alternative to steel reinforcement. FRP bars don't exhibit any plastic behavior (yielding) before rupture. Table 2.3 summarizes the average properties of the material.

FRPs bar have an anisotropic and brittle failure behavior which means that it has a linear stress-strain behavior under tension up to failure, however, they have lower modulus of elasticity compared to steel bars. Figure 2.1 shows stress-strain curves for different types of FRP bars.

It is not recommended to rely on FRP bars to resist **compressive** stresses (ACI-440-1R-06). Tests on FRP bars with a length-diameter ratio from 1:1 to 2:1 have shown that the compressive strength is lower than the tensile strength [Wu 1990]. Compressive strengths of 55, 78, and 20% of the tensile strength have been reported for GFRP, CFRP, and AFRP, respectively [Mallick 1988; Wu 1990]. Higher compressive strengths are expected for bars with higher tensile strength [ACI 1995]. According to reports, the compressive modulus of elasticity is approximately 80% for GFRP, 85% for CFRP, and 100% for AFRP of the tensile modulus of elasticity for the same product [Mallick 1988; Ehsani 1993]. Standard test methods are not yet established to characterize the compressive behavior of FRP bars but a testing method for FRP materials is given by [Benmokrane et al., 1998].

Table 2-3: The average tensile properties for the reinforcing bars (ACI 440.1R-15)

Properties	Steel	GFRP	CFRP	AFRP
Nominal yield stress, MPa	276 to 517	N/A	N/A	N/A
Tensile strength, MPa	483 to 1600	483 to 690	600 to 3960	1720 to 2540
Elastic modulus, GPa	200	35 to 51	120 to 580	41 to 125
Yield strain, percent	0.14 to 0.25	N/A	N/A	N/A
Rupture strain, percent	6.0 to 12.0	1.2 to 3.1	0.5 to 1.7	1.9 to 4.4

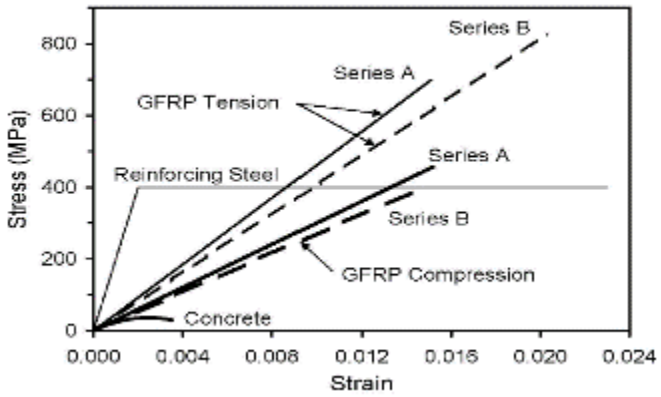

Figure 2-1– Comparison of stress-strain relationships for GFRP in tension or Compression, reinforcing steel, and plain concrete.(Tikka et al. 2013)

Most FRP bars composites are relatively weak in inter-laminar shear where layers of unreinforced resin lie between layers of fibers. The inter-laminar shear strength is governed by relatively weak polymer matrix as there is no reinforcement across layers. One of the ways to increase the shear strength is by providing braiding or winding fibers transverse to the main fibers, depending on the orientation of the fibers in an off-axis direction will increase the shear resistance.

2.3. Behavior of HSC

The use of high strength concrete (HSC) for bridges and high rise buildings have become very popular due to development in concrete technology and the availability of new mineral and chemical admixtures such as silica fume, fly ash and super plasticizers. HSC is often used to reduce the structural member size for compression members and therefore provide considerable savings. Furthermore, due to the superior durability if HSC, significant reduction of the maintenance requirements and an increase in the service life of the structure can be achieved.

The definition of HSC has varied over time. For instance, in the 1950's concrete with a compressive strength of 5000psi (34 MPa) was considered high strength concrete. In the early 1970s, 9000 psi (62 MPa) concrete was being produced. More recently, compressive strength approaching 20,000 psi (138MPa) was available at only a few locations.

Mechanical properties of HSC can be divided into two groups as short term and long term mechanical properties. Short term mechanical properties include compressive strength, stress strain behavior, elastic modulus, poisson's ratio, tensile strength and modulus of rupture. These properties are presented here from previous research work.

2.3.1. Stress strain behavior in compression

Stress-strain behavior of concrete for different range of compressive strength is shown in Figure 2.2. The slope of the ascending part of the tress-strain of HSC is steeper and linear than the NSC, strain at maximum strength is greater and the descending part is also steeper compared to NSC. Stress strain behavior of HSC depends in material properties such as water content and aggregate type, it also depends in experimental parameters that include strain rate, age at testing and interaction between testing machine and specimen.

Carrasquillo et al. (1981) reported that there is less internal micro cracking in HSC than NSC for the same axial strain imposed. This also indicates that HSC experience less lateral strain, and consequently effectiveness of confinement on compressive strength of HSC is often limited compared to NSC.

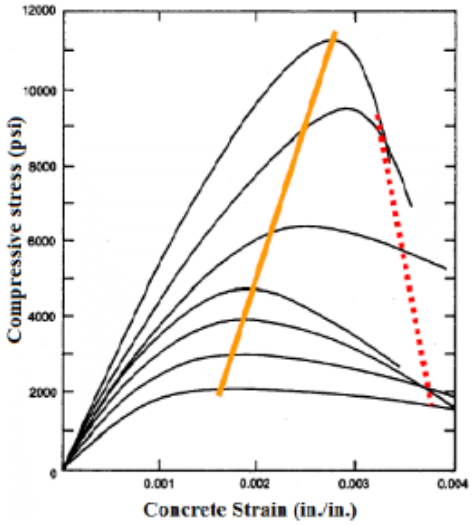

Figure 2-2– Stress strain curve for different concrete strength. (Wight and MacGregor (2009), reproduced from Whittaker (2012)

Compressive strength

Decreasing w/c ratio increases the strength of concrete. However, this trend is only valid as long as the strength of hydrated cement is low compared to the strength of coarse aggregates. When these two strengths become comparable, decreasing the w/c doesn't increase the strength of the concrete. In order to further increase the strength of HSC, strength and quality of HSC need to be increased. Typically, a water to cement ratio of 0.2-0.4 are used for HSC to hydrate all the cement particles in a concrete mixture. It was also experienced that adding mineral admixtures such as silica fume or fly ash increases the workability in HSC. Irvani (1996) noted that effect of silica fume on High strength development of HSC is most prominent during 7 to 28 days.

HSC has higher rate of strength gain at earlier stage compared to NSC as shown in (Carrasquillo et al.,1981). There is no significant increase in strength after 28 days, 10 to 15% increase in strength is gained at age of 56 days and 95 days compared to 28 days strength. Curing of HSC has a strong influence on the strength development because of its low w/c ratio. Testing age of HSC specimens depend in construction requirements; however, considering notable strength gain at later stages, testing age of 56 days or 90 days is often recommended (ACI, 2010).

It's obvious that the HSC has lots of advantages over NSC. HSC usually include ingredients highly resistant to the chloride damage and other chemical attacks. Due to its low permeability, it's highly durable, and consequently requires low maintenance cost. In addition to these advantages, HSC allows the designers to produce minimized structural sections to meet the serviceability limits. The largest application of HSC in buildings is columns of High rise structures. Different buildings and bridges have been constructed using HSC. For building examples, Taipei 101 in Taiwan 2004, Brillia tower in Tokyo 2004, 505 5th Avenue in New York 2004, and Bay Adelaide Center in Toronto 1991. While, for bridge examples, State route 920 over I-75 in Georgia 2002, Federation Bridge Prince Edward Island in Canada 1997, and Portneuf in Quebec 1992.

2.3.2. Elastic modulus

ACI-318 (ACI,2011) defines the secant modulus of elasticity as the ratio of stress and strain at 40% of the compressive strength. As strength of concrete increases, its modulus of elasticity increases as well. Hence the same parameters that affect the compressive strength of concrete also affect the elastic modulus. Consequently, most of the empirical formulations express modulus of elasticity as a function of compressive strength. The equation suggested in ACI 318 (Eqn. 2.1) overestimates elastic modulus of HSC and ACI 363 (ACI, 2010) suggests a different equation for HSC based on studies done by Carraquillo et al. (1981) that have been shown to produce conservative values for normal-density concrete (Shah and Ahmad, 1994):

$$E_c = 3320\sqrt{f_c'} + 6900\ (MPa) \tag{2.1}$$

2.3.3. Poisson's ratio

The data available on Poisson's ratio of HSC is very limited. Poisson's ratio of HSC is constant in the linear zone but increases in the non-linear zone as a function of axial strain. In the linear zone range, poisson's ratio is bit affected by compressive strength, curing method and age of concrete (Logan et al., 2009). Poisson's ratio of HSC reported by different studies in the linear range at 40% of ultimate stress is summarized in Table 2.4.

Poisson's ratio of HSC in the linear zone range carried around 0.2, which is around the same range of values obtained for NSC (0.15-0.25).

Table 2-4: Poisson's ratio of HSC reported by different studies

study	Strength range (MPa)	Poisson's ratio	Standard deviation
Perenchio and Klieger (1978), as reported in Iravani (1996)	N.A.	0.22	N.A.
Carrasquillo et al. (1981)	34-73	0.210	0.016
Ibrahim and MacGregor (1994)	73-99	0.18	N.A.
Iravani (1996)	64-125	0.17	0.023
Logan et al. (2009)	34-120	0.17	0.07

2.4. GFRP reinforced columns

(De Luca et al. 2010) conducted an experimental program to investigate whether the compressive behavior of longitudinal GFRP bars impacts the column performance, and to understand the contribution of GFRP ties to the confinement of the concrete core, and to prevent instability of the longitudinal reinforcement. Five specimens were tested under axial loading: one benchmark steel RC column and four GFRP RC columns.

Figure 2.3 shows the mode of failures for A-12 and B-12 with tie spacing of 12 inches. Failure typically initiated with vertical cracks, followed first by lateral deflection of the longitudinal bars contributing to the splitting of the concrete cover and then by crushing of the concrete core and buckling of the longitudinal bars.

Figure 2.4 compares the response of all specimens in terms of normalized axial stress and deformation. Each curve is the envelope of all the load-unload cycles imparted. The initial slope is identical for all the curves. The GFRP specimens exhibit a gradual decrease in stiffness as the load reaches approximately 60% of the peak capacity, whereas for the steel RC specimen (S-16), the stiffness starts decreasing as the load reaches approximately 80% of the peak capacity.

Figure 2.3– Close-up of buckled GFRP bars for specimen A-12 (De Luca et al. 2010)

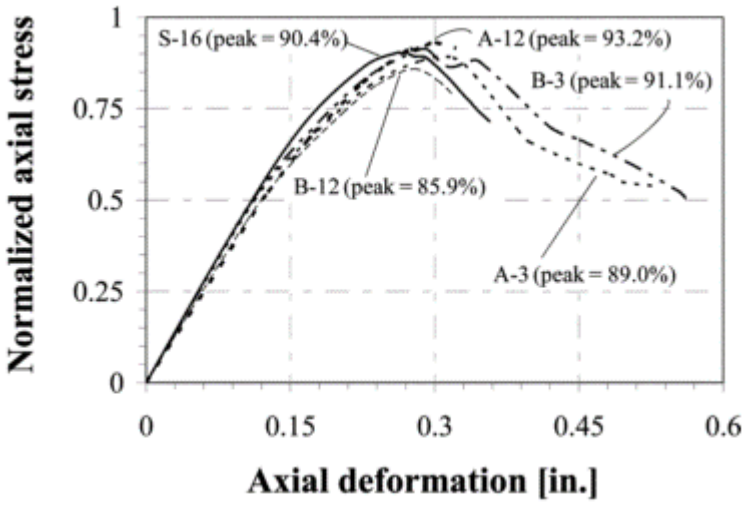

Figure 2.4– Normalized axial stress-axial deformation (De Luca et al. 2010)

Afifi (2013) Conducted experimental and analytical investigations on circular concrete columns reinforced with FRP bars and spirals under concentric axial loading. The program included 27 circular concrete columns having 300 mm diameters and 1500 mm height. The columns were reinforced using different materials (steel, GFRP, and CFRP). The experimental program included also studying different parameters such as longitudinal reinforcement ratio, ties volumetric ratios, confinement type (spirals vs hoops); and lap length of hoops. The testing results revealed that FRP bars were effective in resisting compression till reaching the peak load. The FRP bars contribution average 8% and 13% of

the column maximum capacity for GFRP and CFRP RC specimens, respectively. The authors reported that ignoring the contribution of FRP longitudinal bars in the CSA S806 (2012) design equation underestimated the maximum capacity of the tested specimens. They suggested a modification to the design equation to accurately predict the ultimate load capacities of FRP RC columns.

Tikka et al. 2013, conducted an experimental study to investigate the behavior of eccentrically loaded slender NSC columns that are longitudinally reinforced with GFRP and laterally tied using a carbon fiber spiral wrap. The columns were divided into two series: Series A and Series B were the reinforcement were provided by different manufacturer. For each series two columns (C1 and C2) were longitudinally reinforced with four 12.7 mm diameter GFRP bars and two columns (C3 and C4) were reinforced with six 12.7 mm GFRO bars. For all of the columns the maximum axial load (P_{test}) coincided with the initial onset of crushing of the concrete along the compression face. In five of the column tests the initial onset of crushing of the concrete occurred within the middle third of column height and for columns A-C2, B-C1 and B-C4 the initial onset of concrete crushing occurred nearer the end haunches.

Figure 2.5 compares the strain to the axial load (P/P_{test}) where P is the applied axial load and P_{test} is the column axial capacity. The concrete stress was ranging from 0.0032 for low eccentricity columns to 0.0045 for higher eccentric columns, while for the tensile strain the tensile strain was nearly the same, except for columns with high eccentricity ($e/h \geq 0.4$)

where the tensile strain become visibly apparent due to second order effects.

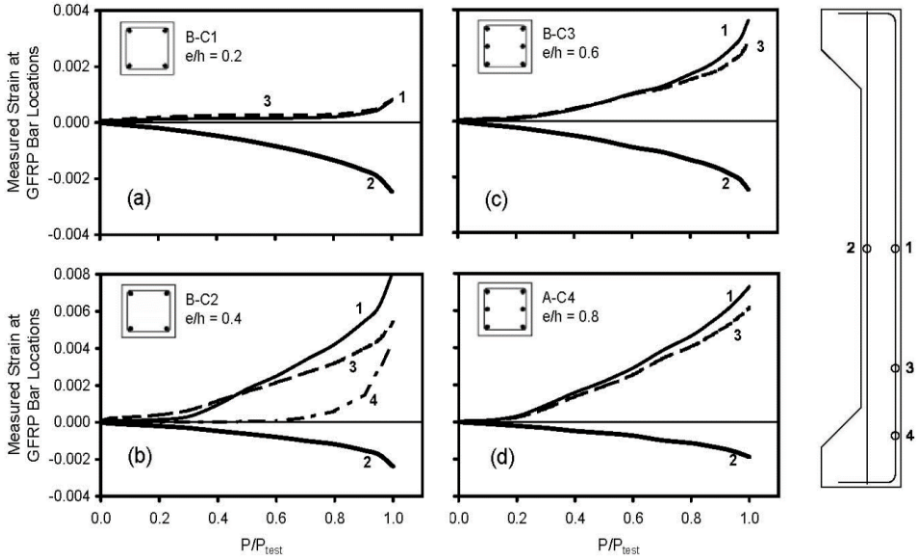

Figure 2.5– Measured strain at selected GFRP bars (Tikka et al. 2013)

Leite et al. 2013, tested 32 columns with unequal eccentricities at the ends to calibrate and check simplified approaches. The variables were: concrete strength, slenderness, reinforcement ratio. Based on the test results of these columns, five types of failure were defined; instability (by tension or compression), elastic instability, ultimate strength of the section wither tension or compression failures. At the ultimate load, a plastic hinge is produced in the critical section after reaching the maximum load and racks starts to appear. Also, it was observed that columns with HSC had a more brittle failure behaviour compared to NSC. Cover spalling occurs more early in HSC. The strains registered in the concrete for the ultimate load are larger than the strain provided by design codes which gives an underestimation of the ultimate bending force. Finally, the authors mentioned that the accuracy of using simplified methods has a low accuracy in case of HSC.

(Tobbi et al. 2014) had conducted an experiment using twenty concrete columns measuring 350 X 350 X 1400 mm and tested under concentric loading. The specimens were including one plain concrete columns, 8 columns entirely reinforced with GFRP bars and 11 columns reinforced with steel longitudinal bars and FRP tie and cross ties.

The effect of longitudinal reinforcement was investigated by comparing the columns with FRP and steel longitudinal reinforcement, see Figure 2.6. Two columns G-1-120-1.0 and G-1-120-1.0S had the same reinforcement ratio (1%). the steel reinforced column had a higher peak stress than the GFRP column, and the GFRP column showed a nearly constant value of load carrying capacity after the peak stress. The difference in post peak behavior is explained as the load remains constant when the steel yield, while the load increased with axial strain with elastic GFRP bars.

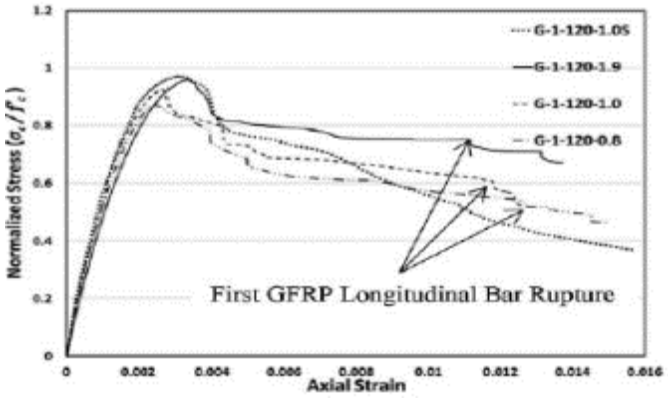

Figure 2.6 – Effect of longitudinal reinforcement on compressive behavior of columns. (Tobbi, et al. 2014)

The ultimate axial compressive strain for columns reinforced longitudinally and transversally with FRP can reach a value of the same magnitude as the FRP ultimate tensile strain of the longitudinal bars under good confinement conditions.

The authors proposed an equation (Eqn. 2.2) to take into account the contribution of the GFRP bars in compression at peak.

$$P_n = 0.85X\ f_c'X\left(A_g - A_{frp}\right) + \ \varepsilon_{co}XE_{FRP}XA_{FRP} \tag{2.2}$$

Where A_g is cross sectional area of the column; A_{frp} is cross sectional area of FRPP longitudinal reinforcement; f_c' is the concrete compressive strength; ε_{co} is concrete strain at peak stress and is E_{FRP} modulus of elasticity of FRP longitudinal reinforcement.

The same author conducted another experimental program to study the effect of FRP bars as longitudinal and lateral reinforcement on the concrete column response (Tobbi et al. 2012). Eight specimens were tested: one made of plain concrete, two steel RC columns and five GFRP RC columns. All of the RC columns had similar reinforcement ratios 1.9% of the gross sectional area.

The main conclusions stated by these authors were:

- Early spalling of the concrete resulted in a loss of axial capacity before the lateral reinforcement being utilized.
- Strength reduction factor of 0.85 can be used for GFRP reinforced columns.
- FRP compressive strength at 35% of the FRP maximum tensile strength.
- GFRP bars used contributed 10% of the column capacity which is close to steel's contribution 12%.

Extensive study was conducted at University of Sherbrooke to study the behavior of eccentric columns using fifty full scale specimens with circular cross section of 305 mm and 1500 mm height. Several articles were published discussing the effect of different parameters such as spiral spacing, reinforcement ratio, reinforcement type and using different concrete strength **(Hadhood et al. 2016a and 2016b, 2017a, 2017b, and 2018)**. The test variables were the reinforcement ratios and the eccentricity to diameter ratio. The author stated that the GFRP reinforcement can be effectively integrated into high-strength concrete column, which proved to enhancing the stiffness of cracked concrete section. The tests results indicated that the GFRP reinforced HSC columns exhibited compression failure resulting from concrete crushing for specimen under low eccentric loading, while specimens tested under high eccentric loading had a flexural-tension failure imitated in the specimens. It's worth mentioning that failure off the columns under high eccentric loading weren't triggered by rupture or crushing of the GFRP bars. The maximum strain value for GFRP bars was -3100 microstrains (13% of the ultimate strain) for the tension side and 6800 microstrains 28% of the ultimate strain on the compression side. The author mentioned also that the ACI 440.1 R-15 or CSA/CAN S806-12 accurately predicted the axial and flexural

capacity of the GFRP reinforced HSC columns by ignoring the contribution of the GFRP bars in compression.

XUE et al., 2014 conducted an experimental program to investigate the mechanical behavior of GFRP RC columns under static eccentric loading. Seven square 300 mm width GFRP RC columns were tested. The test variables included three eccentricities 60, 150, and 300 mm. They also include three nominal slenderness ratios 8, 10, and 12. Finally they include three reinforcement ratios 0.45%, 0.67%, and 1.27%. The tests were conducted using a 10,000 KN testing machine in Tongji University. Both end supports of the columns were designed as hinged connections with predefined eccentricity. Figure 2.3 shows the specimen details. The following points were concluded:

For specimens with length of 3600mm (nominal slenderness ratio is 12), the ultimate load of CE-3 with an eccentricity of 60 mm was 1632kN, while that of CE-4 (with an eccentricity of 150 mm) and CE-5 (with an eccentricity of 300 mm) were 493kN and 300kN, which were decreased by 69.8% and 81.6% when compared with that of CE-3, respectively. The results showed that eccentricity had a significant effect on ultimate load of eccentrically loaded GFRP RC columns.

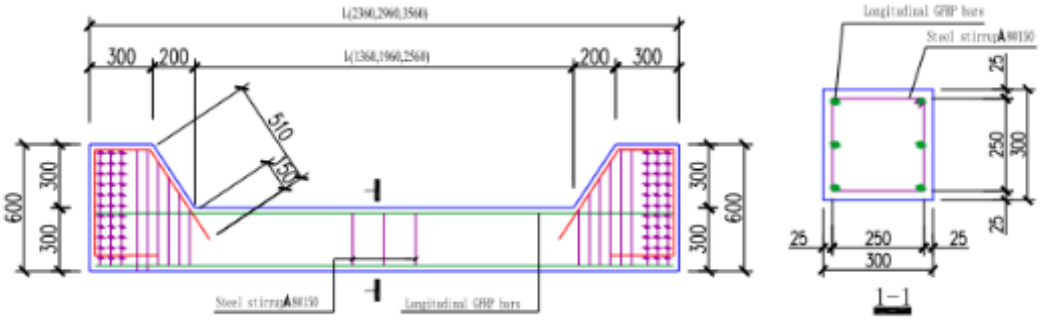

Figure 2-3– Specimen detail, [XUE et al., 2014]

(Hales et al. 2016) experimented nine circular columns reinforced, six of them were short and three were long columns. Three of these columns were reinforced using GFRP bars for transverse and longitudinal reinforcement. The failure mode for the short columns with low eccentricities was mainly a material type failure caused by compressive failure of the concrete, tensile rupture of GFRP spiral, compressive rupture of the longitudinal GFRP bars

and compressive buckling of the longitudinal steel bars. Moreover, the failure mode for the long slender columns was a stability type buckling failure around the mid height region of the columns. The authors confirmed that GFRP spiral can be used in columns but they should be provided with larger cross sectional area and smaller pitch to have the same confinement levels for those of steel stirrups. Also, GFRP longitudinal reinforcement can provide larger deflection capacity compared to steel bars due to their higher tensile strength; in addition, they provide self-centering effect.

Fan and Zhang 2016 tested BFRP RC columns reinforced with BFRP bars. The columns were made with NSC with concrete strength of 33 MPA. The columns dimensions were 900 mm height and square cross section of 120 mm width. The columns were tested under small eccentricity of value 20 mm and large eccentricity of value 80 mm. The results were similar to GFRP RC columns under small were failure was marked by crushing of concrete and under large eccentricity where the failure was marked by intense and large tensile cracks formed along the tension side of the columns.

Maranan et al. 2016, investigated the behavior of concentrically loaded GFRP circular columns reinforced with GFRP bars. Six short columns with L/r = 8 and two slender columns with L/r = 16 were tested. The GFRP bars contributed an average of 7.6& to the overall capacity of the tested columns. The compression contribution of GFRP bars varied from 6.6% to 10.5%. the short columns failed due to crushing of concrete or shear failure.

Several studies have been published recently by a research group in University of Wollongong on the behavior of GFRP-RC columns under axial and/or eccentric loading (Hadi and Youssef 2016; Hadi et al. 2016; Hasan et al. 2016 and 2017; Karim et al. 2016, 2017a, 2017b). These studies include experimental and analytical investigations of various parameters. The experimental program used square cross section of 210 mm sides and 800 mm height and/or circular sections of diameter 205 mm and height 800 mm. The specimens tested under concentric loading; eccentric loading of 25 mm and 50 mm; and/or two-point loading flexure. The test variables were the type of reinforcement (steel vs. GFRP); external confinement or none; internal reinforcement or none; normal concrete or fiber-reinforced concrete. The analytical program included developing interaction diagrams; parametric

studies; estimation of ductility. Their concentric GFRP-RC specimens exhibited second peak points indicating proper confinement, provided by helices spaced each 30 mm or 60 mm. The closely spaced specimen exhibited, however, higher second peak than the other (Hadi et al. 2016). They reported that reducing the GFRP helices pitch from 60 to 30 mm led to an improvement in the performance of the GFRP-RC specimens in terms of load-carrying capacity, bending moment, and ductility. They also reported that the contribution of the longitudinal steel bars in the load carrying capacity of the concentric column specimens was about twice the contribution of the longitudinal GFRP bars, whereas the ductility of the GFRP-RC column specimens was slightly greater than the ductility of the reference steel-RC column specimens under different loading conditions. Karim et al. 2017 addressed the limits of FRP reinforcement in members with different cross sections and different bar arrangements. The study findings include proposing an equation for calculating the deformability factor (DF) using integration of the concrete layers through Popovics's model (1973), in which the DF is a ratio of the product of moment and curvature at ultimate to the product of moment and curvature at serviceability limit state.

Sun et al. 2017 investigated the behavior of GFRP RC columns under an eccentric load values of 175 mm, 125mm and 75 mm using columns with 180 mm X 250 mm. The columns exhibited brittle failure after reaching the peak load. The GFRP bars do not experience damage even after the concrete is damaged. The results indicated that GFRP bars work better with concrete as the compression reinforcement when compared to tensile behavior. Therefore, GFRP bars exhibited significant advantages.

Elchalakni and Ma 2017 conducted an experimental program on 17 rectangular columns with dimension of 150 mm and 75 mm reinforced with both steel and GFRP rebars. The columns were tested to failure under various loading conditions, in order to determine the effect of load eccentricity on axial capacity. The columns were tested under different loading conditions starting from axial loading to pure flexural. The test parameters were the spacing of transverse reinforcement and type of reinforcement. It was found that. The average axial load carrying capacity of the GFRP RC columns under concentric load was 93.5% of their steel RC column counterparts. The GFRP RC columns also exhibited 3.2% average increase

in the load carrying capacity and the steel reinforced columns achieved 15.8% increase in the concrete section capacity compared to plain concrete section. It was also mentioned that GFRP RC columns and beams were found more ductile compared to their steel reinforced counterparts because they absorb more energy through their ability of well deforming in the post-peak collapse region.

Khorramian and Sadeghian 2017 presented and experimental and analytical studies on short concrete columns reinforced with GFRP rebars. The program consisted of fourteen 500 mm long specimens with a square cross section of 150 * 150 mm. Three eccentricity to width ratios of 0.1, 0.2 and 0.3 were considered. The experimental program showed no crushing of GFRO bars at peak load and the corresponding strain did not reach 50% of their crushing capacity obtained from material test. According to the experimental and analytical study presented in this article, it was suggested to consider GFRP bars in compression as linear elastic material until concrete reach its maximum compressive strain.

Guerin et al. 2018 conducted experimental studies for columns with square cross section of 400 x 400 mm and 2000 mm long. The test parameters included the applied eccentricity (0.1h, 0.2h, 0.4h and 0.8h) , reinforcement ratios and reinforcement type (steel and GFRP). All the columns were made with NSC of 41.2 MPa. The results of this experimental investigation were published in two journal articles (Guerin et al. 2018a and Guerin et al. 2018b).

The GFRP reinforced columns showed similar behavior for steel reinforced columns. The GFRP columns failed due to concrete crushing for all the tested eccentricities. Also, it was shown that using maximum GFRP tie spacing as half the limit recommended in ACI 318-14 for steel reinforced columns was sufficient to prevent the longitudinal reinforcement from buckling and to confine the concrete core in post-peak stages (Guerin et al. 2018a).

(**Guerin et al. 2018b)** investigated the influence of using different reinforcement ratios (1.0, 1.4, and 2.5%) for GFRP reinforced columns. The results of this investigation showed that GFRP reinforcing bars can develop high strains in compression up to 12,000 με. The tensile bars with stood tensile forces for all the tested eccentricities up to reaching peak failure as a result of concrete crushing. Also, the study suggested to classify the axial-flexural interaction

diagram for GFRP reinforced columns into three categories similar to steel reinforced columns: a) compression controlled which is recognized by concrete crushing $\varepsilon_c \geq \varepsilon_{cmax}$; $\varepsilon_{ft} \leq 2000\ \mu\varepsilon$, b) compression tension transistion, characterized by the initation of cracks on the tension side with strain limitation $\varepsilon_c \geq \varepsilon_{cmax}$; $2000 \leq \varepsilon_{ft} \leq 5000$

CHAPTER 3 EXPERIMENTAL WORK

3.1. Introduction

The details of the experimental program that included twenty full-scale columns are presented in this chapter. The design, construction and testing of the specimens at the Structural Engineering Laboratory at the University of Sherbrooke are discussed in details.

3.1.1. General

FRP material is a fairly newly discovered which means a lot of research needed to be conducted in this area to fully understand the behavior of this material when used with reinforced concrete. This means theoretical analysis and experimental work need to be conducted specially with high strength concrete. The research project aims to investigate the compressive behavior of high strength concrete columns reinforced with FRP under eccentric loading. The research in this report is divided into two main parts; experimental program and theoretical analysis. The experimental program includes the most effective parameters that are mainly affecting the behavior of columns under eccentric loading. The results of the tests were compared and conducted with the theoretical analysis aiming to provide new guidelines for the design and behavior of High strength concrete columns reinforced with FRP bars.

The test results were analyzed to derive equations for the development of axial load-moment interaction diagrams for square cross section. Besides, it was used check the validity of applying the current design equations used for columns made with NSC and compare it with the test results. All the work were used to provide guide lines to design high strength high strength concrete column reinforced with FRP.

3.2. Objectives

The main objective of the research program is to investigate and evaluate the performance of High strength concrete columns reinforced with FRP bars and stirrups under eccentric loading. Also, it aims to propose design guidelines that include new strength factors to account for the behavior of FRP reinforcement. The specific objectives of this study can be summarized as follows:

- Determine axial resistance of columns with high strength concrete under eccentric compression.
- Evaluate the data published by other researchers related to stress block parameters, ultimate compressive strain of HSC.
- Evaluate the effect of testing parameter, i.e., spacing of transverse reinforcement, and longitudinal reinforcement on strength and ductility of columns with high strength concrete.
- Develop and introduce modifications to the existing design equations of the GFRP-BFRP-RC columns under eccentric loading.
- To evaluate the contribution of BFRP and GFRP bars on the compression side.

3.3. Experimental program

A total of 20 square columns were designed in order to be tested under different eccentric loading. All columns have 400 mm width and an overall height of 2000 mm.

3.1.1 Proposed test parameters

In order to properly fulfill the previously mentioned objectives, parameters were chosen to be studied in this research program. These values inside each parameter has been chosen based on the literature review, codes design equation and personal experiences. The parameters are:

1. Eccentricity.
2. Type of reinforcement.
3. Glass Fiber longitudinal reinforcement ratio.
4. Comparing NSC with HSC.

3.1.2 Material properties

The research proposed examines the effect of various reinforcement types and stirrup spacing. This variety is chosen to draw a full conception for charging vital properties upon the behavior of concrete columns under eccentric loading.

3.1.2.I: Concrete

The specimens were all cast with ready-mixed concrete with a water-to-cement ratio of 0.32. The cement used was Type GUb-8SF, which was premixed with silica fume and water reducer, as shown in Table 2. The silica-fume percentage was 9.4% by mass. The slump was around 80 mm (before adding the superplasticizer). The concrete strength was determined in accordance with ASTM C39/C39M by testing 150 × 300 mm cylinders that were cured under conditions similar to that of the cast specimens. The concrete cylinders had an average strength of 71.2 MPa on the day of testing.

3.1.2.II: Fiber reinforced polymers (FRP)

Two types of fiber polymers bars are used in this research, Glass (GFRP) and basalt (BFRP). These types are the most familiar among the fiber family. Sand-coated GFRP bars and ties (TUF-BAR/PB Composites, 2016) were used to reinforce the column specimens in the longitudinal and transverse directions, respectively, as shown in Fig. 3-1. The GFRP bars had a sand-coated surface to enhance their bond with the surrounding concrete. No. 6 (19 mm in diameter) GFRP bars were used as longitudinal reinforcement for all the GFRPRC columns; No. 3 (10 mm in diameter) GFRP ties were used as transverse reinforcement. The tensile properties of the longitudinal GFRP were determined according to ASTM D7205/D7205M-06, as reported in Table 3-1.

Figure 3-1–GFRP and BFRP cages

Table 3-1 Mechanical properties of FRP bars*

Bar size	Diameter (mm)	Area (mm^2)	Elastic tensile modulus (GPa)	Tensile strength (MPa)	Tensile strain (%)
GFRP reinforcement					
No.3	10	71	63.7	1370	2.2
No.6	20	285	62.7	1236	2.0
No.8	25	510	61.7	1001	1.9
BFRP reinforcement					
No.4	13	129	51.4	1414	2.70
No.6	20	284	120	1646	2.50

* *As provided by the manufacturer*

3.1.2.III: Steel Reinforcement

Grade 60 steel bars were used to reinforce the steel-reinforced control specimens. Deformed No. 6 (20M) and No. 3 (10M) steel bars were used as longitudinal and tie reinforcement, respectively. The mechanical properties of these steel bars were obtained by testing five representative specimens of each diameter according to ASTM A615/A615M-14 [23], as shown in Table 3-2. Figure 3-2 shows typical cages for steel reinforcement.

Table 3-2: Mechanical properties of Steel bars*

Bar size	Diameter (mm)	Area (mm^2)	Elastic tensile modulus (GPa)	Yield Tensile strength (MPa)	Ultimate Tensile strength (MPa)	Tensile strain (%)
10M	11.3	100	200	460	660	0.2
20M	19.5	300	200	460	660	0.2

** As provided by the manufacturer*

Figure 3-2– Steel cages

3.4. Specimen Design

A total of 20 specimens are designed to study the effect of eccentric loading. All the test specimens had a 400 × 400 mm cross section and a height of 2000 mm, giving an aspect ratio of 0.2. These dimensions were selected to ensure the specimens were large enough to be considered full-scale columns, yet easy to handle without cracking. The specimens were designed to investigate the influence and behavior of using GFRP and BFRP reinforcement in HSC columns and to test them under different magnitudes of eccentricities. The eccentricities were 80, 120, 160, and 240 mm. These values were selected to ensure different and discrete points that could be plotted to cover a wide range of the interaction diagram representing the strength of the column under different eccentricities. The columns had a reinforcement ratio equal to 1% of the concrete cross section, which meets the minimum reinforcement ratio for flexural reinforcement specified in ACI 440.1R-15 [5] and ACI 318-14M [25]. The spacing for the FRP ties was 150 mm and 300 mm for the steel. The tie spacing for steel RC columns was chosen considering the allowable maximum tie spacing as provided in the ACI318-14.

3.5. Specimens production

3.5.1. Cage Assembling

All the cages (steel, basalt and glass) were made at Sauvee laboratory. The bars were fixed horizontally between two wooden plates which has identical slots to fix the bars in place. This ensures all the columns with the same number of bars have the same spacing. The stirrups were then inserted from one end and then tightened in place using Tie-raps. Finally, plastic circular bar spacers were fixed on the bottom and the sides of the cages in order to maintain a 25mm clear cover. Figure 3.8 shows some assembled cages of different reinforcement materials. The end regions of the columns have more dense stirrups spaced at 8cm to resist the end moment due to the end capping.

Table 3-3: Test Matrix

SERIES	Reinforcement type	Code	Vertical reinforcement		Horizontal reinforcement		**Eccentricity**	**Parameter**
			ρ_L (%)	Number of bars	No.	S (mm)		
I	Steel	Se80	1.07	6 M20	10M	300s	80	Steel Reinf.
		Se120					120	
		Se160					160	
		Se240					240	
II	BFRP	Be80	1.07	6#6	#4	150	80	Basalt Fiber
		Be120					120	
		Be160					160	
		Be240					240	
IV	GFRP	G1e80	1.07	6#6	#3	150	80	Glass Fiber
		G1e120					120	
		G1e160					160	
		G1e240					240	
VI		G2e80	2.55	8#8	#3	150	80	Reinforcement ratio
		G2e120					120	
		G2e160					160	
		G2e240					240	
VI		G3e80	0.49	4#5	#3	150	80	
		G3e240					240	
VII		G4Te80	0.53	3#6	N/A	150	80	Comp. reinf.
		G4Te240					160	

3.5.2. Instrumentation

The columns was instrumented to measure displacement, rotation, tensile and compressive strains. A linear Variable different transducers (LVDT) was be used to measure column mid-span lateral deformations. A light steel frame mounted on the laboratory floor supporting the LVDTs. Concrete strain gauges were used to monitor and record the concrete strain during testing. Three LVDTs were mounted horizontally along the column to measure lateral displacements.

To measure the strain for both the concrete and the reinforcement bars, electric strain gauges were properly installed on the stirrups and the longitudinal bars to measure the change in strain during testing. A total of 9 strain gauges of 10 mm length were used in each column under eccentric loading. Four were attached on the bars under tension: two strains - at 50 cm at the start of the testing zone and two strain gauges at the mid height of the column. For the compression side, two strain gauges is attached to the longitudinal bars on the compression side at the mid height and the other three mounted in different locationson the mid-height stirrup. Figure 3-3 shows the details of the instrumentation process. During testing the results were recorded using a data acquisition system that was connected to a computer, control unit and a power supply.

Figure 3-3 – Instrumentation

3.5.3. Formwork construction

A form work has been constructed to be able to cast 12 columns in one casting. This ensured that all the columns have nearly the same conditions and geometry. The columns were casted horizontally to be able to reach the bottom of each column and facilitate vibrating the columns throughout the length during the casting process, similar to the casting conditions for pre-casted members for columns sections. Figure 3-4 show details for the formwork.

Figure 3-4 – Form work used

3.5.4. Concrete casting

A High strength Portland cement concrete is intended to be used to cast the 24 columns. Figure 49 All columns were casted in CFI laboratory, the concrete strength is designated to be 70 MPa. Standard concrete cylinders were cast for each patch to establish the 7- and 28-days strength of concrete as well as the strength on the day of testing. Molds were used to cast 100 mm by 200 mm standard cylinders to perform the standard compression tests. The cylinders were casted in three layers of equal volume, and were compacted by rodding 25 strokes after each layer, in accordance with the CSA Test Method A23.2-3c (ASTM C192-20a). The curing was done for cylinders together with the test specimens to be under identical environmental conditions. The cylinders were tested at 7, 28 days and were tested also in the

testing day. Figure 3-5 show the square piles during the casting process and using vibrator and after casting.

Figure 3-5 – Concrete casting

3.5.5. Test setup

A total of 20 columns were tested under eccentric loading. The proposed eccentricity values are presented previously in the test matrix table. The specimens were first externally confined at the ends by means of steel brackets, specially manufactured for this purpose. This would prevent premature failure of columns at the ends, outside the test region. The brackets were made of two steel plates that were connected together by bolts. Figure 3-6 shows the details of the eccentricity model setup. From the other hand, load and deformation measurements were taken in small increments as the applied load increases. The strain gauge readings were monitored during testing. The overall behaviour of specimens were manually recorded and the crack patterns were observed. As the peak load approaches, the load was slowed down due to the failure of the member. The readings were taken at a faster rate as deformations increase faster under approximately constant load, follows by subsequent reduction in load.

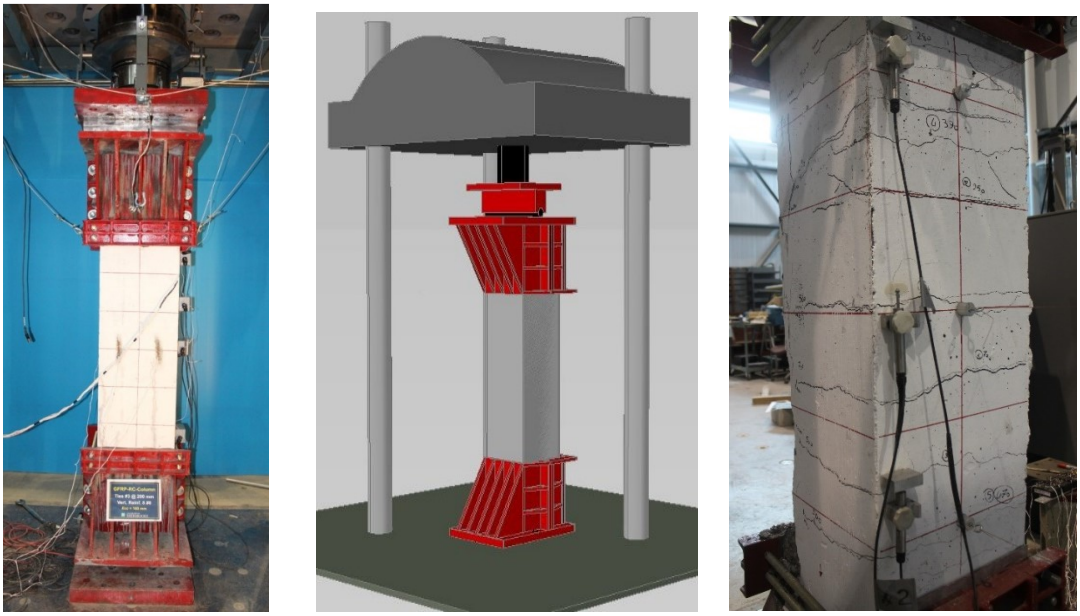

(a) (b) (c)

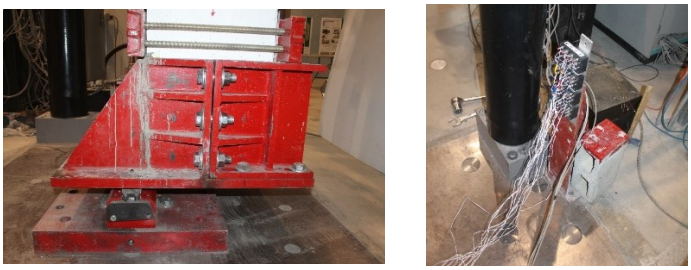

(d) (e)

Figure 3-6 – Test setup: a) elevation of test setup, b) 3d drawing of test setup, c) lower end cap and applied eccentricity and d) data acquisition system.

CHAPTER 4 FULL-SCALE HIGH STRENGTH CONCRETE COLUMNS REINFORCED WITH GFRP BARS AND TIES SUBJECTED TO ECCENTRIC LOADS

Foreword

Authors and Affiliation:

- Ashraf Salah-Eldin: Ph.D. candidate, Department of Civil Engineering, Université de Sherbrooke, Sherbrooke, Quebec, Canada, J1K 2R1.
- Hamdy M. Mohamed: Research Associate/Lecturer, Department of Civil Engineering, Université de Sherbrooke, Sherbrooke, Quebec, Canada, J1K 2R1.
- Brahim Benmokrane: Professor, Department of Civil Engineering, Université de Sherbrooke, Sherbrooke, Quebec, Canada, J1K 2R1.

Journal Title: (Engineering Structures, Elsevier)

Abstract:

In recent decades, high strength concrete (HSC) has been widely used in bridge elements, tunnels, and precast concrete members. However, a limited number of studies have investigated the behavior of integrating HSC columns with glass fiber-reinforced polymers (GFRP) bars. Moreover, most concrete codes do not explicitly cover concrete with strength above 55 MPa. This paper investigates the behavior of HSC reinforced with GFRP bars and ties when subjected to eccentrically axial loads. Full-scale columns of 400×400 mm square

cross section and 2000 mm height were tested under axial monotonic loading. The test variables were the eccentricity to width ratio, concrete strength, and reinforcement type using steel and GFRP bars and ties. The test results indicated that the failure of the test specimens under different levels of eccentricity was not triggered by rupture of the GFRP bars on the tension side, up to attending the maximum section capacity governed by concrete strain limitation. The load- axial displacement, load- lateral displacement, failure mode and reinforcement strain responses of all GFRP reinforced-HSC columns were presented and compared to that of the steel reinforced-HSC columns. The behavior of HSC columns reinforced with GFRP bars and ties subjected to eccentric axial loads were evaluated by drawing the axial force-flexural moment interaction diagrams and compare them with steel reinforced columns. Analytical method (layer by layer approach) was developed to predict the axial and flexural load capacity of the GFRP-reinforced HSC columns. Parametric study was introduced to examine the effect of increasing the reinforcement ratio, the concrete strength and investigating the strength contribution of compression GFRP bars.

Keywords: Columns; eccentric; concrete; HSC; GFRP; interaction diagram; sectional analysis.

4.1. Introduction:

Corrosion of steel reinforcement in concrete structures is almost inevitable when exposed to aggressive environment leading to loss of strength and serviceability. Many researches were conducted to develop new technologies to solve this problem. High strength concrete (HSC) was developed and promoted to be used owing to its wide range of advantages over normal strength concrete. It offers higher compressive strength and more durable concrete which allow the designers to reduce the cross-section area. Another industrial development was made by replacing the steel reinforcement with noncorrosive composite glass fiber-reinforced polymer (GFRP) bars. Reinforcing HSC with GFRP bars will in turn offers more durable and resistant concrete members.

HSC is usually referred to concrete with compressive strength higher than 55 MPa according to ACI-ASCE 441R-96 committee. It’s highly recommended for structures subjected to

harsh environment because of its lower permeability(Collins et al. 1993), less water content, and superior durability and strength. It's also used in pre-casted concrete elements, long-span bridges, and heavily loaded reinforced column. HSC is lower in ductility compared to normal strength concrete (NSC). It's reported also tat HSC reinforced with steel bars exhibit early cover spalling and brittle failure under high axial loads, concentric and eccentric, unless adequate confinement is provided (Foster 2001; Lee and Son 2000). However, using GFRP bars as reinforcement for HSC, especially in columns, is still a relevant issue to be addressed and not covered by design codes such as ACI 440.1R-15 and CSA S806. Moreover, the contribution of compressive GFRP reinforcement in columns is questioned and under study. Only limited studies investigated the behavior of HSC columns reinforced with GFRP under eccentric and concentric columns.

Recent studies were conducted to study the behavior of GFRP in normal strength concrete. (Luca et al. 2009) indicated that the behavior concrete columns internally reinforced with GFRP bars is similar to the conventional steel RC columns for reinforcement ratio of 1%. (Mohamed et al. 2014; Tobbi et al. 2014) tested circular and square concrete columns reinforced with GFRP bars, ties and spirals. They showed the viability of using GFRP reinforcement in axially loaded columns. The contribution of GFRP bars in compression was reported to range between 3-10% of the total load carrying capacity of the RC columns compared to 12-16% compressive contribution for steel reinforcement. Also, it was reported that the axial capacity of reinforced columns are lower by 13-16% when reinforced with GFRP bars compared to steel bars (Alsayed et al. 1999; Pantelides et al. 2013). As for columns subjected to eccentric loading, (Hadhood et al. 2016a; Issa et al. 2011; Xue et al. 2012) have investigated their behavior under different reinforcement ratio, confinement spacing and different values of eccentricity. They reported that the GFRP RC columns exhibited smaller axial capacity and had larger lateral displacement compared to steel columns with the same properties. (Guérin et al. 2018) reported experimental test results for 12 full scale concrete columns of 405×400mm cross section and 2000 mm in height. The columns were fully reinforced with GFRP bars and ties and were then tested under different eccentric values. Their study indicated that GFRP reinforced concrete columns had similar failure pattern compared to steel reinforced control specimens.

Only limited studies covered using HSC with GFRP bars under combined axial and flexural loads or under pure flexural. (El-Nemr et al. 2013) reported that using GFRP bars in HSC beams contributed in enhancing the ultimate load-carrying capacity, crack width and deflection of beams. (Hales et al. 2016) conducted an experimental program testing 9 HSC GFRP RC columns with different slenderness ratio. It was reported that for short columns the failure was classified as material failure, where the failure was due to rupture of concrete on the compressive side, tensile rupture of GFRP spirals or buckling of GFRP compressive bars. (Hadi et al. 2017) tested 12 circular HSC reinforced with GFRP spiral and longitudinal bars with 210 mm diameter and 800 mm in height. They have found that GFRP bar reinforced HSC specimens sustained similar axial load under concentric axial compression with the same amount of steel reinforcement. Also, the contribution of GFRP bars in the total carrying capacity was half that for steel reinforcement. Moreover, (Hadhood et al. 2016b) tested 10 circular columns reinforced with GFRP using HSC. It was reported that for small eccentricity the failure was mainly controlled by concrete and the failure was due to concrete crushing on the compression side. It was also mentioned that a flexural tension failure initiated in specimens tested under high eccentric loading.

Few assumptions and investigations were made by researchers and design codes in North America to accurately predict the ultimate strength of columns with GFRP bars. (Choo et al. 2006a) found that the interaction diagram for rectangular columns doesn't exhibit balanced points due to the linear behavior of GFRP bars and he emphasized that the GFRP compressive bars should be able to reach strain equal to that of concrete. Based on these conclusions (Zadeh et al. 2013) assumed that GFRP can be replaced with equivalent concrete area during analysis for simplicity. While many researchers conducted different values for the contribution of GFRP bars in compression, design guides didn't provide any guidance regards this aspect. CAN/CSA S806-12 ignores the compressive bars contribution in both flexural and compression members. The ACI 440.1R-15 highlights about the urge for more extensive research regarding concrete columns.

4.2. Objectives:

To focus on investigating the behavior of HSC columns reinforced with GFRP bars and ties, the research presented herein address full-size tied HSC columns subjected to different range of eccentricities. The columns are with high aspect ratio to minimize the effect of slenderness. Overall, this study aims at:

- Investigating the behavior of HSC columns reinforced with GFRP bars and ties, and the consequent effect on the failure mode and strength compared to steel reinforced columns.
- Assessing the compressive contribution of GFRP bars in HSC columns.
- Comparing GFRP reinforced columns behavior with steel reinforced columns.
- Developing analytical model to predict the nominal strength of the columns and compare it to experimental result.
- Conducting analytical study to assess the effect of increasing the concrete strength and the reinforcement ratio.

4.3. Materials

In this study, eight full-scale HSC columns were prepared and tested axially under four different eccentric load values. All the columns were made of HSC of an average compressive strength of 71 MPa. Four columns were reinforced using GFRP longitudinal bars and ties. While the other four columns were reinforced using steel bars and ties to serve as control specimens.

4.3.1. GFRP reinforcement

Sand-coated GFRP bars and ties (TUF-BAR/PB Composites, 2016) were used to reinforce the column specimens in the longitudinal and transverse directions, respectively as shown in Fig. 3.1. The GFRP reinforcements have a sand coated surface to enhance the bond performance between the bars and the surrounding concrete. No.6 (20 mm diameter) GFRP

bars were used as longitudinal reinforcement for all the GFRP-RC columns; No.3 (10 mm diameter) GFRP ties were used as transverse reinforcement. The tensile properties of the longitudinal GFRP were determined according to ASTM D7205/D7205M-06 (ASTM 2011), as reported in Table 4-1.

4.3.2. Steel reinforcement

Grade 60 steel bars were used to reinforce the steel reinforced control specimens. Deformed No. 6 and No. 3 steel bars were used as longitudinal and tie reinforcement, respectively. The mechanical properties of these steel bars were obtained by testing five representative specimens of each diameter according to ASTM A615/A615M-14 as shown in Table 4-1.

Table 4-1 – Mechanical properties of GFRP and Steel reinforcement

RFT type	Bar Size	d_b, mm	A_f [a], mm^2	A_{im} [b], mm^2	E_f, GPa	f_{fu}, MPa	ε_{fu}, %
GFRP	No.3	10	71	86.8 ± 3.6	63.7	1370[d] ± 23	2.2 ± 0.0
	No.6	20	285	309 ± 4.5	62.7	1236 ± 40	2.0 ± 0.1
Steel	10M	11.3	100	---	200	f_y [c] = 460 ± 10	ε_y [c] = 0.2
	20M	19.5	300	---	200	f_y [c] = 460 ± 15	ε_y [c] = 0.2

[a] Nominal cross-sectional area.
[b] Immersed cross-sectional area.
[c] f_y and ε_y are the yield strength and strain of the steel bars, respectively.
[d] Tensile strength of straight bar.
Note: properties calculated based on the nominal cross-sectional area

4.3.3. Concrete properties

The specified 71 MPa concrete was ready mixed. The concrete formulation was based on a water-cement ratio of 0.32. Cement type GUb-8SF was used for the concrete mix and it was premixed with silica fume, water reducer as shown in Table 4-2. The silica fume percentage was 9.4% of the mass. The slump was around 80 mm (before adding the superplasticizer). The concrete strength was determined in accordance with ASTM C39/C39M by testing 150 × 300 mm cylinders that were cured at the similar conditions of the casted specimens. The concrete cylinders had and average strength of 71.2 MPa at the same day of testing.

Table 4-2– Concrete mix properties

Composition	(kg/m^3)
Water	157
Cement	490
Sand	812
Crushed stone 10-5 mm	557
Crushed stone 20-5 mm	475
Density	2491

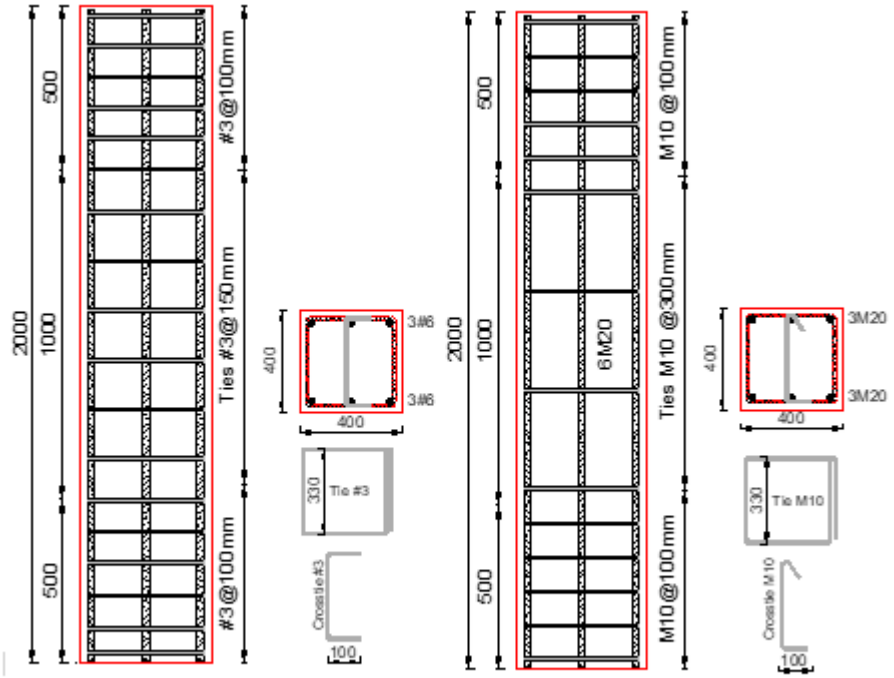

(a)

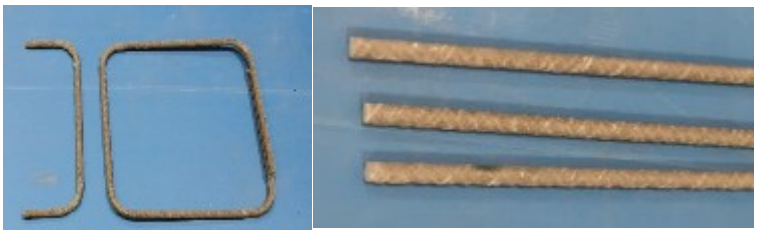

(b)

Figure 4-1 (a) Reinforcement details for column GFRP and steel reinforced columns. (b) overview of GFRP bars and ties.

4.4. Stress-strain Relationship for HSC:

Typical stress-strain curves were obtained for unconfined compression cylinders for HSC have different overall behavior compared to normal strength concrete (NSC). As the concrete increase in strength it exhibits (a) higher elastic modulus for the ascending part, (b) more linear response till the maximum stress, (c) higher strain at higher stress, (d) steeper unloading after maximum stress, and (e) sharply reduced ultimate strain capacity. All these changes depend on the target compressive strength for the concrete. Behavior of the curves past the peak stress behavior are depending on the end conditions of testing. Also, different properties changes with the increase of the compressive strength, such as rate of shrinkage, the stress strain model, Poisson's ratio, splitting tensile strength and creep.

4.5. Construction method:

Table 4-3 lists the test matrix for the eight RC columns reinforced with GFRP and steel bars. The first stage of construction involved preparation of the reinforcement bars and ties. The steel and GFRP bars were cut into 1950 mm length and were aligned using wooden formwork to have exact locations of the bars for all the columns. Tie wraps were used to fasten the ties to the bars, paying careful attention to spacing between ties and alignment of the bars on the compression and tension side. Strain gauges were then installed on the longitudinal bars at the mid height were maximum stresses are expected. Once glued to the longitudinal rebars, the strain gauges were covered with an epoxy layer. All the columns were casted on the same day using ready mix high-strength concrete with an average compressive strength of 71 MPa. The specimens were casted horizontally with tension and compression surfaces facing the sides of the formwork to avoid having different concrete strength between the compression and tension sides. They were then covered with wet burlap for curing and removing the sides of the formwork was done one day after casting. The water curing was continued for two successive weeks.

Table 4-3 – Test matrix

Series	Specimen ID	Test eccentricity (mm)	Longitudinal reinforcement	Transversal reinforcement
S	Se80	80	Steel 6M20	Steel 10M@300
	Se120	120	Steel 6M20	Steel 10M@300
	Se160	160	Steel 6M20	Steel 10M@300
	Se240	240	Steel 6M20	Steel 10M@300
G	Ge80	80	GFRP 6#6	GFRP #3@150
	Ge120	120	GFRP 6#6	GFRP #3@150
	Ge160	160	GFRP 6#6	GFRP #3@150
	Ge240	240	GFRP 6#6	GFRP #3@150

4.6. Specimen Design:

All the test specimen had a 400 × 400 mm square cross section and the height was 2000 mm giving an aspect ratio of 0.2 and length to width ratio of 5. These dimensions were selected to ensure the specimens are large enough to consider full-scale columns, while be easily handled without cracking. The specimens were designed to investigate the influence and the behavior of integrating GFRP reinforcements with HSC and test them under different magnitudes of eccentricities. The eccentricities were 80 mm, 120 mm, 160 mm, and 240 mm. These values were selected to ensure different and discrete points can be plotted to cover wide range of the interaction diagram representing the strength of the column under different eccentricities. The columns had reinforcement ratio of 1% of the concrete cross section which meet the minimum reinforcement ratio for flexural reinforcement as specified by ACI 440.1R-15 and ACI 318-14M. Ties were placed with spacing 150 mm for GFRP and 300 for steel RC columns. Additional ties were provided at the two ends of the specimens to prevent undesired failure in these zones. The effective length of the specimens was chosen to be considered as short columns. The columns had concrete cover of 35 mm. The columns were labeled according to the material used and eccentricity to width ratio.

4.7. Test setup and instrumentation

The columns were tested using MTS machine with an axial capacity of 11,000 kN. The ends of the columns were leveled to make sure they are horizontal and ensure uniform distributed load to the entire surface, also, both ends of the columns were capped with high strength grout layer. Then each side of the columns was attached to the setup separately. Steel plates were used to fill the gap between the tension side of the column and the setup. While grout was poured between the compression face of the columns and the setup. To apply eccentric load on the column, two loading heads were made with high-strength steel plate. The loading head transfers the load from the MTS machine to the column through the ball joint to provide hinged boundary condition. The loading head parts were fastened together using high strength bolts. Then the loading head provides the required length to transfer the moment due to eccentricity to the entire length of the column. The columns were tested under loading rate up to 70% of the predicted maximum load then switched to displacement control. Vertical displacement was measured as the head movement of the MTS testing machine using the data acquisition system. The lateral displacements were measured at the mid height and at the ends of the testing zone, quarter height, using 3 LVDTs. Concrete strain gauges were mounted on the compression surface of the column before testing. The MTS machine, strain gauges, and LVDTs readings are all connected and recorded using the data acquisition system. A photo of a typical eccentric testing is shown in Fig. 3.2.

Figure 4-2 – Test setup elevation and side view.

4.8. Test results and observations:

4.8.1. Cracking pattern:

The test day average cylinder strength for the target strength was 70 MPa. The highest test-day average cylinder was 77 MPa. Results of the eight eccentrically loaded columns are tabulated in Table 4-4. The moment values given in the table were taken about the neutral axis including the secondary moments due to the second order effect resulting from the lateral deflection of the column. It can be noted that the secondary moment was minor compared to the primary moment form the initial eccentricity. The failure pattern of the columns subjected to eccentric loads is combining that for concentrically loaded columns and beam. It started with the appearance of tensile cracks start to appear throughout the length of the column. The number of cracks and their width is related to the value of moment applied and lateral deformation attained during loading. Then, the column reaches an ultimate load when cracks on the tension side are wide and the concrete on the compression side start to crush followed by cover spalling. The column experience reduction in strength as a result of failure part of the concrete section and shifting of the center of the gravity which increases the value of eccentricity applied to the column's section.

Table 4-4– Test matrix and summary of results

Series	Column ID	*e/h*	P_{peak} (kN.m)	e (mm)	Δ (mm)	M_I (kN.m)	M_{II} (kN.m)	M_{tot} (kN.m)	$P_{bar,peak}$ (kN)	$P_{bar,peak}/P_{peak}$ (%)	GFRP ε_t ($\mu\varepsilon$)
G	Ge80	0.2	5100	80	4.89	408	25	433	44	0.9	930
	Ge120	0.3	3621	120	5.84	434	21	455	60	1.7	3000
	Ge160	0.4	2457	160	13.35	393	33	426	58	2.3	6190
	Ge240	0.6	1367	240	19.71	328	27	355	37	2.7	9050
S	Se80	0.2	5137	80	3.8	411	19	411	140	3.7	N/A
	Se120	0.3	4213	120	7.03	506	30	506	130	3.1	N/A
	Se160	0.4	3019	160	8.12	483	25	483	81	2.6	N/A
	Se240	0.6	1338	240	15.21	321	20	321	70	5.2	N/A
G*	CGA80	0.2	3354	80	4.8	268	16	284	90	2.6	430
	CGA160	0.4	1943	160	9.2	311	18	329	85	4.4	3000
S*	CS80	0.2	3815	80	5.9	305	22	328	396	10.4	N/A
	CS160	0.4	2318	160	9.0	371	21	392	396	17.1	N/A

Notes: e is eccentricity; h is column width; P_{peak} is peak axial load; M_I is the moment due to applied eccentricity; M_{II} is the secondary moment due to the deflection; $P_{bar\ peak}$ is the bar contribution; and GFRP ε_t is the maximum achieved tensile strain in the GFRP bars at the peak load. * Specimens reported by Guérin et al. (2018)

The cracking pattern for column Ge80 appeared at a load value of 5,100 kN (37% of the maximum axial load). The applied loads exist on the boundaries of the cross-sectional kernel, making the cross section is mostly under compressive stresses and small values of tensile stresses. The cracks started to grow wider and propagate perpendicular to the longitudinal reinforcement as the load continued to increase. No cover spalling and few tensile cracks were observed before reaching the peak value. At the peak load, the concrete on the compression side failed in an explosive and brittle manner causing spalling of the concrete cover at the mid height. No failure was observed for the GFRP reinforcement. After cover spalling, the column suffered sudden loss 34% of the column strength. On the other hand, for steel reinforced column Se80 the column achieved maximum axial strength of

5,137 kN. Both columns achieved similar value and over all demonstrate the same failure process. The first cracked was visible at an approximate load of 2,200 kN. The crack width was small due to the high axial force withstood by the column. After reaching the peak load, the compression reinforcement yielded and bigger area of concrete was crushed. This led to higher losses in strength for the post peak phase. Also, higher values of axial and lateral deformation were reached. Both columns, GFRP and steel reinforced columns, possessed the same number of horizontal tensile cracks.

Further increase of the eccentricity in column Ge120 lowered the peak load reached and increased the maximum moment. The column failed due to compression failure of the concrete surface at a concrete strain of 3,120 microstrains, while the maximum tensile strain recorded for GFRP bars was 2,930 microstrains. The cracking pattern on the tension side was similar to that of *e/h* 0.1 but the first crack appeared at an earlier stage at a load value of 500 kN (11% of the maximum load). The concrete on the compression side started cracking around 85- 90% of the maximum load. On the counter part, specimen Se120 had an axial resistance of 4,213 kN. At load of 250 kN the first crack was visible. For the post peak phase, the steel columns suffered for strength loss more than the GFRP as the compression steel yielded. It should be noted that the yielding of the steel didn't take place before reaching the maximum strength of the column.

Under high eccentric values, column Ge160 failed at an axial load value of 2,458 kN and at a concrete strain of 3,420 microstrain. Cracks on the tension side start to initiate at an early stage of loading at a load value of 340 kN (14% of maximum load). The cracks were more intense and rapidly initiated throughout the length of the column.

Specimen Ge240 started cracking at an early stage of loading. The first crack initiated at a value of 290 kN. Then the columns started to bent and forming a concave shape. The number of cracks appeared pre-failure, especially the tension cracks, have increases abruptly in number and width as the eccentricity is the largest in value compared to other columns. On the other side, the area of concrete spalling and crushing are the smallest. The maximum load carried by this column was 1,367 kN. Conversely, columns Se160 and Se240 had axial strength of 3,019 kN and 1,338 kN respectively. For Se160, the compressive reinforcement

yielded before reaching the maximum axial capacity. While wide tensile cracks appeared for columns Se240 indicating yielding of tensile steel. Once yielding strains reached by the tensile steel reinforcement, the cracks deformed wider and deeper decreasing the axial and lateral stiffens of the column. ACI 318-14M classify this as tensile failure of the flexural members although the ability of the column to resist more load. The yielding of the reinforcement led the column to acquire more cracks and lateral deformation. At load 1,338 kN the compressive concrete cover spalled and lost 67% of its strength.

In general, all the columns failed due to the crushing of the concrete on the compressive side and crack formation on the tension side. No rupture of bars either in compression or tension was observed, this is due to the high tensile strain of the GFRP bars $(\varepsilon_{fu} = 2.0\%)$. With small eccentricity, *e/h*=0.2, the column withstood large axial load and small moment and the column exhibited few tensile cracks which appeared at 56% of the peak load. With larger eccentricities the columns were carrying lower axial loads and more flexural bending moment due to the combined eccentricity from loading and the second moment effect, the column also showed ductile behavior until reaching maximum concrete strain at the compression surface. For high eccentricities, 0.6h, steel reinforced column failure was classified as tension failure. While for GFRP reinforced column, more tensile strains were still being resisted by the GFRP bars and the cracks grew wider and deeper. Nevertheless, both columns showed similar pre-peak behavior in terms of cracks number, width, axial strength and lateral deformation. Fig. 3.3, 3.4, and 3.5 show different view for the steel and GFRP reinforced column.

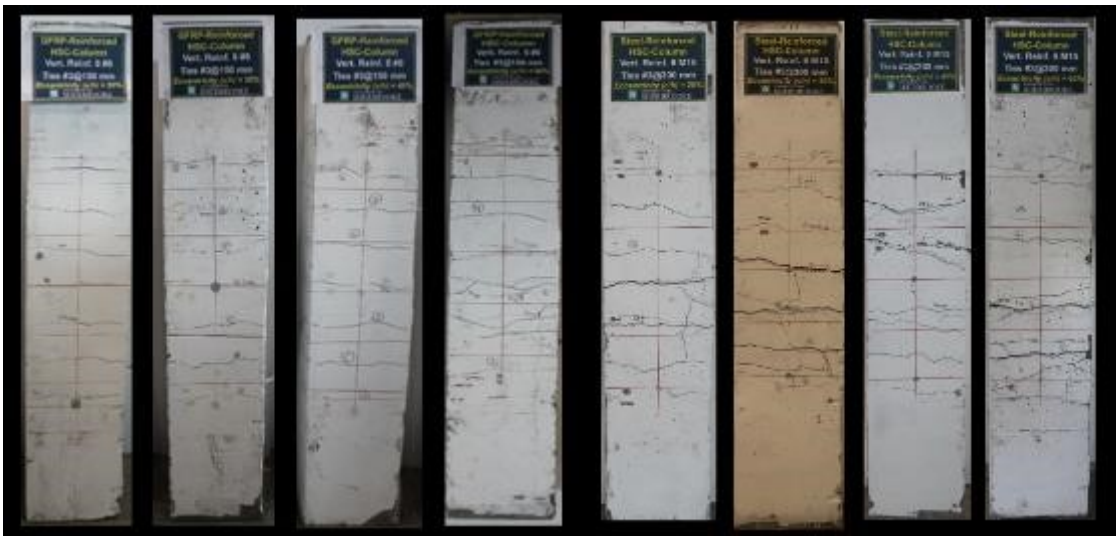

Ge80 Ge120 Ge160 Ge240 Se80 Se120 Se160 Se240

Figure 4-3 – Failure mode for group GFRP and steel reinforced columns series on tension side.

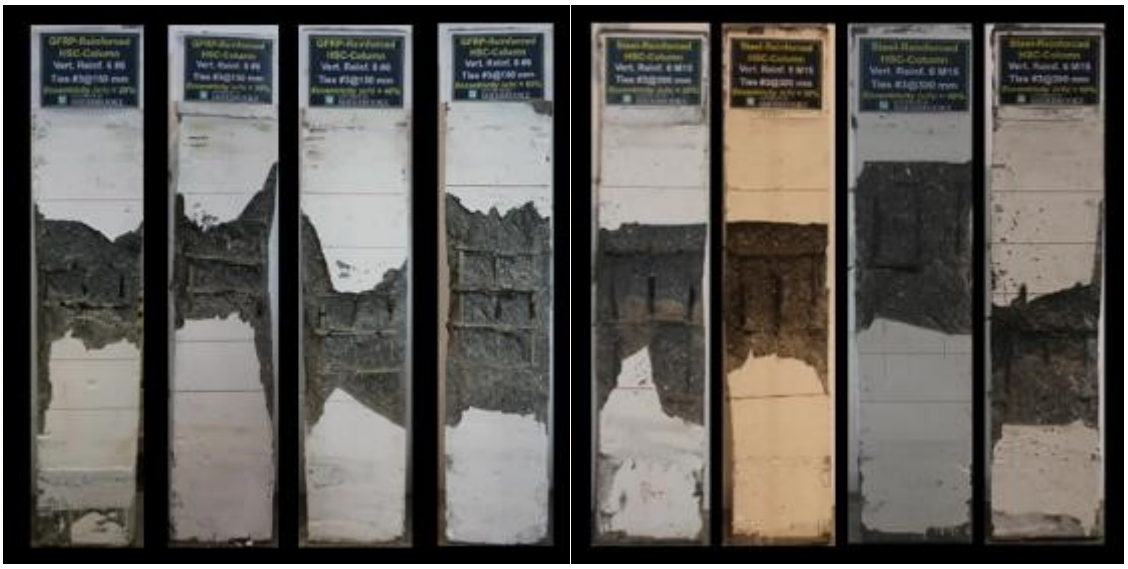

Ge80 Ge120 Ge160 Ge240 Se80 Se120 Se160 Se240

Figure 4-4 – Failure mode for group GFRP and steel reinforced columns series on compression side.

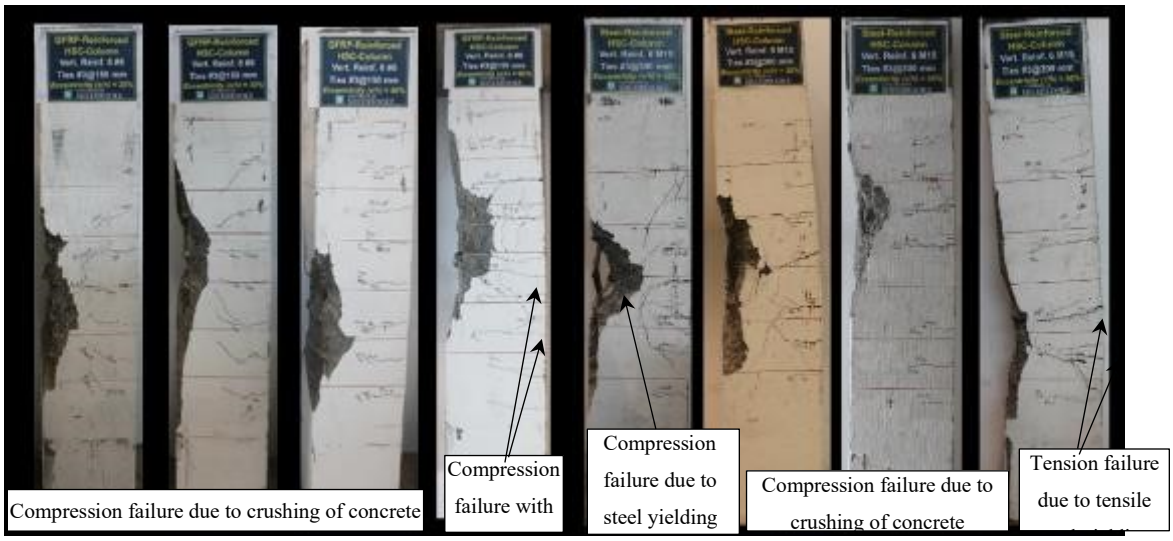

Ge80 Ge120 Ge160 Ge240 Se80 Se120 Se160 Se240

Figure 4-5 – Side view for the failure mode for group GFRP and steel reinforced columns series.

4.8.2. Axial and lateral deformation:

Fig. 3.6 provides the load versus the axial displacement response for all the columns. The axial displacement was measured during testing with a data acquisition system that is connected to the MTS machine used to test the different columns. Fig. 3.7 shows the load versus the lateral displacement at the mid height for the G series. Overall, using HSC increases the axial and lateral stiffness when compared to NSC. A significant change in the axial stiffness, which is represented by the slope of the charts, was observed with each different eccentricity. In general, as the eccentricity increases the axial and lateral stiffness decreases. Normally, all the columns have a linear initial linear branch up to certain load level then afterward the columns start the failure process by forming tensile cracks, which in turn gradually decreased the axial stiffness until reaching the peak load. For GFRP reinforced column with *e/h* equal to 0.2, 0.3, 0.4 and 0.6 the axial stiffness start degrading at 82%, 77%, 60% and 42% of the peak load. After this stage, the stiffness of the column gradually decreased up to reaching failure at the peak load. This gradual loss in the axial stiffness is a result of the crack formation on the tension side and the microcracks initiation

on the compression as the loading continues. The higher the eccentricity to width ratio the lower the column's axial stiffness it gets.

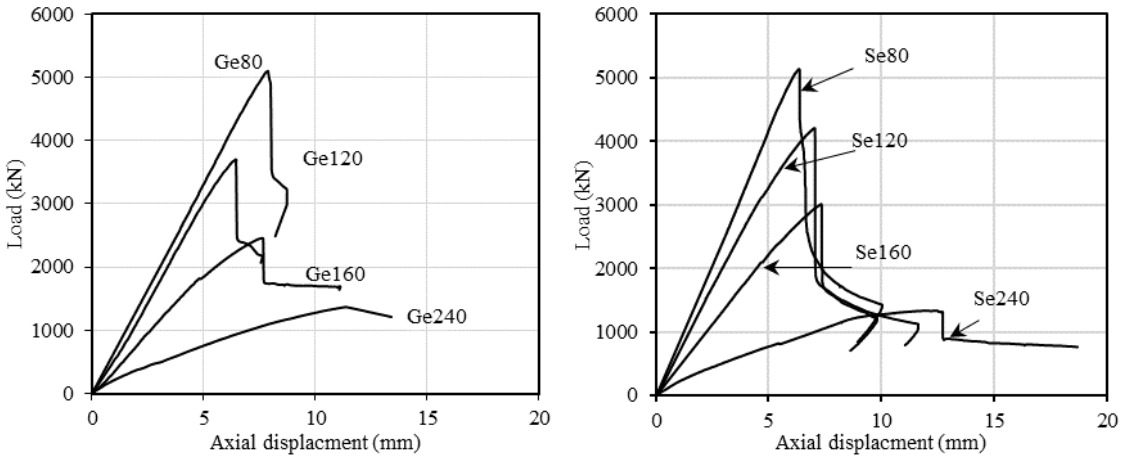

Figure 4-6 – Load versus axial displacement for GFRP and steel reinforced columns.

After failure the columns suffered from strength loss due to cover spalling on the compression side which in turn reduced the compressive area responsible to withstand the compressive stresses in the concrete section. The columns with *e/h* 0.2, 0.3, 0.4, 0.6 had reduction in strength of 34%, 32%, 29%, and 14% of the peak value respectively. The reduction in strength was greater in value with small eccentricity which withstood large axial capacity, while on the other hand, the reduction wasn't significant for small eccentricities. At the peak, the axial displacement was 7.58mm, 6.43, 7.61 and 11.32 mm for columns with *e/h* 0.2, 0.3, 0.4and 0.6 respectively. After the peak, variable strength decay developed according to the level of eccentricity. As the axial deformation increase, columns *e/h* 0.2 and 0.3 had less gradual loss of axial strength, while for columns *e/h* 0.4 and 0.6 had nearly constant axial capacity which was acquired by the elongation of the GFRP bars on the tension side.

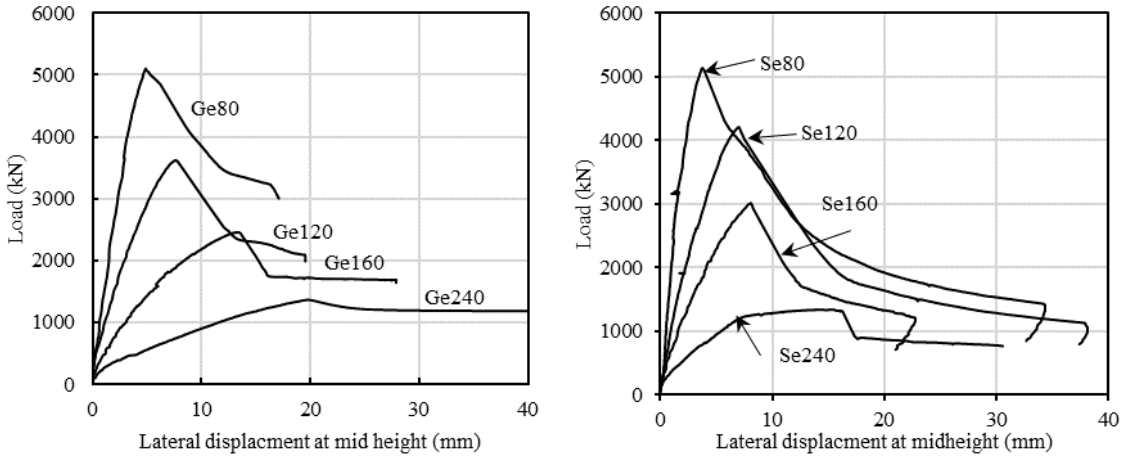

Figure 4-7 – Load versus lateral mid-height displacement.

4.8.3. Concrete strain:

Fig. 3.8 shows the concrete's strain response for columns with different eccentricities. The concrete strain gauges were installed at the mid height of the columns where the maximum compressive strains are expected. The slope of each curve is different and affected by the magnitude of the eccentricity applied during testing. Nevertheless, the concrete response was elastic till initiation of microcracks or flexural-tensile cracks. The slope of the curves then started to decrease in slope up to failure load. It can be noticed that for small eccentricity, i.e e= 80 mm, the concrete strains have the smallest values among all the other columns. This can be attributed to the fact that with small eccentricities the columns are resisting higher values of axial compressive force which facilitate the process of cover spalling. The maximum recorded concrete strains ranged from 1,870 microstrains for e=80 mm to 3,420 microstrains with eccentricity of 160 mm for GFRP columns. On the other hand, the steel reinforced columns had concrete strain values ranged from 2090 to 3140 microstrains. The columns tested eccentricities of 160 mm and 240 mm reached concrete strains close to the specified limit by the ACI 440.1R-15 (-3,000 microstrains). These recordings are a bit lower than the range for the known ultimate concrete compressive strain for extreme fiber in flexural members which ranges from 3,000 to 4,000 microstrains. Such a decrease in the maximum compressive strains is expected as the concrete compressive strength increases. This range comes in agreement with the experimental results obtained by

Kaar et al. (1977). They reported that the ultimate strain of plain concrete flexural members without lateral confinement decreased as the concrete compressive strength increased.

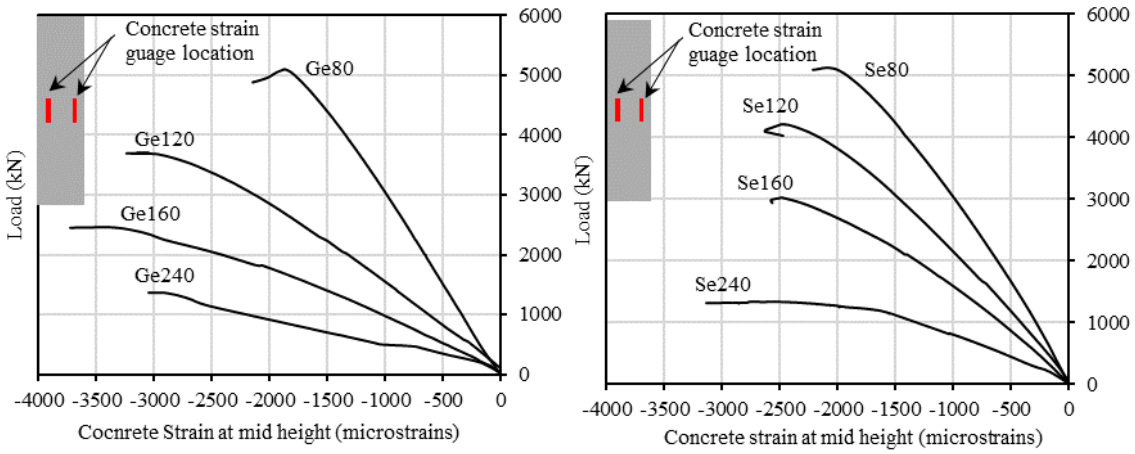

Figure 4-8 – Load versus concrete strain on the compression side.

4.8.4. Longitudinal GFRP-bar strain profiles:

To monitor the performance of the GFRP bars with high strength concrete, strain gauges were mounted on the bars at the mid-section to record the strain at the mid height. Fig. 3.9 shows the recordings for the compressive bars at the mid height section of the columns where the maximum recordings are expected. Also, Fig. 3.10 shows the recordings of the tensile bars on the opposite compression side. The results indicated that GFRP reinforcement developed high compression and tensile strain which exceeded the yielding strain of the steel reinforcement. This is attributed to the main difference between linear behavior of GFRP bars which allowed the strain recorded to exceed the yielding strain of steel bars. The compressive bars had semi linear response that gradually increase up to reaching the peak load. It should be noted that the strain at the peak load is nearly the same as the failure strain for the concrete. On the other side, the tensile bars start up with a linear response with very low strain up to the initiation of the tensile cracks which transfer the tensile loads to the bars after exceeding the tensile rupture modulus of the concrete. Then the tensile bars will increase semi linearly till reaching the maximum columns resistance.

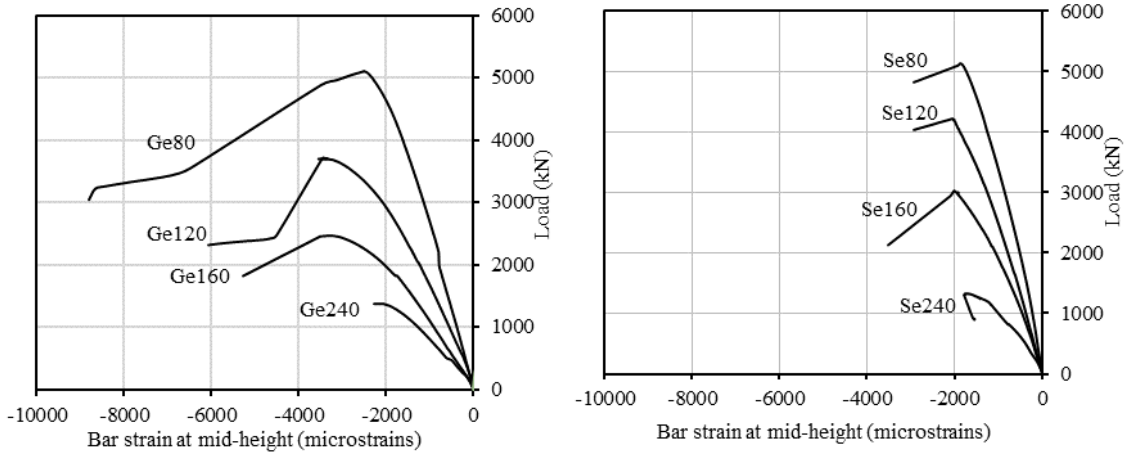

Figure 4-9 – Load versus outermost compressive bar strain at mid-height for GFRP and steel bars.

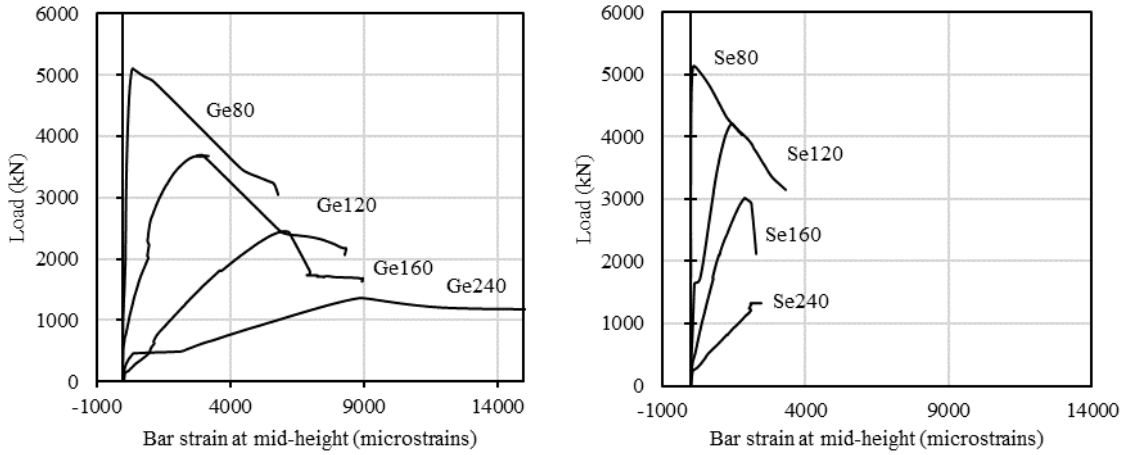

Figure 4-10 – Load versus outermost tensile bar strain at mid-height for GFRP and steel columns.

Columns with small eccentricity, e= 80mm, the column section was under compressive stresses and there were insignificant tensile stresses on the tension bars. This is a result of the axial force of loading is acting within the core area of the column. The steel columns had a compressive strain record of -1,860 $\mu\varepsilon$ (9.3% $\varepsilon_{u)}$ (at the peak load), while the tensile strain was 103 $\mu\varepsilon$. The GFRP reinforced column Ge80 reached compressive strain of -2,490 microstrains and tensile strain of 930 microstrains. (Guérin et al. 2018) stated that for the

same dimensions of the column and by using NSC the strain recorded was 450 microstrains (2.3% ε_u).When the peak load was reached, a compressive failure was marked by the crushing and spalling of the concrete on the compressive side. This caused the neutral axis of the column to shift and inducing more compressive strains on the outer most parts and sharp increase in the strain gain despite the drop in the axial load. The maximum recorded strain recorded for Ge80 was -8,790 $\mu\varepsilon$(44% ε_u) on the compression side and 5,820 $\mu\varepsilon$ (29% ε_u) on the tension side.

Column under eccentricity to depth ratio of 0.3h and 0.4h had most of the section under compressive stresses and small value of tensile stresses. Ge160 and Ge240 reached compressive strains of -3,340 (16.7% ε_u) and -3,260 microstrains (16.3% ε_u) respectively at the peak load. The compressive bars for these two columns had close strain values as the failure was governed mainly by the rupture and spalling of the concrete cover, with no sign of buckling or failure of the GFRP bars. At the same moment, the tensile bars possessed different tensile strains of 2,850 (14.3% ε_u) and 6,010 (30% ε_u) microstrains for Ge120 and Ge160 respectively. This difference in the tensile strain is attributed to the fact that column with *e/h* 0.4 had a higher moment at failure load as a result of larger applied eccentricity and lateral deflection at the mid height. (Guérin et al. 2018) mentioned that for sample CGB160 the maximum tensile strain recorded was 3,200 microstrains (16% ε_u). After failure, the tensile strain had a drastic drop in the load value. The loss in the axial strength is related to the maximum axial resistance reached by the column. The tensile bars were able to withstand the sudden shift of the neutral axis and were able to reach a plateau with no signs of slippage. The steel reinforced columns, Se120 and Se160, were only able to reach the yielding strains of 2,060 and 2,000 microstrain for the compressive bars. While for the tensile bars these columns recorded values of 1,460 and 2,240 microstrains for Se120 and Se160.

Under large eccentric loading, Ge240, the compressive bars behaved similarly to the previous cases with starting with semi linear behavior up to the maximum load. The strain recorded for the compressive bar at the maximum load was -2,040 microstrain. Columns with high eccentricity to depth ratio tend to experience cover spalling before the compressive bars reach value near to the concrete's maximum strain. The high deflection and curvature

experienced with these columns tend to assist the unbraced concrete cover to spall of the concrete core.

4.9. Discussion

4.9.1. Influence of test parameters

Three main parameters were under investigation in this study: the effect of increasing the concrete compressive strength, the effect of changing the eccentricity to depth ratio, and the effect of using GFRP vs steel reinforcement. It was observed that changing the eccentricity has a similar effect on GFRP and steel reinforced section in terms of axial, lateral deformation, and strength. While using GFRP reinforcement in place of steel bars altered the behavior of pre-peak phase in terms of number of cracks appearance and their width.

4.9.2. Efficiency of using high strength concrete:

In order to investigate the effect of increasing the concrete compressive strength, the results of the tested specimens is compared with the available test results in the literature of **normal strength concrete columns reinforced with GFRP ties and bars** (Guérin et al. 2018). In this research rectangular specimen with same dimensions, 400 mm width, and having a concrete strength of 42.3 MPa were tested under the eccentricity of 40, 80, 160, and 320 mm. for comparison purposes Specimens with centricity of 80 mm and 160 mm will be compared with the results of the tested specimens herein. Under the eccentricity of 80 mm, the axial capacity increased by 52 and 35% for GFRP type A and steel reinforced columns when the compressive strength increased from 42.3 to 70 MPa. The tensile strain for the tensile GFRP bars at the peak load increased by 115% for GFRP rebars type A and 6 % for steel reinforcement by using HSC with 70 MPa. While for eccentricity 160mm, the increase in axial strength was 26% and the tensile strain increased by 100% for GFRP type A. This level of eccentricity made the steel bars on the tension side to reach yielding strain for both normal and high strength concrete. In terms of lateral deflection, columns with reinforcement type GFRP A (CGA80) had deflection of 4.8 compared to 2.88 mm deflection for column Ge80 under the eccentricity level of 80 mm and at the same load level of 3354 kN. While

for eccentricity level 160 mm, the specimens CGA160 had lateral deflection of 7.9 mm compared to 9.2 mm for Ge80 at load level of 1,940 kN. For steel column, CS80 and CS160 had lateral deflections values of 5.9 and 9.0 mm at a peak load of 3,815 and 2,318 kN, respectively. The HSC exhibited less ductile manner as the lateral deflection values recorded at the same load level were 2.14 and 5.13 mm for columns Se80 and Se160, respectively.

The effect of increasing the concrete strength is demonstrated in the increased axial strength for the column's cross section and the column's axial and lateral stiffness (which is indicated by the slope of the load-deflection plots in Fig. 3.6). Using HSC allows the designers to use smaller concrete column's cross sections to resist a given axial load. But, it also decreases the ductility of the reinforced members as the maximum lateral deflection reached is less than that for NSC (as shown by comparing the lateral deflections at the same load level). It should be also noted from Table 4-4 that the steel and GFRP rebars contribution in compression ranged between 2.6% to 5.2%, and 0.9% to 2.7%, respectively. It should be noted that these values are lower than those stated by other researchers (Guérin et al. 2018; Luca et al. 2009). Increasing the compressive strength of the concrete caused the concrete to have higher Young's modulus which lowered the axial force resisted by the bars during loading.

4.9.3. Eccentricity to depth ratio

The main objective of this study is to determine the behavior of GFRP bars with HSC columns under different eccentricities. Four values for eccentricities were selected to study different behaviors and the corresponding failure mechanism. The GFRP columns had similar manner in terms of peak load and reaching a comparable axial and lateral stiffness compared to steel columns under same eccentricities. After reaching the peak load the G series columns lost an average of 67%, 65%, 71%, and 88% of the peak load at eccentricities to depth ratio of 20%, 30%, 40%, and 60%. The failure modes of the columns tested under low, moderate and extreme eccentricities were concluded to be classified as compression failure due to the crushing and spalling of the concrete cover at the peak load. No crushing in the GFRP bars was observed upon reaching the maximum resistance load of the column. While for steel reinforced columns, the failure mode changed from compressive and tension

failure at low and high eccentricities respectively. It can be noted from Fig. 3.3 that the steel column had wider cracks as a result of steel yielding after failure while for GFRP the crack width was much smaller in comparison. Increasing the eccentricity gradually change the column behavior from having high axial load with high axial and lateral stiffness to column subjected to high moment value and low axial force which resulted in lower axial resistance and lower axial and lateral stiffness.

For normal strength concrete columns, the failure pattern was similar to those made with HSC. The HSC columns demonstrated more brittle compressive failures compared to NSC columns. This is attributed to the higher strength resistance and properties of HSC. Moreover, as the eccentricity to depth ratio increases more flexural stresses are applied to the cross section which result in more tensile cracks and migration of the neutral axis along the section. As a result of using HSC, the columns suffered from higher axial strength loss with the increase of the applied e/h compared to columns made with normal strength concrete. this is shown in the Ge80 and Ge160 which had strength loss of 2640 kN with the increase of e/h form 0.2h to 0.4h compared strength loss of 1410 kN for specimens CGA80 and CGA160. The rate of strength loss decreases as the value e/h increase, as for short eccentricity the column's resistance depends mainly on the compressive block of the column's cross section. While for the steel specimens the Se80 and Se160 had strength loss of 2120 kN compared for strength loss of 1500 kN between CS80 and CS160.

4.9.4. Reinforcement type:

There is a major difference between steel and GFRP materials in terms of mechanical properties especially with the stress-strain behavior of these two materials. The GFRP is known to linear stress-strain trend, while for steel it has linear elastic stress strain until reaching the yield stresses at which the strain reaches a plateau of yielding. This difference in behavior was observed in the post-peak behavior of the columns. Steel columns exhibit lateral deflection higher than the GFRP reinforced columns due to yielding of the steel rebars. While the GFRP reinforced columns possess smaller cracks and smaller lateral deflection, despite the fact that the Young's modulus for GFRP bars is nearly 30% of that for the steel bars.

Using HSC allowed the GFRP reinforced columns to reach higher tensile strains in the bars which can be considered more efficient use of the GFRP bars. The maximum recorded tensile strains for specimens Ge80 and Ge160 were 930 and 6010 microstrains respectively. These tensile strains values are 116% and 100% larger than the tensile strain recorded by specimens CGA80 and CGA160 in which normal strength concrete were used, respectively. As for the compression bars, no signs of bar crushing were observed at peak resistance or even at the end of testing. both NSC and HSC had near compressive strain values (-2700 and -2900 microstrains for NSC compared to -2490 and -3260 microstrains for HSC at e80 and e160). On the contrary, steel compressive bars yielded and buckled towards outside the core of concrete which helped early spalling of concrete and the columns to exhibit large displacements axially and laterally due to the lack of resistance in the compression and tension bars. While columns reinforced with GFRP bars were able to resist the applied load at high tensile and compressive strains keeping the core concrete intact. Because of this the GFRP columns had lower axial and lateral displacement at the post-peak phase compared to the control steel reinforced specimens. It should be noted also by using HSC less lateral pressure is applied on the ties of the columns due to its lower Poission's ratio (reference). Moreover, steel reinforced columns had strength loss of 57%, 56%, 45%, and 34% for eccentricity to width ratio of 0.2h, 0.3h, 0.4h, and 0.6h respectively. Whereas for GFRP reinforced columns the strength losses were 34%, 32%, 29% and 14% for the same eccentricities values, respectively. These results clearly indicate that the GFRP bars can be safely used in columns even with HSC as they GFRP reinforced columns behaved similarly to steel reinforced columns at the pre-peak and post-peak phases.

4.10. Experimental P-M interaction diagrams:

Drawing the interaction diagram for GFRP reinforced concrete column is different than for steel reinforced columns. For steel reinforced column, the interaction diagram is divided into three main zones; compression-controlled region, transition, and tension controlled zone (ACI 318R-14). These zones are determined by both the compression concrete surface strain and the steel bar strain. For steel bars strain, the transition between zone lies between strains 0.002 and 0.005. These limits provide the necessary ductility for moment distribution along

the structural element. On the other hand, the interaction diagram for GFRP reinforced columns lack these limits due to linear elastic behavior of the GFRP bars.

In this study, four levels of eccentric loading were applied to two series of columns (series S and Series G). Based on the test results for each specimen, the P-M interaction diagram was developed as shown in Fig. 3.12 The nominal bending moment M_n is given by:

$$M_n = M_{n1} + M_{n2} = P_n \times e \; + \; P_n \times x \tag{3.1}$$

Where P_n is the nominal axial force; e is the given eccentricity, and x is the lateral displacement at the peak load measured at the column's mid height. Fig. 3.11 shows that the interaction diagram for series S and G have similar values for small and large eccentricities (80 mm and 240 mm).

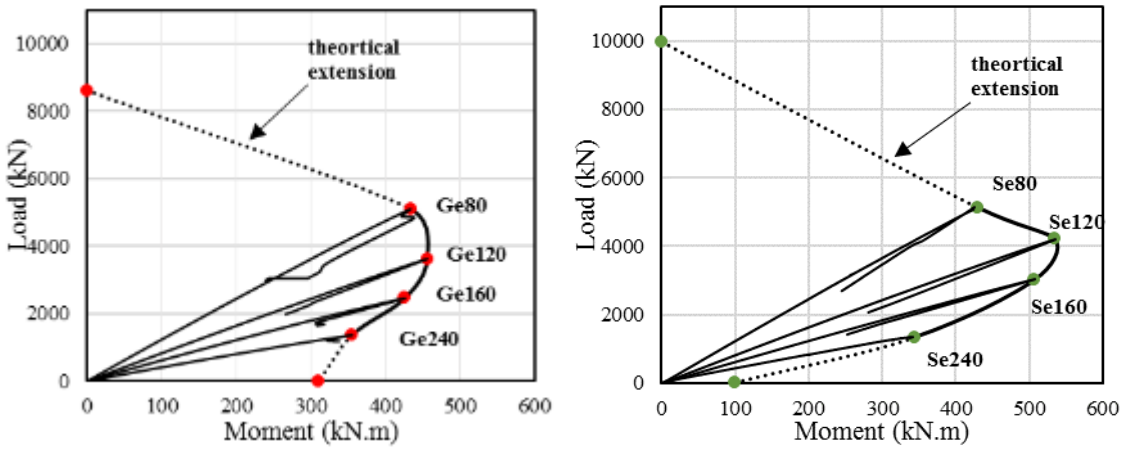

Figure 4-11 – Experimental results for GFRP and steel reinforced columns series.

4.11. Theoretical prediction:

An analytical study was performed to draw a full interaction diagram based on the current guidelines of ACI 440.1R-15 and CSA S806-12, then compare it with the experimental results for the tested specimens. It's worth mentioning that these codes have high limitation to use GFRP bars in compression elements. For the ACI it's advised not to rely on the FRP to resist compressive forces due to the lower modulus compared to steel. While the CSA allowed the use of FRP bars in compression members but with deeming zero compressive

strength and stiffness. Other researchers recommended substituting the FRP bars with concrete. This study considered layer by layer approach and force equilibrium to develop the interaction diagram for GFRP reinforced columns. In order to perform this method, the cross section was divided into ten layers. The thickness of the layers is equal to the depth of the square cross section divided by the number of the layers. Then, the maximum strain 0.0035 is assumed to be reached at the outer most layer. Based on the test results, the strain distribution in all the specimen was almost linear up to reaching the maximum column's resistance, which proves the assumption of plane section remains plane after deformation is a valid and true assumption. Fig. 3.12 shows the strain distribution for all the G series columns at the peak load. By taking that into consideration the average strain for the rest of the layers was determined and hence the stress is determined for each section. The concrete model used for high-strength concrete is explained below. The tensile stresses for the layers below the neutral axis were ignored. After that, the total forces for the layers in compression were added together. Then the strain corresponding to the level of the tensile and compression reinforcement was calculated to accounts for their forces. By doing that the nominal axial force (P_n) and the nominal moment was determined.

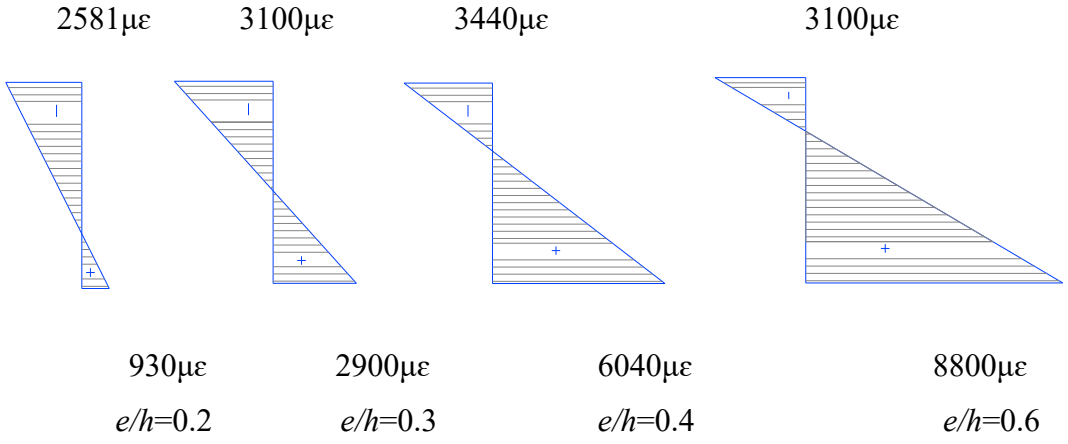

Figure 4-12 – Strain profile at peak load for G series under different eccentricities.

For a comprehensive analysis, the nominal axial and bending resistance were calculated under two different assumptions: 1) considering the full contribution of GFRP compression bars, 2) ignoring the contribution of the compression bars. According to the design codes, the maximum strain taken for GFRP bars was same as the maximum strain for concrete

(3,000 for ACI and 3,500 for CSA). The same assumptions used for designing steel reinforced column were adopted for GFRP reinforced columns. Based on the following assumption the theoretical interaction diagram was drawn.

1) Assuming perfect bond between GFRP bars and concrete, which means that the GFRP bars and the concrete have the same strains.

2) Strength factor for GFRP bars and concrete are set to unity.

3) The maximum Strain used is 3500 as advised in CSA S806-12, and the tensile strength of concrete is ignored,

4) The nominal axial resistance is calculated based on the following equation (assuming that the strain in the GFRP bars is equal to the ultimate assumed concrete strain):

$$P_o = P_c + P_f = \alpha_1 f_c^{'}(A_g - A_f) + 0.0035 E_f A_f \tag{3.2}$$

Unconfined high strength concrete stress-strain model:

The strain response is different for HSC concrete than that for NSC. A convenient expression for the ascending part of the curve was proposed by Popvics in 1973

$$f_c = f_c^{'} \frac{\varepsilon_c}{\varepsilon_c^{'}} \frac{n}{n - 1 + (\varepsilon_c / \varepsilon_c^{'})^n} \tag{3.3}$$

and for the descending part Thorenfeldt et al., (1987) suggested the addition of factor k to accurately predict the descending part as follows:

$$f_c = f_c^{'} \frac{\varepsilon_c}{\varepsilon_c^{'}} \frac{n}{n - 1 + (\varepsilon_c / \varepsilon_c^{'})^{nk}}, \tag{3.4}$$

$$n = 0.8 + \frac{f_c^{'}}{17} \text{ (MPa)}, \tag{3.5}$$

$$k = 0.67 + \frac{f_c^{'}}{62} \text{ (MPa)}, \tag{3.6}$$

$$\varepsilon_c^{'} = \frac{f_c^{'}}{E_c} \frac{n}{n - 1}. \tag{3.7}$$

Where ε_c is the axial concrete strain at any concrete stress; f_c' is the unconfined concrete maximum stress at age of 28 days; ε_c' is strain when f_c reaches f_c' is the maximum stress; n is curve fitting factor that is responsible for the ascending slope; k is factor for the descending branch's slope; and E_c is the elastic modulus of concrete (ACI 2014)

4.11.1. Development of theoretical interaction diagrams:

This section presents the assumptions used to plot the nominal interaction diagram for the axial and bending moment based on two different scenarios. In these two scenarios, the contribution of the compression reinforcement is being ignored in one of them and considered in the other.

Scenario A: Ignoring the contribution of GFRP bars in compression.

In the first scenario, the nominal axial load and flexural resistance can be calculated as:

$$P_n = P_c - T_f = \sum_{n1}^{nt} tbf_i - \varepsilon_{fj} E_f A_f \tag{3.8}$$

$$M_n = M_c \pm M_t = \sum_{n=1}^{nt} f_i \left(\frac{h}{2} - (n - \frac{t}{2})t\right) \pm \varepsilon_{fj} E_f A_f \tag{3.9}$$

Where t is the thickness of the layers used, b is the width of the square cross section; $\varepsilon_{fj}, E_f, A_f$ = strain in the tensile bars, Young's modulus and area of reinforcement. Refer to Fig. 3.13 for the cross section layer by layer method symbols and explanation.

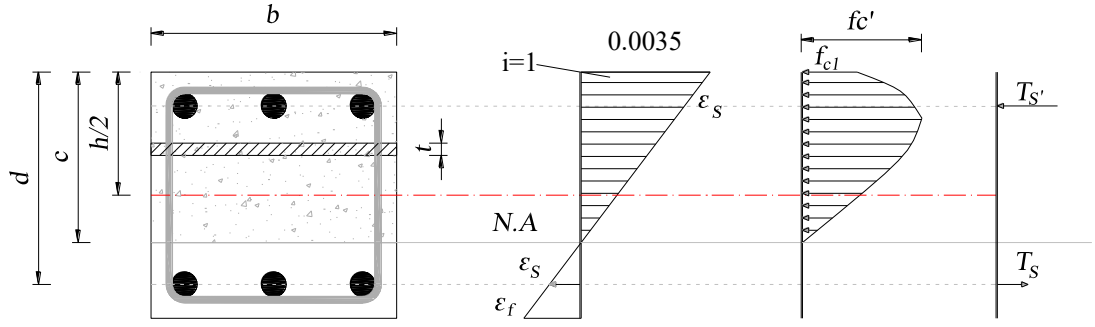

Figure 4-13 – Stress and strain assumption for strip method analysis.

Scenario B: considering the contribution of GFRP reinforcement in compression:

The previous equations are modified to account for the compression reinforcement by adding their compression forces. In this scenario the Young modulus for the compression forces is assumed to be equal to the tensile Young's modulus.

4.12. Comparing the experimental and theoretical results:

Fig. 3.14 plots and compares the experimental results for the tested GFRP reinforced columns with the theoretical model calculations by plotting the P-M interaction diagram for the same cross section using the previously mentioned scenarios. Values for scenario (B), in which the contribution of GFRP reinforcement in compression was fully considered, had closer values to the experimental results compared to scenario A. Scenario B had axial and flexural prediction close to the experimental results by 6-10%. While scenario A, which ignored the contribution of the compression reinforcement, was close to the experimental results by 10-16%. Based on these results, it can be concluded that the experimental results are in better agreement with the predicted results when considering the contribution of the compression forces. While ignoring their contribution may be considered as a much conservative method to be used which provide a safe margin for designers.

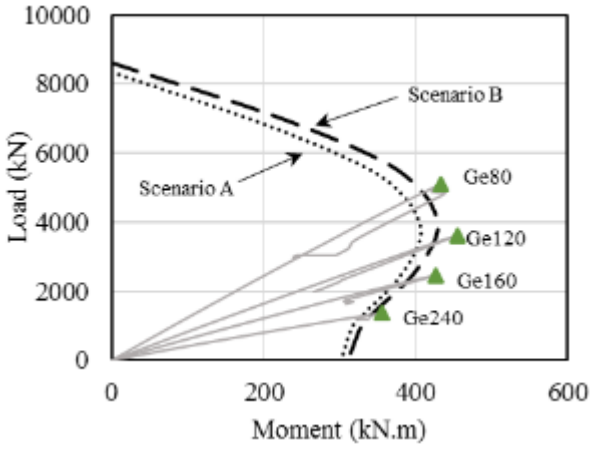

Figure 4-14 – Axial-Moment interaction diagram for experimental vs predicted results.

4.13. Parametric investigation:

In this section, the effect of the concrete strength, reinforcement ratio and the contribution of the compression reinforcement is studied, Fig. 3.15. A sectional analysis was used on square columns with the same cross section as the tested specimen (400 × 400 mm). The concrete strengths of 70, 80, 90, and 100 MPa were used with GFRP reinforcement ratios ranging from 1 to 4%. The results were plotted as shown in Figure 3.15.

4.13.1. Effect of increasing the longitudinal reinforcement ratio:

The influence of changing the reinforcement ratio of the column was different depending on the level of eccentricity and the contribution of compression reinforcement (scenarios A and B). By using scenario B, the reinforcement effect was more pronounced throughout the interaction diagram, especially for small eccentricities where most of the column's cross section is under compression. Ignoring the contribution of compression reinforcement, scenario A, concealed any difference in values for the upper part of the interaction diagram. The upper part is representing the small eccentricities, ($e<h/6$), where most of the cross section area is under compressive stresses. In fact, by increasing the reinforcement ratio larger area is subtracted from the concrete which reduces the resulting compressive forces for the concrete.

As for large eccentricities, the difference in values for scenario A was gradually increasing until reaching the flexural strength of the cross section which represents the beam case. On the other hand, using method B increased the capacity of the cross section compared to method A. The difference in values between each reinforcement ratio calculated using scenario B was nearly the same throughout the lower part.

4.13.2. Effect of the concrete strength:

The impact of changing the concrete strength is obvious for all the plots in figure 3.15. By increasing the concrete compressive strength, more axial resistance is provided by the uncracked concrete on the compression side. Also, the flexural capacity is increased with

using concrete of higher strength due to the nature of the GFRP which can sustain higher tensile strains compared to the steel reinforcement. It should be noted that with the use of higher concrete strength, the contribution of compression reinforcement diminishes as the young modulus of the concrete becomes close to that for the GFRP compression bars. Which means that as the used concrete acquires higher compressive strength, the contribution of the compression reinforcement becomes insignificant compared to it. Which reduce the difference in values between Scenarios A and B.

4.13.3. Effect of ignoring the contribution of bars in compression:

According to the current guidelines (ACI 4401R-15 and CSA S806-12), it's recommended to ignore the contribution of GFRP reinforcement in compression. As can be seen from Fig. 3.15, by ignoring their contribution there will be no significant change in the axial capacity of the columns with low eccentricity. This assumption may be valid for structure members under axial loads with high eccentric values or under flexure moments only. This is due to the fact that the neutral axis is close to the compression reinforcement and their contribution, in this case, will be insignificant. But in case of column subjected to pure axial loads or axial load with small eccentricity, where most of the cross section is under compressive forces, the contribution of the compression reinforcement should be ignored to increase the level of conservatism.

Using HSC will result in providing greater compressive strength to resist external forces. The contribution of the compressive GFRP bars compared to the HSC compressive strength is relatively low due to the fact that the GFRP bars and the HSC have small difference in the Young's modulus and the maximum strain reached by the bars is the same maximum strain of the concrete which limits the maximum axial force that can be resisted by the bars before the peak load. The gap in strength between using the different scenarios decreases with the use of concrete with higher compressive strength. A good assumption to be followed is the one suggested by (Choo et al. 2006b) when performing analysis and design which recommend ignoring the GFRP bars compressive contribution in sectional analysis.

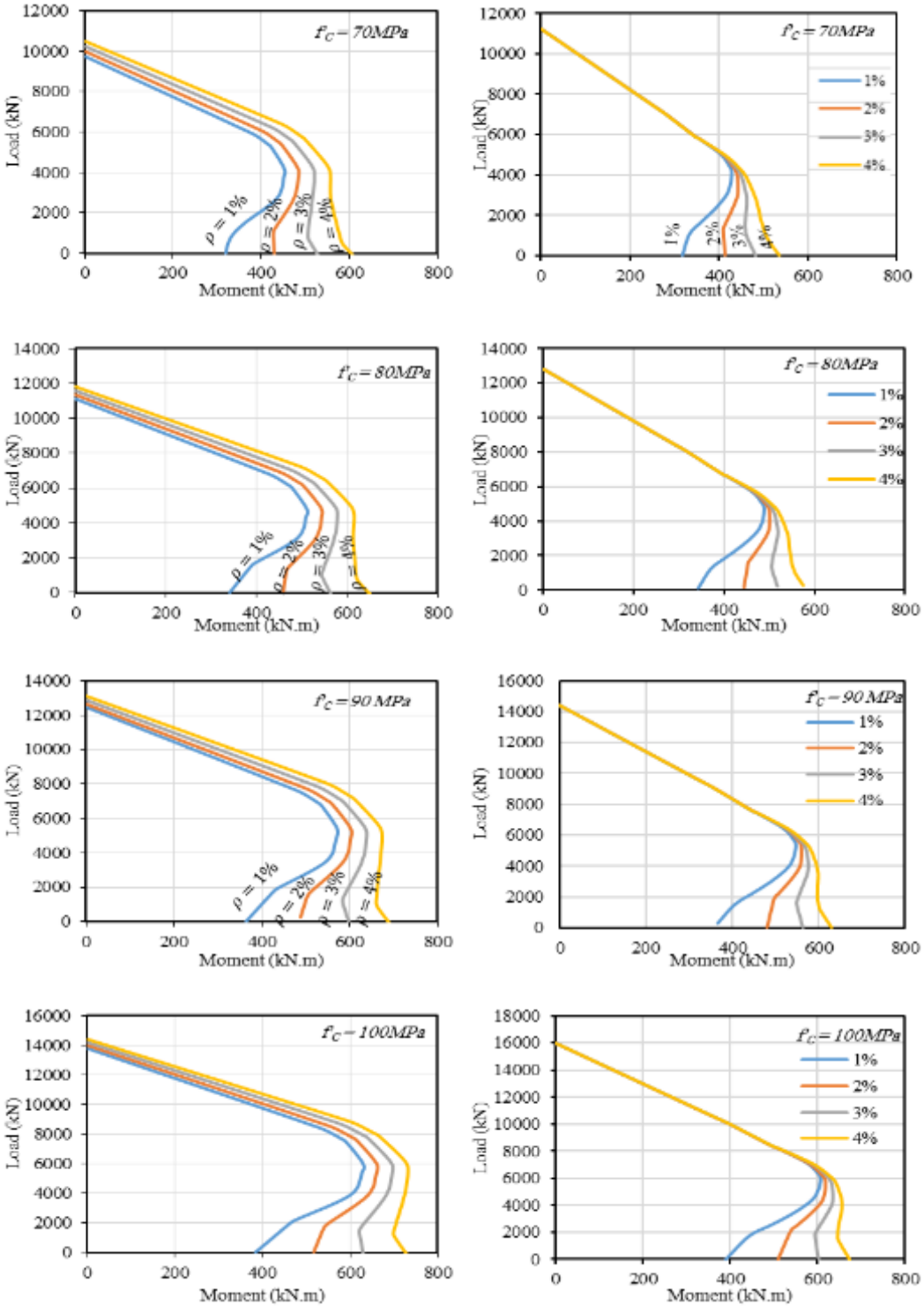

Figure 4-15 – Theoretical interaction diagram for square section (400×400) (a) considering te contribution of GFRP bars in compression (b) ignoring the contribution of GFRP bars in compression.

4.14. Conclusions:

The following conclusions have been drawn from the research presented in this study:

a) Integrating GFRP reinforcement with HSC columns achieved close axial resistance to columns with steel reinforcement for eccentricity to depth ratio of 0.2*h* and 0.6*h*. No appreciable difference was observed in terms of column's strength. The GFRP reinforced columns was more ductile and experienced more lateral and axial deformation when compared to steel reinforced columns under the same eccentricity.

b) As expected, increasing the concrete compressive strength increased the column's axial and flexural strength. Higher tensile strains were developed in the GFRP bars at the peak load levels which increased the axial and flexural strength of HSC columns when compared to NSC columns.

c) Both type of reinforcement showed stable and ductile behavior for the post-peak descending branch. The GFRP reinforced columns have a longer post peak and smaller loss in strength compared to steel reinforced columns for all the tested eccentricities. This is mainly due to the nature of GFRP to sustain higher strains compared to the yielding strain of the steel bars. The steel reinforced columns suffered loss strength ranging from 43% to 67% for eccentricity to depth ratio of 0.3h and 0.6h. GFRP reinforced columns had post-peak losses ranging from 14% to 34% for 0.2h and 0.6h respectively.

d) The range of concrete strain achieved in steel reinforced columns was 2,090 to 3,140 με, while for GFRP reinforced columns was 1,870 to 3,420με.

e) Loading with small to medium eccentricity, 0.2h,0.3h, and 0.4h, the failure of GFRP RC columns failed due to crushing of the concrete cover at the peak load under all the tested eccentricities. Similar failure mode was observed for the steel reinforced counterpart, columns under the same eccentricity levels. For high eccentricity level, *e/h*=0.6, the GFRP reinforced column experienced deep and wide cracks and experienced 30 % increase in lateral deformation compared to the steel reinforced column at the peak load. At the same level of eccentricity to depth ratio, the steel bars

on the tensions side reached yielding strain which caused the cracks to grow excessively wide and the columns to exhibit large lateral deflection. Similar failure process and behavior for both GFRP and steel reinforced columns were observed at e=0.6h.

f) Using HSC allowed the GFRP bars to be more efficient as they were able to reach higher tensile strains at higher peak load levels compared to NSC. Also, no rupture was observed for the GFRP bars under compression for all the tested eccentricities as most of the compressive stresses were resisted by the extra strength gained by using HSC.

g) Using layer by layer approach predicted axial and flexural strength values close to the experimental results. Considering the contribution of the GFRP bars in compression resulted in more reliable predictions, while it's advised to replace the area of GFRP bars with concrete in case their contribution is accounted for.

CHAPTER 5 AXIAL–FLEXURAL PERFORMANCE OF HSC BRIDGE COMPRESSION MEMBERS REINFORCED WITH BFRP BARS AND TIES: EXPERIMENTAL AND THEORETICAL INVESTIGATION

Foreword

Authors and Affiliation:

- Ashraf Salah-Eldin: Ph.D. candidate, Department of Civil Engineering, Université de Sherbrooke, Sherbrooke, Quebec, Canada, J1K 2R1.
- Hamdy M. Mohamed: Research Associate/Lecturer, Department of Civil Engineering, Université de Sherbrooke, Sherbrooke, Quebec, Canada, J1K 2R1.
- Brahim Benmokrane: Professor, Department of Civil Engineering, Université de Sherbrooke, Sherbrooke, Quebec, Canada, J1K 2R1.

Journal Title: (Journal of Bridge Engineering, ASCE)

5.1. Abstract

The forthcoming editions of the North American highway bridges design codes and guidelines will include complete sections with provisions on designing non-prestressed-concrete compression members (columns, piles, and piers) reinforced with FRP bars subjected to combined axial and flexural load. This paper presents the results of a research program investigating the use of newly developed sand-coated basalt-FRP (BFRP) bars and ties in axial–flexural members made with high-strength concrete (HSC). Eight full-scale concrete columns 400×400 mm in cross section and

2,000 mm in height were constructed and tested. The test variables were eccentricity-to-depth ratio and reinforcement type (BFRP and steel bars and ties). The test results indicate that the specimens reinforced with BFRP bars and ties under different levels of eccentricity behaved similarly to their steel-reinforced counterparts. An analytical study was conducted to predict the axial–flexural capacity. A parametric study was introduced to examine the effect of increasing the reinforcement ratio and concrete strength. Moreover, the effective flexural stiffness was estimated and plotted at different load levels and compared to design-equation results. The findings of this investigation can be considered as a fundamental step toward developing code provisions for using BFRP bars and ties as internal reinforcement in bridge pier and pile applications.

Keywords: Compression members, columns, piles, concrete, eccentric loading, high-strength concrete, Basalt FRP (BFRP) reinforcement, interaction diagram, sectional analysis, stiffness.

5.2. INTRODUCTION

Heavily loaded structures, such as bridges and high-rise buildings, require additional attention from designers regarding durability issues, choosing the right materials, and reducing maintenance costs. For bridges, using high-strength concrete offers many advantages that could help reduce construction costs and increase structure service life. It allows for smaller cross sections due to its higher compressive strength, reduced creep and shrinkage, lower deflection due to a higher modulus of elasticity, and increased durability as well as enhanced physical- and chemical-deterioration resistance (Smadi et al., 1987; Mokhtarzadeh and French, 2000). HSC has been increasingly used in precast bridge elements, thereby facilitating and shortening bridge construction (Mokhtarzadeh and French, 2000; Dolan and LaFraugh, 1993). Despite these advantages, HSC is still subject to steel-corrosion problems, which reduces service life and durability. The United States Federal Highway Administration (FHWA) estimates that eliminating the nation's bridge deficient backlog by 2028 would require an investment of $20.5 billion annually because of corroded steel and steel reinforcement. Also, Report Card for America's Infrastructure states that "The U.S. has 614,387 bridges, almost four in 10 of which are 50 years or older. 56,007 — 9.1% — of the nation's bridges were structurally deficient in 2016, and on average there were 188 million trips across a structurally deficient bridge each day (Mirza and Ali 2017; ASCE 2017). To overcome this problem, fiber-reinforced-polymer (FRP) reinforcement is being used extensively as a replacement for steel reinforcement in US and Canadian bridges. It is also

considered an economical, less-disruptive solution compared to retrofitting structural elements after degradation has occurred.

Bridge piers and piles are considered the most critical elements since they support and carry vertical loads. In most cases, bridge piles and piers are situated in waterways or near a marine environment, subjecting them to a high rate of corrosion yet making them hard to access for maintenance or repair. Using FRP can avoid high repair costs and constitute a durable, cost-effective replacement for steel reinforcement. Valuable research has been carried out in recent years on the behavior of glass-FRP (GFRP) bars in compression members. Afifi et al. 2014; De Luca et al. 2010; Tobbi et al. 2014; and Hadhood et al. 2017a tested square and circular concrete columns reinforced with GFRP and demonstrated the viability of using GFRP in axially loaded RC members for bridge pile and pier applications. The contribution of the GFRP bars in compression was reported to range from 3% to 10% of the total load-carrying capacity of the RC columns compared to 12% to 16% for steel reinforcement. Hadhood et al. (2017b) tested full-scale columns made with HSC and reinforced with GFRP bars and spirals tested under concentric and eccentric loading. Their results indicate that increasing the GFRP-reinforcement ratio enhanced the stiffness of the concrete columns. Guérin et al. (2018a) tested and reported experimental data for full-scale square concrete columns reinforced with GFRP bars and ties. The columns were tested under four different values of eccentricities. Their performance was compared to four control specimens reinforced with steel bars and ties. The test results indicated that the steel- and GFRP-reinforced concrete columns behaved similarly and that GFRP bars and ties could be used effectively in compression members.

Recently, basalt-FRP (BFRP) has emerged as a promising alternative to conventional FRPs in reinforcing concrete structures (Elgabbas et al. 2015 and 2016). BFRP bars show advantageous mechanical and chemical characteristics as well as a higher performance–cost ratio compared to other FRPs. For instance, BFRP has higher strength and modulus at a similar cost; greater chemical stability than E-glass FRP; a wider range of working temperatures; and much lower cost than carbon FRP (CFRP) (Brik 1997; Sim et al. 2005). It has also shown to perform better in an acidic environment (Wei et al. 2010) and provide five times the strength and approximately one-third the density of commonly used low-carbon steel bars (Wu et al. 2010; Sim et al. 2005; Palmieri et al. 2009). Because of these characteristics, BFRP bars were chosen for the HSC columns in this study.

5.3. ADVANCES IN RESEARCH ON BFRP-REINFORCED CONCRETE MEMBERS

Several researchers have investigated the performance of BFRP as internal reinforcement in concrete members. The latest BFRP research is summarized below for each BFRP element.

BFRP reinforcement bars: Elgabbas et al. (2015) tested three types of BFRP bars in an alkaline solution at high temperature (60ºC) to simulate the corrosive environment of concrete. The results showed that the BFRP bars met the physical and mechanical properties specified in ASTM D7957 and CSA S807-10. Furthermore, they could be placed in the same category as grade II and grade III GFRP bars (CSA S807-10). Their tensile strength was reported to exceed that required in CAN/CCSA S807-10 for CFRP bars.

BFRP-reinforced slabs: In addition, Elgabbas et al. (2016) tested full-scale edge-restrained concrete deck slabs reinforced with BFRP bars. The test parameters included different boundary conditions for the slabs, reinforcement ratios, and bar sizes. Based on the test results, the BFRP-reinforced concrete bridge-deck slabs evidenced punching-shear failure at corresponding loads higher than the factored designed loads in CSA S806-12. The authors concluded that BFRP reinforcement could be used in bridge-deck slabs and could be designed using the same design considerations as GFRP bars. Mahroug et al. (2014) tested continuously and simply supported concrete slabs reinforced with BFRP bars with different reinforcement ratios. These specimens were compared with steel-reinforced control specimens. The provisions of CSA S806-12 yielded reasonable deflection predictions for the test specimens.

BFRP-reinforced beams: Tomlinson and Fam (2016) evaluated the flexural and shear performances of concrete beams reinforced with BFRP rebar and ties. They found no significant differences in the load–deflection response within the service-load range between the steel and BFRP ties. They also mentioned that the beams with BFRP reinforcement had 2.6 to 2.9 times the flexural strength of the steel-reinforced counterparts in the case of tension-controlled specimens. Ovitigala et al. (2016) conducted an experiment with eight BFRP-reinforced beams. The beams had different reinforcement ratios and were divided into three categories: light, medium, and heavy reinforcement. All the tested beams failed by concrete crushing at the top compression zone. El Refai et al. (2015) tested 10 concrete beams with no transverse reinforcement. They concluded that

the beams with BFRP bars behaved similarly to beams reinforced with glass- or aramid-FRP (AFRP) bars. Moreover, it was found that CSA S806-12 provided the most accurate predictions for the concrete strength of beams reinforced with BFRP bars. Gribniak et al. (2015) evaluated the performance of beams reinforced with BFRP bars, in particular, their cracking and deflection response. No bond failure was observed between the concrete and BFRP bars. Moreover, their findings indicated a perfect bond between the BFRP bars and concrete, so that the deflection could be accurately assessed.

BFRP-reinforced columns: Fan and Zhang (2016) tested short columns reinforced with BFRP bars under eccentric loads. The columns measured 120 mm ×120 mm × 900 mm. The concrete compressive strength used was 34.9 MPa. The results indicated that the load-carrying capacity of the BFRP-reinforced concrete columns was 30% lower than that of the steel-reinforced concrete columns. They concluded that both the basalt- and steel-reinforced columns behaved similarly under small and large eccentricities.

In summary, to date, no experimental research has been reported concerning the axial–flexural behaviour of HSC columns reinforced with BFRP bars and confined with BFRP ties. Therefore, research is needed to develop experimental data and provide a sound basis for making design recommendations for inclusion in the new design codes. This paper reports on the test results of full-scale HSC columns reinforced internally with BFRP bars and ties.

5.4. AIMS AND OBJECTIVES OF THE STUDY

The forthcoming editions of the *AASHTO LRFD Bridge Design Guide Specifications for GFRP Reinforced Concrete – 2nd Edition* (2019) and the *Canadian Highway Bridge Design Code – Edition 2019* (CAN/CSA S6-19, 2019) will include valuable provisions for designing concrete columns and piers with FRP bars, spirals, and ties. Moreover, most of the design provisions are based on tests involving normal-strength concrete. The research reported on herein aimed at generating experimental data on the axial-flexural strength of full-scale concrete members made with high-strength concrete (HSC) and reinforced with BFRP bars and ties. This will help provide a better understanding of the failure mechanics and behavior of BFRP reinforcement in HSC members. In addition, an analytical model was developed to predict the nominal strength for use in assessing the effect of increasing the concrete strength and reinforcement ratio. The study also

aimed at assessing the performance of BFRP-reinforced concrete columns with respect to the reference HSC columns reinforced with steel bars. Additionally, the test results were compared to the available design provisions and recommendations. The test results can be used to evaluate and explore the feasibility of using BFRP bars and ties as internal reinforcement for RC bridge pier and pile foundations. The experimental evidence from this study provides a compelling case to include design provisions in the future edition of the *AASHTO LRFD Bridge Design Guide Specifications for GFRP Reinforced Concrete* and the *Canadian Highway Bridge Design Code* for the use of BFRP bars and ties.

5.5. EXPERIMENTAL WORK

5.5.1. Material Properties

BFRP bars (No. 6; 19 mm diameter) were used as longitudinal reinforcement on the tension and compression sides and No. 4 (13 mm diameter) BFRP ties were used as transverse reinforcement. Crossties were used at the center of the cross section with tail lengths equal to 12 d_b (d_b is the tie diameter). The BFRP bars were manufactured from continuous basalt fibers impregnated in vinyl-ester resin using the pultrusion process with a fiber content of 81% (by weight) (Pultrall, 2017). The ultimate tensile strength, $f_{fu,}$ and the modulus of elasticity, E_f, of the longitudinal BFRP bars (No. 6) and the straight portion of the bent BFRP bars (No. 4) were determined according to ASTM D7205. To determine the Young's modulus and compressive strength for the BFRP bars, sand-coated #6 BFRP bars were tested under compression according to ASTM D695 - 15 with an MTS machine. Different lengths of BFRP coupons were cut and prepared for testing. The free length of the specimens varied from 2D (where D is the bar diameter) up to 8D. These lengths were chosen to consider the shortest length specified by ASTM up to reaching the maximum spacing between the BFRP ties in the columns. For consistent and repeatable results, the same rate of loading (1.3 mm/min) was used in testing all the bars. The ends of the coupons were sawn perpendicular with a rotating water saw. Three specimens were tested for each length, and the average compressive strength and compressive modulus calculated. The bars failed in a crushing-failure mode in the middle zone with no buckling of the BFRP bars observed at all the tested lengths. The results indicate that the BFRP bars had an average compressive strength of 500 MPa and compressive

Young's modulus of 57 GPa, which is close to the tensile-rupture modulus. Figure 4.1 shows the tensile and compressive properties of the specimens tested.

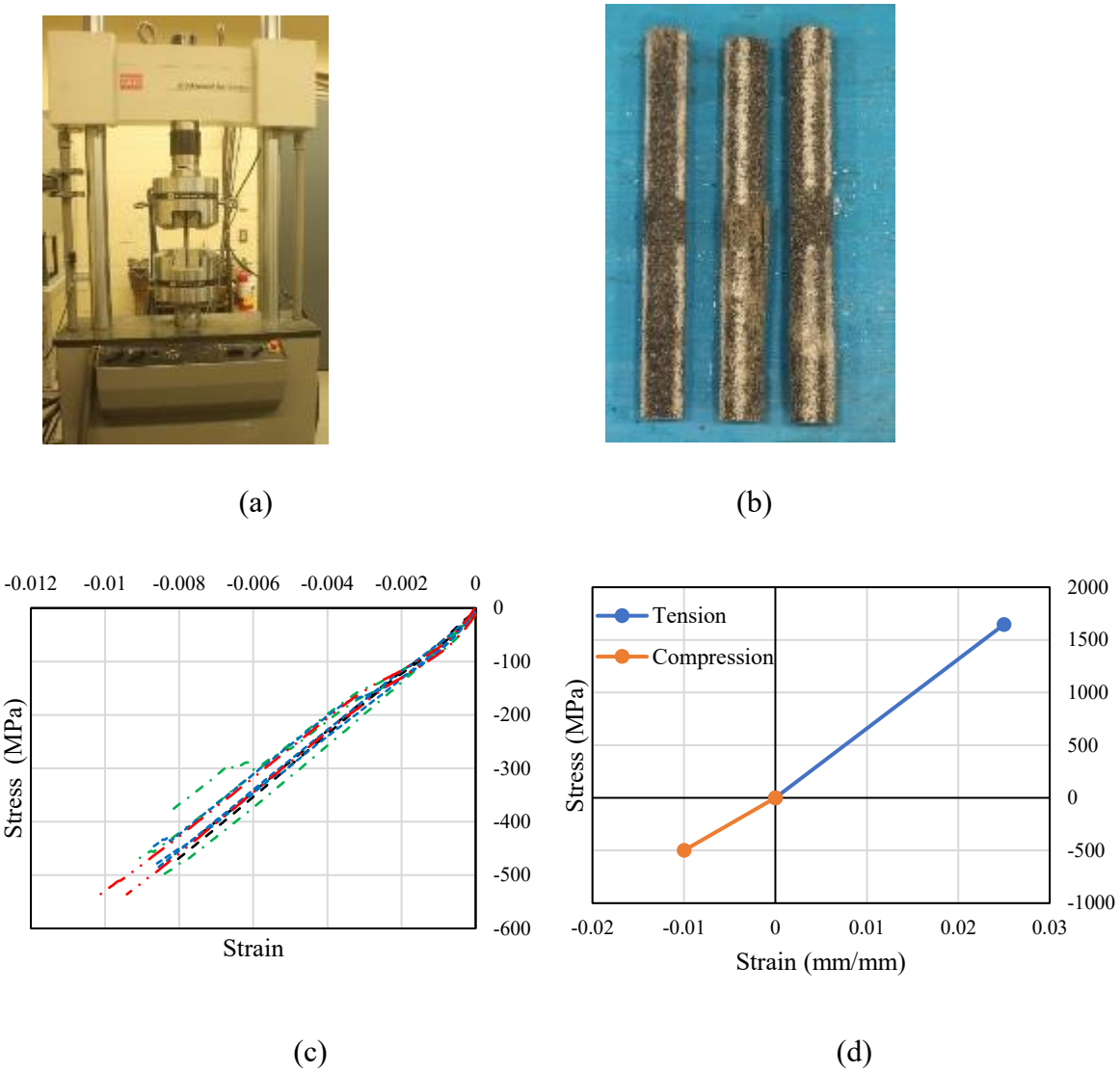

Figure 5-1 – Compression test for BFRP bars (a) test setup, (b) typical crushing failure, (c) stress–strain relationship for all the BFRP bars tested under compression, (d) average stress–strain used for tension and compression.

The steel reinforcement consisted of grade 60 steel bars used in the control specimens. Deformed M20 steel bars were used as the longitudinal reinforcement and M10 for the ties. The mechanical properties of these steel bars were obtained by testing five representative specimens of each diameter according to ASTM A61/A615M-14. Table 5-1 provides the properties and dimensions of both the steel and BFRP bars.

Table 5-1 – Mechanical properties of the BFRP and steel reinforcement

RFT Type	Bar Size	d_b, mm	A_f [a], mm^2	A_{im} [b], mm^2	E_f, GPa	f_{fu}, MPa	ε_{fu}, %
BFRP	No. 4	13	129	139 ± 0.80	51.4±0.20	1414 [d] ±11	2.70±0.2
	No. 6	20	285	346 ± 2.2	63.7±0.80	1646±40	2.50±0.1
Steel	10M	11.3	100	---	200	f_y [c] = 460 ± 10	ε_y [c] = 0.2
	20M	19.5	300	---	200	f_y [c] = 460 ± 15	ε_y [c] = 0.2

[a] Nominal cross-sectional area.

[b] Immersed cross-sectional area.

[c] f_y and ε_y are the yield strength and strain of the steel bars, respectively.

[d] Tensile strength of straight bar.

Note: properties calculated based on the nominal cross-sectional area

5.5.2. Concrete

The specimens were all cast with ready-mixed concrete with a water-to-cement ratio of 0.32. The cement was Type GUb-8SF, which was premixed with silica fume and water reducer, as shown in Table 5-2. The silica-fume percentage was 9.4% by mass. The slump was around 80 mm (before adding the superplasticizer). The concrete strength was determined in accordance with ASTM C39/C39M by testing 150 × 300 mm cylinders that were cured under conditions similar to that of the specimens. The concrete cylinders had an average strength of 71.2 MPa on the day of testing.

Table 5-2 – Concrete mix properties

Composition	(kg/m^3)
Water	157
Cement	490
Sand	812
Crushed stone, 10–5 mm	557
Crushed stone, 20–5 mm	475
Density	2491

5.5.3. Test Specimens

This research is a part of a project at the University of Sherbrooke, which includes extensive experimental tests on members reinforced with BFRP bars under pure axial load, pure flexural testing, and members tested under combined axial–flexural loads. The present study reports on original research work focused on an experimental investigation of the eccentric behavior of square HSC columns reinforced with BFRP bars and ties. Full-scale columns were made with HSC: four were reinforced with BFRP bars and ties and four with steel reinforcement as control specimens. All the columns measured 400 × 400 × 2,000 mm. The concrete cover was kept constant at 35 mm for all specimens. Each group of columns with the same type of reinforcement was tested under four different eccentricity-to-depth ratios (0.2, 0.3, 0.4, and 0.6*h* where *h* is the depth of the square section). The four eccentricities were used to develop the experimental P–M interaction diagrams with a wide range of eccentricities from small to large. The eccentricities were selected to cover as many points in-between under axial- and flexural-stress behavior: e/h = 0.2: small eccentricity (compressive stress behavior is dominant); e/h = 0.3-0.4: medium eccentricity (compressive-tensile stress behavior is the dominant transition zone); e/h = 0.6: large eccentricity (tensile-stress behavior is the dominant transition zone: flexural behavior). The applied eccentricity values were selected to provide data about the eccentric behavior of square HSC columns with BFRP reinforcement and draw its corresponding P–M interaction diagram. The axial and pure flexural capacity of the columns were determined theoretically, as explained in the section on theoretical analysis. Table 5-3 provides the test matrix and the column reinforcement details. Each specimen was labelled so as to indicate the reinforcement type and applied eccentricity. The letters B and S identify specimens reinforced with BFRP or steel, respectively. The numbers 80, 120, 160, 240 after the *e* symbol represents the applied eccentricity in millimeters. The reference steel-reinforced concrete columns had the minimum amount of longitudinal reinforcement and the minimum tie cross-sectional area at maximum spacing ($16d_b$, where d_b is the bar diameter).

Table 5-3 – Specimen details.

Series	Col. ID	*e* (mm)	*e/h* (%)	Reinforcement	
				Longitudinal	Transverse
Basalt	Be80	80	20	6 No. 6	No. 4 @ 150 mm
	Be120	120	30	6 No. 6	No. 4 @ 150 mm
	Be160	160	40	6 No. 6	No. 4 @ 150 mm
	Be240	240	60	6 No. 6	No. 4 @ 150 mm
Steel	Se80	80	20	6 20M	10M @ 300 mm
	Se120	120	30	6 20M	10M @ 300 mm
	Se160	160	40	6 20M	10M @ 300 mm
	Se240	240	60	6 20M	10M @ 300 mm

The same longitudinal reinforcement ratio (1% A_g, where A_g is the gross area of the column's cross section) was used for the BFRP-reinforced concrete specimens with three BFRP bars (No. 6) on each side of the column. As specified by ACI 318-14's maximum tie spacing ($16d_b$), as per Sections 10.7.6.1.2 and 25.7.2.1, was reduced to $8d_b$ for the BFRP reinforced columns to account for the difference in moduli of elasticity between BFRP and steel reinforcement (Guérin et al. 2018a and b; De Luca et al. 2010). The tie spacing for the steel-reinforced columns was chosen to consider the allowable maximum tie spacing, as provided in ACI 318-14. On the other hand, the tie spacing for the BFRP–reinforced columns was designed considering the recommendations given by Nanni et al. 2014; De Luca et al. 2010; Guérin et al. 2018a and b. According to Nanni et al. (2014), "the spacing is related to the diameter of tie bars to achieve a desired level of concrete confinement at the core of the column." From this viewpoint, De Luca et al. 2010 suggested that, in the case of GFRP-reinforced concrete RC columns, the tie spacing in ACI 318-11—controlled by tie diameter—must be halved from 48 to 24 tie-bar diameters given GFRP's lower stiffness. The tie spacing was reduced to 50 mm at both ends of the columns to avoid premature failure. The column dimensions and tie spacing were chosen to match the specimens tested by Guérin et al. (2018a) at the University of Sherbrooke in order to compare with their results. It should be noted that the columns tested were subjected only to applied axial and flexural forces. The diameter of the BFRP ties used was 13 mm. Figure 4.2 shows the reinforcement details for both column series.

5.5.4. Instrumentation and Test Setup

The compressive and tensile strains induced in the reinforcement bars during testing were measured with electrical resistance strain gauges mounted at the middle of the reinforcement bars. The tensile

strains were measured at the quarter- and mid-height of the columns; the compressive strains were measured at the mid-height of the columns. A total of six electrical strain gauges were used to monitor the strains along the BFRP rebars. The horizontal deflection was measured with linear variable displacement transducers (LVDTs) fixed at three different points along the column: mid-height and the top and bottom quarter of the column. Moreover, two strain gauges were mounted on the surface of the concrete columns to monitor the compressive concrete strain at the surface. The loading, deflection, and strains in the concrete and reinforcement were recorded with an automatic data-acquisition system connected to a computer.

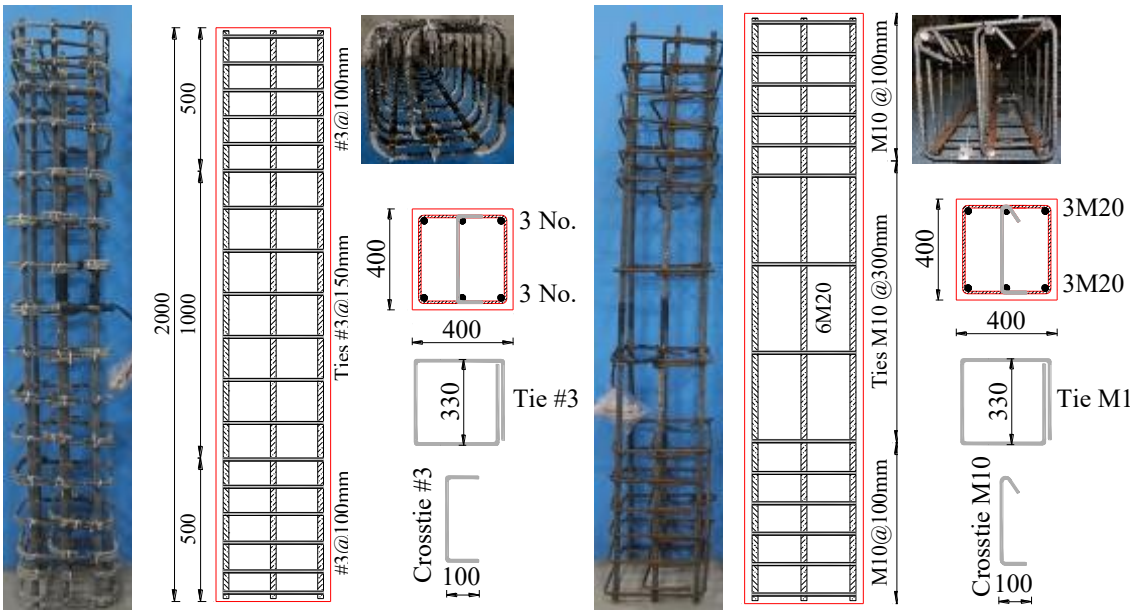

(a)

(b)

Figure 5-2 – (a) Configuration of BFRP- and steel-reinforced columns and reinforcement details and (b) overview of BFRP bars and ties.

Figure 4.3 shows the overview of the test setup. The test setup was designed and fabricated in the University of Sherbrooke's structural laboratory. Rigid steel caps were designed and fabricated to provide proper confinement and prevent premature failure of the end zones. The top and bottom surfaces of the columns were filled with high-strength cement grout to maintain full contact between the column sides and the end caps. The load was applied at the determined eccentricity using roller bearings attached to the steel end caps. The columns were monotonically loaded from the top of the column at a load control rate of 1.5 kN/sec until 70% of the load was reached. At that point, the MTS machine switched to displacement control with a rate of 0.002 mm/sec. The columns were observed visually during testing for cracks and the corresponding loads were recorded.

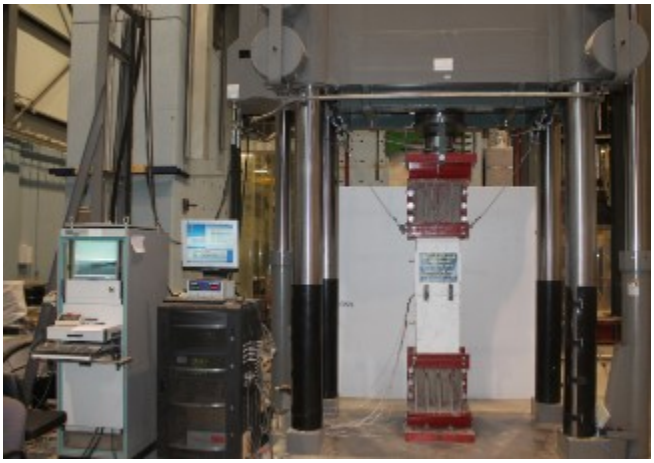

Figure 5-3 – Overview of the test setup.

5.6. TEST RESULTS AND OBSERVATIONS

Table 5-4 summarizes the test results obtained for all the columns tested. The following sections describe the behavior of the BFRP-reinforced columns under different levels of eccentricity and compare it to the steel-reinforced controls. Figure 4.4 shows an overview of the cracking pattern for the columns tested from three sides.

Table 5-4 – Test matrix and summary of test results

Series	Column ID	*e/h*	P_{peak} (kN)	e (mm)	Δ (mm)	M_{tot} (kN.m)	μ_e	$P_{bar,peak}$ (kN)	$P_{bar,peak}/P_{peak}$ (%)	BFRP ε_t ($\mu\varepsilon$)
B	Be80	0.2	4965	80	5.1	423	1.16	210	4.2	110
	Be120	0.3	3664	120	7.7	468	1.18	135	3.7	2210
	Be160	0.4	2356	160	11.2	403	1.20	126	5.3	4290
	Be240	0.6	1309	240	22.7	344	1.30	105	8.0	9270
S	Se80	0.2	5137	80	3.8	411	1.10	335	6.5	N/A
	Se120	0.3	4213	120	7.0	506	1.11	370	8.8	N/A
	Se160	0.4	3019	160	8.1	483	1.10	362	12	N/A
	Se240	0.6	1338	240	15.2	321	1.19	315	23	N/A
G*	CGA80	0.2	3354	80	4.8	284	N/A	90	2.6	430
	CGA160	0.4	1943	160	9.2	329	N/A	85	4.4	3000
S*	CS80	0.2	3815	80	5.9	328	N/A	396	10.4	N/A
	CS160	0.4	2318	160	9.0	392	N/A	396	17.1	N/A

Notes: *e* is eccentricity; *h* is column depth; P_{peak} is peak axial load; M_{tot} is the total moment due to the applied eccentricity and the secondary moment due to the deflection; $P_{bar\ peak}$ is the bar contribution at peak load; μ_e is the ductility index; and BFRP ε_t is the maximum achieved tensile strain in the BFRP bars at peak load. *Specimens reported by Guérin et al. (2018a)

5.6.1. Low Eccentricity (*e* = 80 mm)

The basalt- and steel-reinforced columns had similar behavior and failure modes when tested under an eccentric load of 0.2*h*. The concrete cover on the compression side was visually free of cracks until 90% of the peak load. The tensile cracking patterns initiated at column mid-height where the maximum moment is expected. More cracks appeared as the loading continued, increasing until reaching the failure load. The failure was identified by concrete-cover spalling on the compression side. The concrete strain gauges recorded readings of 2,040 με and 2,160 με for Be80 and Se80, respectively, as shown in Fig. 4.5. Columns Be80 and Se80 sustained maximum loads of 4,965 kN, and 5,137 kN, respectively. Figs. 4.6 and 4.7 provide the load versus axial and lateral deflections, respectively. At peak load, Se80 had smaller axial- and lateral-deflection values (11.74 mm and 3.79 mm) compared to Be80, which reached axial and lateral displacements of 9.20 and 5.13 mm,

respectively. At peak load, the recorded average strain for the compression bars was -1,930 με and -2,680 με for Be80 and Se80, respectively, as shown in Fig. 4.8. The strain values for the steel bars on the compression side indicated that the steel bars had reached yielding strains before reaching peak load. This was also noticed for the tensile bars strains at the quarter height, as shown in Fig. 4.9. When the yielding strain was reached, the steel bars buckled outwards, which facilitated spalling of the concrete cover. This spalling led to axial-strength loss and a sudden increase in lateral deformation. The strength loss after peak load was 44% and 49% for Be80 and Se80, respectively. With the sudden drop in strength, the columns experienced more lateral deflection as the cover spalled. The steel-reinforced column experienced higher strength losses due to the bars yielding, so the columns could not withstand additional loads or reach a plateau for the post-peak phase. Conversely, in the case of column Be80, the test results indicate that the BFRP bars were effective in resisting compression until after concrete crushing on the compression side. The bars on the tension sides of Be80 and Se80 had negligible maximum tensile strains of 110 με and 103 με, respectively. This is because the initial eccentricity was within the kernel area of the column, which subjects the column cross section to compressive stresses. Figures 4.10, 4.11, 4.12, and 4.13 reveal significant tie-strain readings for the pre-peak phase.

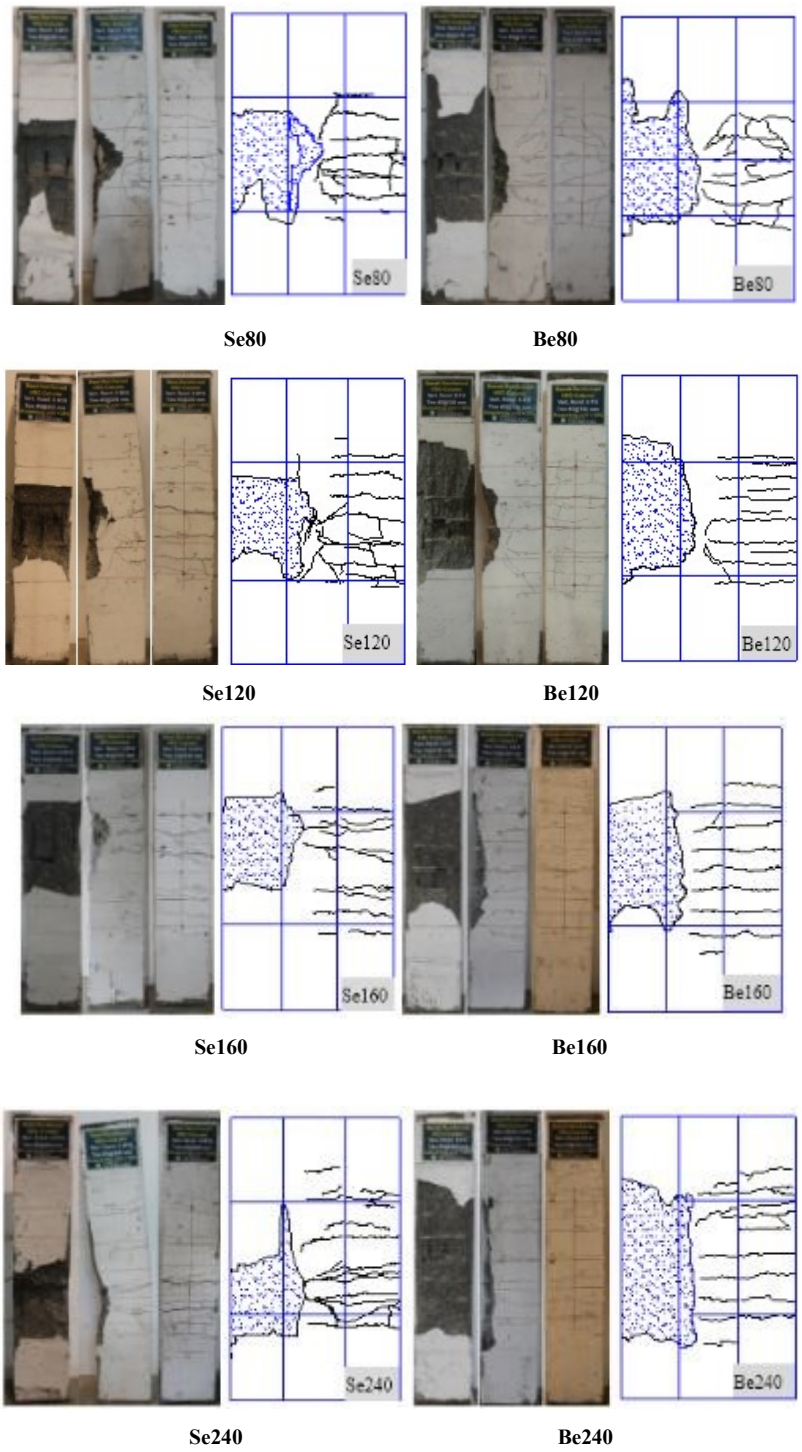

Figure 5-4 – Overview of cracking pattern for three sides of the tested columns.

The tie strain was due to lateral pressure from bar buckling and dilation of the concrete core. The lateral pressure applied by the concrete core increased significantly in the post-peak phase compared to the pre-peak phase. It should be noted that, due to the reinforcement yielding, the

steel-reinforced columns had larger concrete-crushing areas and permanent deformation even after load removal. In contrast, the BFRP-reinforced columns retained smaller axial and lateral deformation even after concrete-cover spalling. This self-centering behavior is advantageous for columns subjected to lateral loads such as during earthquakes. Moreover, wider cracks were observed in the steel-reinforced column in the post-peak phase.

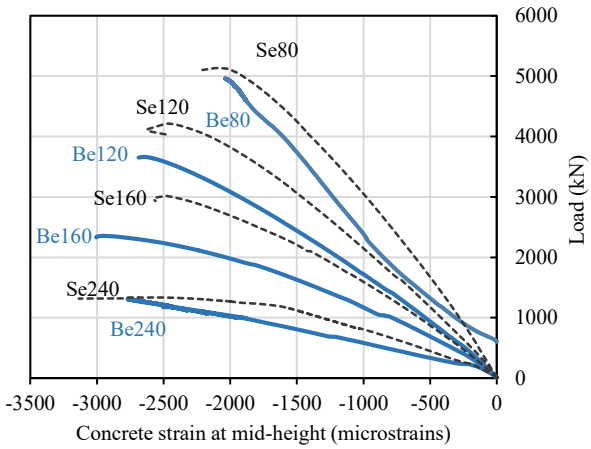

Figure 5-5 – Load versus concrete strain on the compression side.

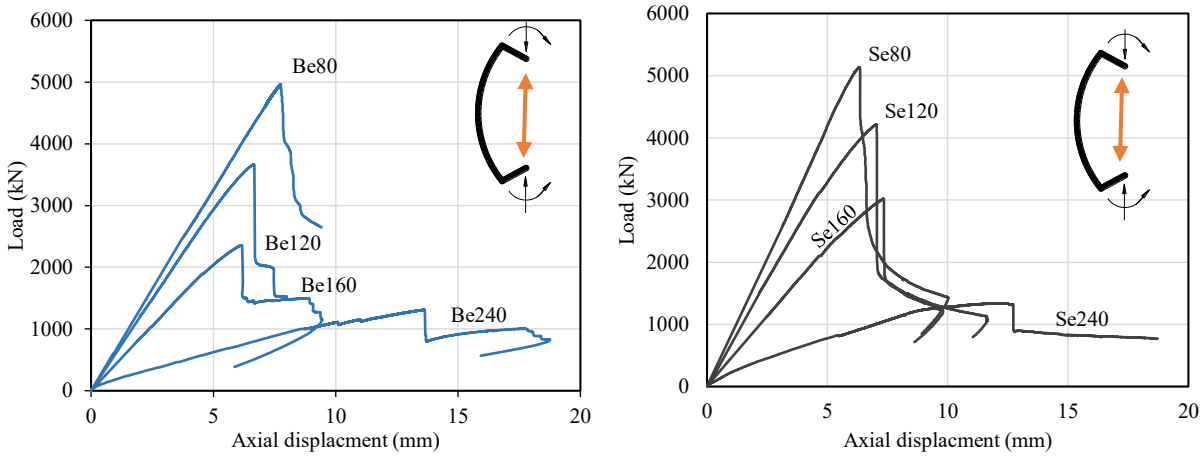

Figure 5-6 – Load versus axial displacement for the BFRP- and steel- reinforced columns.

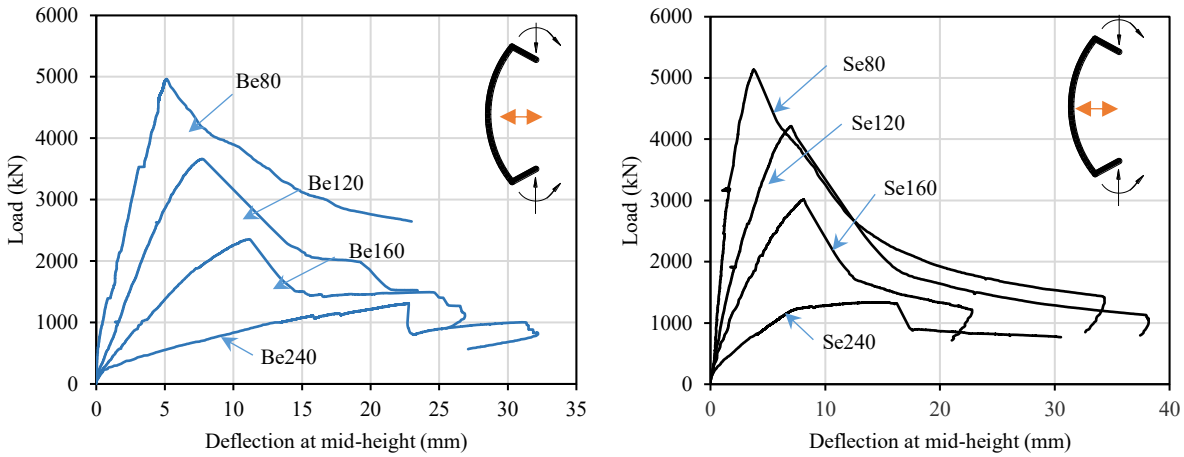

Figure 5-7 – Load versus lateral displacement at mid-height.

In the post-peak phase, the steel-reinforced columns at both eccentricities exhibited slight signs of axial-load resistance, which depended mainly on the concrete compressive resistance. The steel bars negligibly contributed to the post-peak strength as both the compression and tensile bars had reached their yielding strains. The basalt-reinforced columns had less strength loss and lower axial and lateral deformation values in the post-peak phase compared to the control specimens. It is worth mentioning that two different behaviors were observed for e/h = 0.3 and 0.4h. At e = 160 mm (e/h = 0.4) the BFRP-reinforced column's strength reached a plateau with a slight increase in strength, then crushing failure initiated in the compressive bars. The test was terminated when there was no further increase in axial strength. Failure of the BFRP bars was observed only after stopping the test. Overall, both the steel- and BFRP-reinforced columns suffered excessive axial and lateral deformation. The steel-reinforced columns had much wider cracks in the post-peak phase due to bar yielding. The maximum measured compressive strains for the basalt-FRP bars were 6,030 and 4,630 με for e/h = 0.3 and 0.4h, respectively, while the maximum measured tensile strains were 9,860 με for e/h = 0.3 and 10,160 με for e/h = 0.4.

5.6.2. High Eccentricity (e = 240mm).

With both types of reinforcement, applying the axial load at such a high level of eccentricity resulted in greater flexural response of the columns. The cracking stresses were reached at a very early stage of loading. Subsequently, flexural tensile cracks started to appear and widened along the length of the columns, which experienced more axial and lateral deformation as the axial load

increased. On the other hand, higher tensile and compressive strains were reached in the tensile and compressive BFRP bars. In the case of the columns loaded with high eccentricity—Be240 and Se240—the flexural stresses dominated the failure process of the columns' critical section. The steel-reinforced column had a bilinear load–axial gradient up to a maximum axial resistance of 1,338 kN. Its first crack occurred at a load of 300 kN (26% of peak load), then tensile cracks started spreading along the length of the column. At a load of 1,280 kN, the tensile bars reached yield strain and, simultaneously, the cracks grew wider and deeper. Based on the load versus mid-height deflection shown in Fig. 4.6, the specimen exhibited much lower lateral stiffness, which suddenly increased the rate of lateral deflection. This description is consistent with ACI 318-14M's labeling of columns falling within the transition zone, characterized by the yielding of steel bars before peak load is achieved. At this point, the column is classified unsafe due to excessive deflection and wide cracks. That occurred with Se240. The peak resistance was reached when the concrete strain recorded was 3,100 με. At this level of eccentricity, the steel bars buckled outwards which contributed to spalling of the concrete cover.

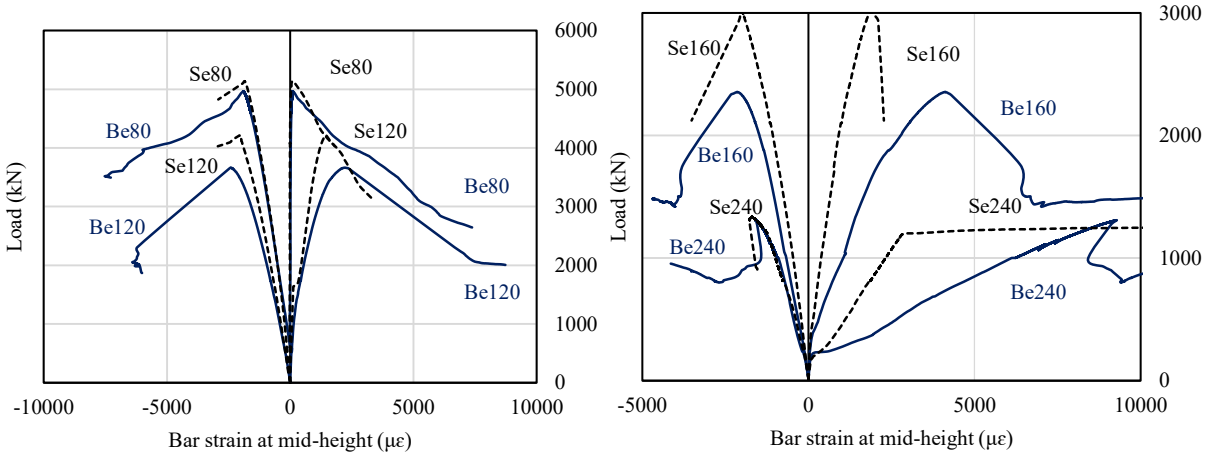

Figure 5-8 – Load versus outermost bar strain at mid-height.

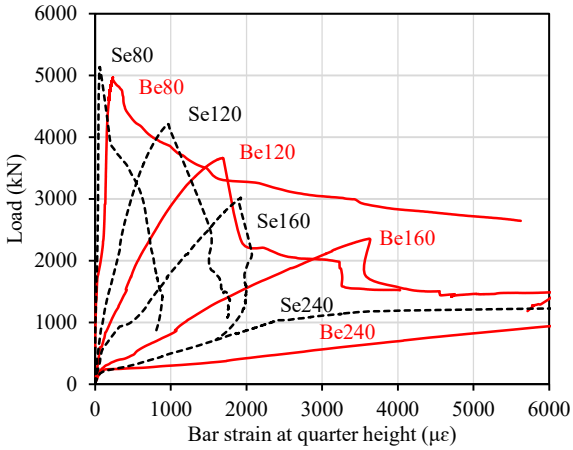

Figure 5-9 – Load versus outermost bar strain at quarter-height.

Column Be240 exhibited a failure process similar to that of its counterpart Se240. For column Be240, the cracking started at the middle top and bottom of the testing zone at a load of 280 kN (22% of peak load). As the load increased, the flexural cracks propagated deeper into the column, and more cracks started to develop along the tensile surface. At such a high *e/h* ratio, the axial load had little effect on reducing the cracks width; the flexural moment controlled the column's failure process. A popping sound was heard at a load of 1,080 kN. This has been attributed to excessive bending due to column's curvature, which caused the basalt bars on the compressive side to reach their ultimate compressive strength, leading to their compression failure. A slight dip in load was noticed before reaching the maximum load, followed by the column resisting more axial load. The column Be240 failed at a load of 1,309 kN. It was noticed that the steel-reinforced counterpart, Se240, had sudden spike in the rate of increase in lateral deflection at a load level of 1,230 kN and lateral deflection of 9.0 mm. This is attributed to the yielding of the tensile bars. Conversely, Be240 did not experience any reduction in lateral stiffness before reaching the peak load. The failure of the column Be240 was marked by spalling of the concrete cover at a concrete strain of 2,770 με. At failure, the column Be240 reached an axial deflection of 13.6 mm and lateral deflection of 22.8 mm. The recorded strain for the compressive bars was 1,910 με (7% of ultimate strain) and 9,300 με (36% of ultimate strain) for the tensile bars. In the post-failure phase, the column, Be240, showed increase in strength, reaching a second peak at a load of 1,000 kN. The maximum recorded strains for the basalt bars were 5,570 με (22% of ultimate strain) for the compressive bars and

10,930 με (42% of ultimate strain) for the tensile bars. The test stopped when the column evidenced no sign of further increase in strength. After load removal, Be240 recovered most of the deflection as the basalt bars did not reach the ultimate rupture or crushing strains. Small residual deformation was still observed due to crushing of the concrete during the failure process.

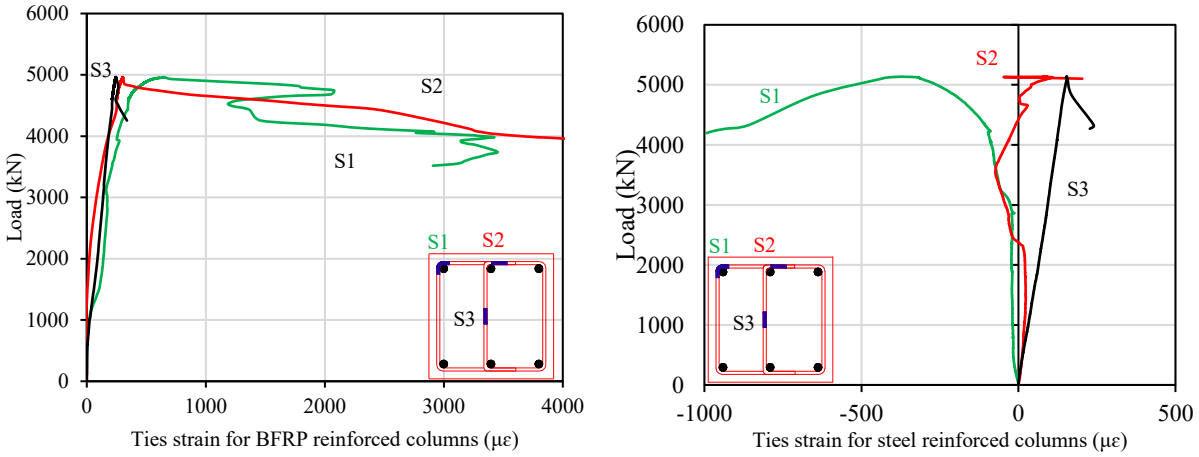

Figure 5-10 – Ties strains for columns tested with *e* = 80 mm.

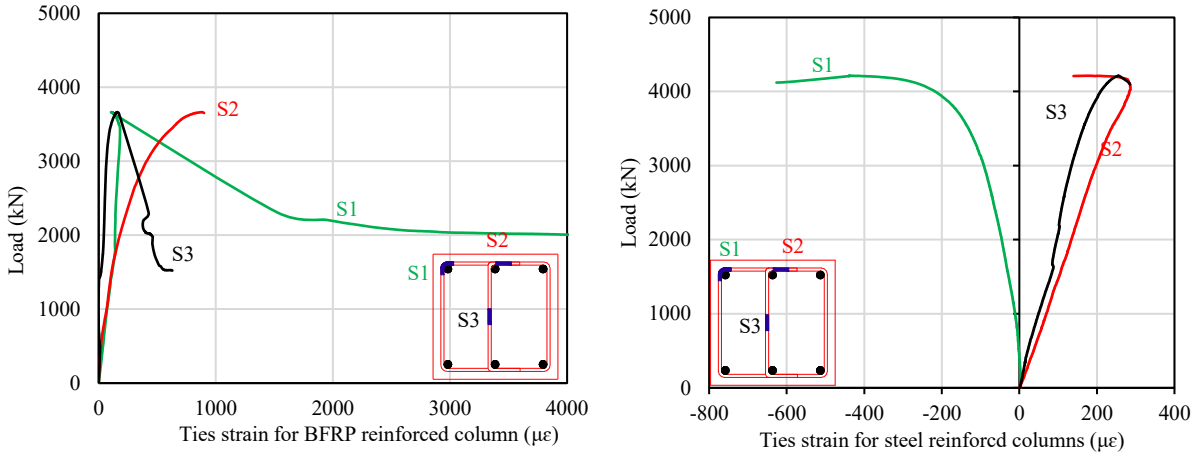

Figure 5-11 – Ties strains for columns tested with *e* = 120 mm.

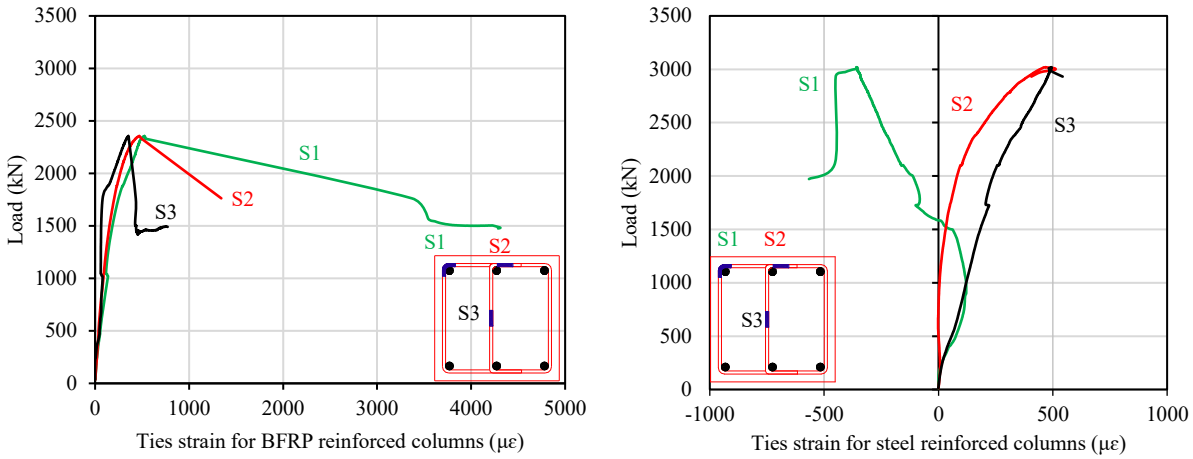

Figure 5-12 – Ties strains for columns tested with *e* = 160 mm.

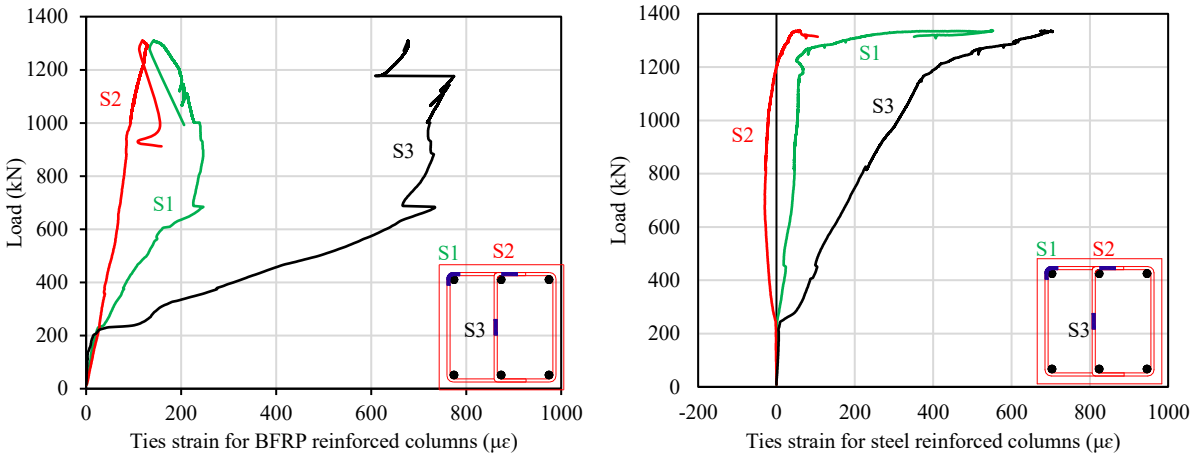

Figure 5-13 – Ties strains for columns tested with *e* = 240 mm.

5.7. DISCUSSION

5.7.1. Effect of Test Parameters

This section discusses the effect of the various study parameters to investigate their effects on the axial–flexural strength, column axial and lateral deflection, and the induced strains in the reinforcement bars and ties.

5.7.2. Initial Eccentricity and Induced Moment

Columns are always subjected to axial and flexural stresses due to the fact that any axial load involves a minimum amount of eccentricity. In practice, axially loaded columns do not exist, therefore a minimum eccentricity is recommended in most design codes. Using HSC allowed the columns to reach higher axial and flexural strength. Consequently, the BFRP bars developed higher tensile strains for all the tested eccentricities, and the columns overall exhibited higher stiffness compared to the columns made with NSC. Using HSC caused the overall failure of the columns to be more brittle, leading to higher strength loss after the maximum axial resistance was reached.

Increasing the level of applied eccentricity reduced the maximum axial load achieved by both the steel- and BFRP-reinforced columns. The BFRP-reinforced columns (Be120, Be160, and Be240) tested at *e/h* of 0.3, 0.4, and 0.6 have an average loss in the strength of 26%, 53%, 74%, respectively, compared to maximum load achieved by Be80. The corresponding strength loss values for the steel-reinforced columns were 18%, 41%, and 56% for columns Se120, Se160, and Se240, respectively, compared to Se80. Moreover, as the eccentricity increased, the columns experienced more lateral deflection and applied moment, which increased the crack depth within the columns. It can be also noticed that the concrete strain readings at the surface ranged from 2,000 to 2,700 με. Increasing the eccentricity would slightly increase the maximum corresponding concrete strain recorded. As for the effect changing eccentricity had on bar strains, the strains were mainly governed by the mode of failure and the deflected shape of the columns. At low eccentricity (0.2*h*), the steel compressive bars reached their yield strains (2300 $\mu\varepsilon$) before reaching the maximum load. The buckling of the steel bars caused the early spalling of the concrete cover, which culminated in the column Se80 reaching its maximum resistance. In the case of column Be80, the failure was governed by concrete crushing, no buckling was observed up until peak load. As the axial load shifted towards the edge, more initial eccentricity was applied to the column. At moderate eccentricity, 0.3 and 0.4*h*, the failure process started as flexural cracks on the tension side of the columns, Be120 and Be160, reducing their axial and lateral stiffness, followed by microcracks on the compressive side of the concrete. The failure mode was marked by concrete crushing on the compression side. The number of tensile cracks increased in number, width, and depth.

Applying the highest eccentricity, (0.6*h),* led the columns to be dominated by flexural stresses. The maximum axial resistance was minimal for all the columns tested. The tensile bars experienced maximum strains during failure. The basalt bars reached a strain of 15,090 με (60% of ultimate strain) at peak load; the steel bars reached yielding strains, which widened the cracks abruptly. The steel-reinforced column's deformed shape can be classified as tensile failure as the steel bars yielded before the concrete reached its maximum strain. Consequently, the column experienced a sudden increase in lateral deformation and much wider cracks. Both the steel- and BFRP-reinforced columns had similar behavior in the pre-peak phase in terms of cracking and large lateral deflection values. No signs of BFRP rupture were observed in the ties or tensile bars.

5.7.3. Efficiency of Using HSC

In order to investigate the effect of increasing the concrete compressive strength, the results for the tested specimens were compared to the previous test results obtained at University of Sherbrooke for normal-strength-concrete columns reinforced with GFRP bars and ties, as tested by Guérin et al. (2018a)**.** Their research involved square specimens of 400 × 400 × 2,000 mm and a concrete strength of 42.3 MPa—tested with eccentricity levels of 40, 80, 160, and 320 mm. Between the two sets of columns made with NSC or HSC, those tested with the same eccentricity were selected for comparison (see Table 5-4). The GFRP and BFRP bars used in these columns had comparable behavior in terms of tensile strength and Young's modulus. For 80 mm eccentricity, the increase in the axial capacity was 48%, and 35% higher for columns Be80 and Se80 (compared to columns CGA80 and CS80), respectively, when the compressive strength increased from 42.3 to 71.2 MPa. The tensile strain at peak load had nearly the same values or less as the applied moment did not initiate enough tensile stresses in the BFRP or steel bars, as the specimen with HSC had higher rupture modulus and column strength. At an eccentricity of 160 mm, the increase in axial strength for columns Be160, and Se160 was 21%, and 30% higher than those achieved by CGA160 and CS160. Also, the tensile strain induced in the tensile bars for column Be160 increased by 43% compared to CGA 160. Applying the same level of eccentricity caused the steel bars on the tension and compression sides of the columns, Se160 and CS160, to reach their yielding strain in both the normal- and high-strength concrete. In terms of lateral deflection, column CGA80 had a deflection of 4.8 mm at a peak load of 3,354 kN, compared to 2.93 mm of lateral deflection at the same load level for Be80. As for the steel-reinforced columns, Se80 (made with HSC) had a lateral deflection

of 2.14 mm, compared to 5.9 mm for CS80 (made with NSC). Using HSC reduced the acquired lateral deflection at a given load level due to the higher Young's modulus compared to NSC. This confirms that HSC columns are less ductile than their NSC counterparts and should have adequate confinement for lateral deformation.

Increasing the concrete strength increased the axial strength of the column cross section as well as the axial and lateral stiffness. It also allows designers to use smaller cross sections to resist a given axial load. Despite these advantages, using HSC decreases the ductility of reinforced members. This is demonstrated by comparing the maximum lateral deflection achieved by the HSC columns compared to those made with NSC.

5.7.4. Reinforcement Type

Steel and BFRP reinforcement have different mechanical properties such as tensile strength, Young's modulus, ultimate strain, and stress–strain behavior. Such differences affect the maximum recorded strains for each type of bar and tie. To account for the different levels of axial stiffness of the reinforced columns in this study—caused by steel and BFRP reinforcement having different Young's moduli—the steel-reinforced columns had ties set at double the spacing used in the BFRP-reinforced columns. This also affected bar-load contribution in compression and the maximum strain induced during loading. In order to verify that, the bar strains were monitored with electric strain gauges mounted at column mid-height on the compressive and tensile bars, and at the quarter height for the tensile bars only (see Fig. 4.9). Given the bar strain, the bar's contribution was calculated by multiplying the strain by the bar's Young's modulus. Table 5-4 shows that the average load carried by the longitudinal BFRP reinforcement was 4.2%, 3.7%, 5.3%, and 8% for Be80, Be120, Be160, and Be240, respectively. The values for the steel-reinforced counterparts were 6.5%, 8.8%, 12%, and 23% for Se80, Se120, Se160, Se240, respectively. The difference in the bar load contribution was expected, since the Young's modulus of the steel bars is more than three times that of the basalt bars. This also accounts for the difference in the axial resistance between the BFRP- and steel-reinforced columns (see Fig. 4.14 (a) and (b)). At similar load levels, the bar load contribution was found to be lower for HSC columns than that for NSC columns. Furthermore, the axial and lateral deflection for columns at the same eccentricity was slightly higher for the BFRP bars.

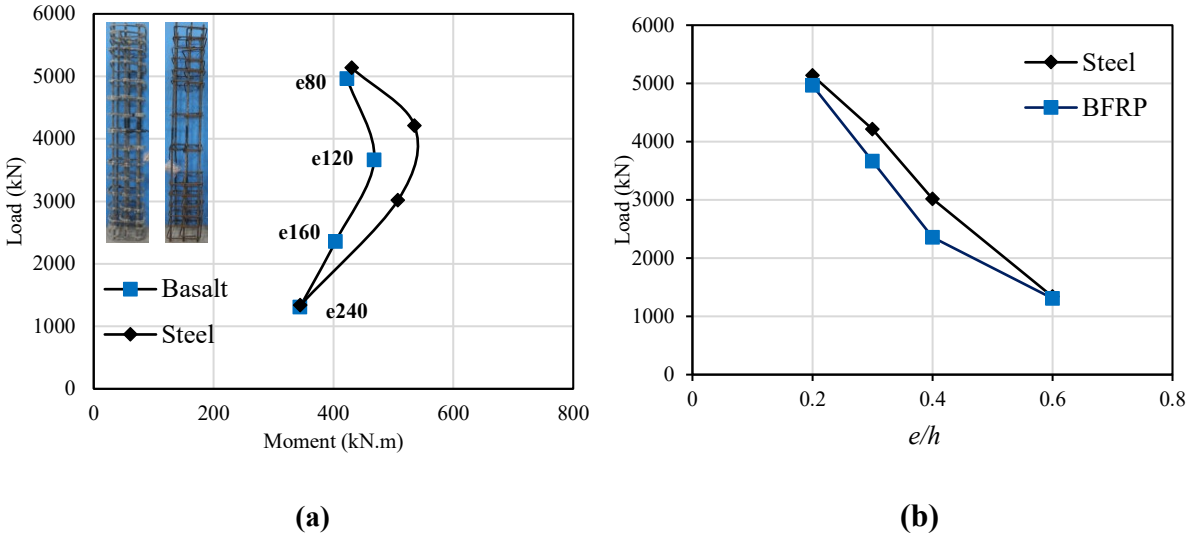

Figure 5-14 – Experimental results for (a) BFRP- and (b) steel-reinforced concrete columns.

As mentioned above, BFRP bars have advantages over other types of fiber in terms of being environmentally friendly, good magnetic-insulation properties, and higher resistance to alkalinity in concrete. In a recent study (El Refai et al., 2015), BFRP showed better adhesion to concrete at the initial stages of loading. The authors also mentioned that, unlike steel, BFRP is elastic and does not have large residual stresses and strains after load removal. This is a preferable in columns and piers for acquiring post-yield stiffness, which also enhances the self-centering capability. Based on the experimental data in our study, the BFRP-reinforced columns exhibited behavior similar to the steel-reinforced columns in terms of crack propagation, axial and lateral deflection, and levels of axial strength. For the post-peak phase, the basalt bars exhibited lower strength losses due to their linear elastic nature. The BFRP bars effectively resisted the tensile forces on the tension side of the columns after concrete crushing and failure of the BFRP bars on the compression side. The basalt ties exhibited no rupturing in either the pre-peak or post-peak phases for the eccentricities tested. Thus, BFRP reinforcement can be used as a valid replacement for steel reinforcement in corrosive environments because of their noncorrodible nature and high tensile strength. FRP bars have high strength-to-weight ratio, high electromagnetic transparency, and relatively high fatigue strength compared to steel reinforcement (ACI 440.1R-15), delivering an acceptable level of strength and deformation, while offering a structurally sound alternative in most applications.

Strain gauges attached at the corner and middle of the ties on the compression side and at the mid-height of the ties (S1, S2, and S3, respectively) recorded similar strains. For all the levels of eccentricity tested, the compression forces resulting from the axial load exerted lateral pressure that was resisted by the ties. In the case of the steel ties, the strains increased significantly after the yield strain was achieved; some strain gauges malfunctioned before reaching this level as a result of excessive tie deformation. The basalt ties returned minor strain readings for S1, S2, and S3 until the maximum load was reached. The strain reading for the basalt ties did not exceed 500 με at peak load. As a result, no rupture was observed in the basalt ties. For the steel-reinforced counterpart, the maximum strain recorded for S2 and S3 was 542 με.

5.8. THEORETICAL ANALYSIS

5.8.1. Experimental and Theoretical Development of the P–M Interaction Diagrams

The shape of the interaction diagram for BFRP-reinforced columns differs from that for steel-reinforced columns due to the two materials behaving differently. The interaction diagram for steel-reinforced columns is divided into three main zones; the compression controlled, transition, and tension-controlled zones (ACI 318R-14M). These zones are determined by both the compression-concrete surface strain and the steel-bar tensile strain. The transition zone of steel reinforcement lies between tensile strains ranging from 0.002 to 0.005. In contrast, the interaction diagram for BFRP-reinforced columns lacks these limits due to the linear elastic behavior of BFRP bars.

In this study, four levels of eccentric loading were applied to two series of columns (series S and B). Based on the test results for each specimen, the P–M interaction diagrams were developed, as shown in Fig. 4.14 (a). The nominal bending moment M_n is given by:

$$M_n = M_{n1} + M_{n2} = P_n \times e \; + \; P_n \times x \tag{4.1}$$

where P_n is the nominal axial force; e is the given eccentricity, and x is the lateral displacement at peak load measured at the column's mid-height. Figure 4.15 also shows the strain-distribution assumptions used for BFRP-reinforced HSC columns.

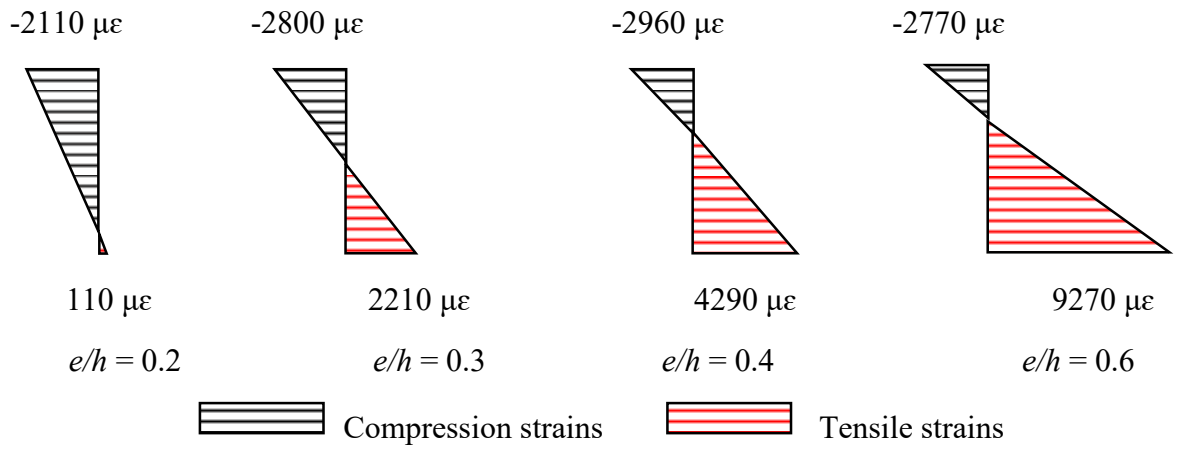

Figure 5-15 – Strain profile for the BFRP-reinforced columns at peak load for the tested eccentricities.

5.8.2. Theoretical Prediction of P-M Interaction Diagrams

An analytical study was performed to draw a full P–M interaction diagram, taking into account the design provisions in ACI 440.1R-15 and CSA S806-12, for comparison with the experimental results for the tested columns. The codes only provide for the use of GFRP bars in compression members. These limits were used for BFRP bars as there are no current specifications specifically for BFRP reinforcement. ACI 440.1R-15 recommends to refrain from relying on FRP bars to resist compressive forces because they have a lower modulus than steel. CSA S806-12, on the other hand, allows the use of FRP bars in compression members but does not consider them for compressive strength. Other researchers recommended substituting concrete for the FRP bars (Zadeh and Nanni, 2013). Their study considered a strip-by-strip approach and force equilibrium to develop the interaction diagram for BFRP-reinforced columns. In applying this approach, the cross section was divided into ten strips of equal thickness. Increasing the number of layers would not significantly change the accuracy of the strength prediction. The layer thickness was equal to the depth of the square cross section divided by the number of strips. The maximum strain of 0.0035 is assumed to be reached at the outermost strip. Based on the test results, the strain distribution in all the specimens was almost linear up to the column's maximum resistance. This proves that assuming that the plane section remains plane after deformation is a valid and true assumption. By taking

that into consideration, the average strain for the rest of the strips is determined and the stress determined for each section. The concrete model used for HSC is explained below. Figure 4.16 shows the stress and strain assumptions and symbols for the strip-method analysis. The tensile stresses for strips below the neutral axis were ignored. After that, the total forces for the strips in compression were added together. Then the strain corresponding to the level of the tensile and compression reinforcement was calculated to account for their forces. Doing that allowed for determining the nominal axial force (P_n) and the nominal moment (M_n).

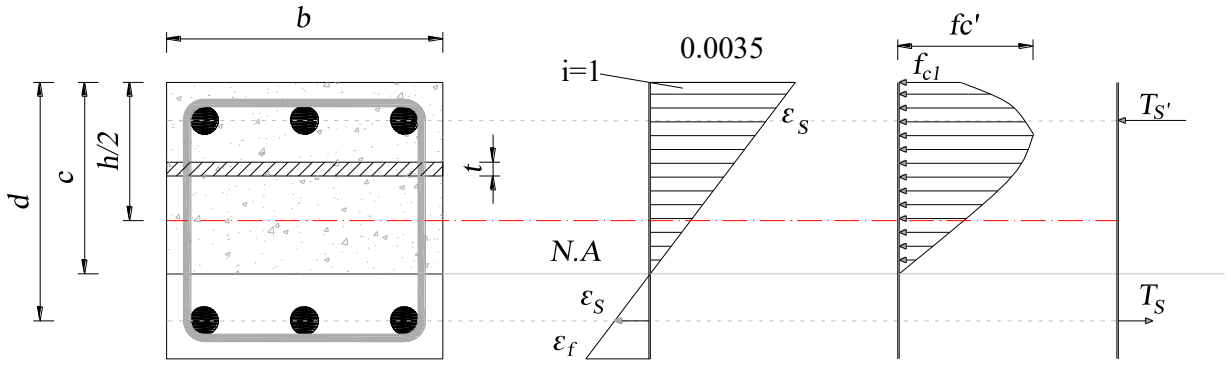

Figure 5-16 – Stress and strain assumption for strip-by-strip method of analysis.

For a comprehensive analysis, the nominal axial and bending resistances were calculated with two different assumptions: (1) considering the full contribution of the BFRP compression bars, and (2) ignoring the contribution of the compression bars. According to the design codes, the maximum strain taken for BFRP bars is the same as the maximum strain for concrete (3,000 με for ACI 440.1R-15 and 3,500 με for, CSA S6-14, CSA A23.3-14 and S806-12). Based on the following assumptions, the theoretical interaction diagram was drawn.

1) The bond between the BFRP bars and concrete is perfect, which means that the BFRP bars and the concrete have the same strains.

2) The strength factor for the BFRP bars and concrete is set to unity.

3) The maximum strain is 3,500 as per CSA S806-12; the concrete tensile strength is ignored.

4) The nominal axial resistance is calculated based on the following equation (assuming that the strain in the BFRP bars is equal to the ultimate assumed concrete strain).

$$P_o = P_c + P_f = \alpha_1 f_c^{'}(A_g - A_f) + 0.0035 E_f A_f \tag{4.2}$$

Unconfined High-Strength-Concrete Stress–Strain Model

HSC and NSC have different strain responses. In 1973, Popvics proposed a convenient expression for the ascending part of the stress–strain curve:

$$f_c = f_c^{'} \frac{\varepsilon_c}{\varepsilon_c^{'}} \frac{n}{n - 1 + (\varepsilon_c / \varepsilon_c^{'})^n} \tag{4.3}$$

and Thorenfeldt et al. (1987) suggested adding the factor k to accurately predict the descending part as follows:

$$f_c = f_c^{'} \frac{\varepsilon_c}{\varepsilon_c^{'}} \frac{n}{n - 1 + (\varepsilon_c / \varepsilon_c^{'})^{nk}}, \tag{4.4}$$

$$n = 0.8 + \frac{f_c^{'}}{17} \text{ (MPa)}, \tag{4.5}$$

$$k = 0.67 + \frac{f_c^{'}}{62} \text{(MPa)}, \tag{4.6}$$

$$\varepsilon_c^{'} = \frac{f_c^{'}}{E_c} \frac{n}{n - 1}. \tag{4.7}$$

where ε_c is the axial concrete strain at any concrete stress; $f_c^{'}$ is the unconfined concrete maximum stress at 28 days; $\varepsilon_c^{'}$ is the strain when f_c reaches the maximum stress $f_c^{'}$; n is a curve-fitting factor responsible for the ascending slope; k is the factor for the descending branch's slope; and E_c is the elastic modulus of concrete (ACI 318-14M).

The following section presents the nominal interaction diagram for the axial and bending moment based on two different scenarios. In these two scenarios, the contribution of the compression reinforcement is ignored in one and considered in the other.

Scenario A: Ignoring the Contribution of BFRP Bars in Compression.

In this scenario, the nominal axial load and flexural resistance can be calculated as:

$$P_n = P_c - T_f = \sum_{n1}^{nt} tbf_i - \varepsilon_{fj} E_f A_f \ , \tag{4.8}$$

$$M_n = M_c \pm M_t = \sum_{n=1}^{nt} f_i \left(\frac{h}{2} - (n - \frac{t}{2})t\right) \pm \varepsilon_{fj} E_f A_f \tag{4.9}$$

where t is the thickness of the strips, b is the depth of the square cross section; ε_{fj}, E_f, and A_f are the strain in the tensile bars, Young's modulus, and the reinforcement area, respectively.

Scenario B: Considering the Contribution of BFRP Reinforcement in Compression

The above equations are modified to account for the compression reinforcement by adding their compression forces. In this scenario, the Young's modulus for the compression forces is assumed to be equal to the tensile Young's modulus.

5.8.3. Comparing the Experimental and Theoretical Results

Figure 4.17 compares the experimental results for B and S columns to the theoretical-model calculation by plotting the P–M interaction diagram for the same cross section using the scenarios above. Scenario B, in which the contribution of the BFRP bars in compression was fully considered, had values closer to the experimental results than was scenario A. Scenario B had axial and flexural predictions within 1% to 10% of the to the experimental results. Scenario A, however, which ignored the contribution of the compression reinforcement, was within 3% to 16% of the experimental results. Based on these results, it can be concluded that the experimental results are in better agreement with the predicted results when the contribution of the compression bars are considered. Ignoring their contribution may, however, be considered as a more conservative method providing a safe margin for designers.

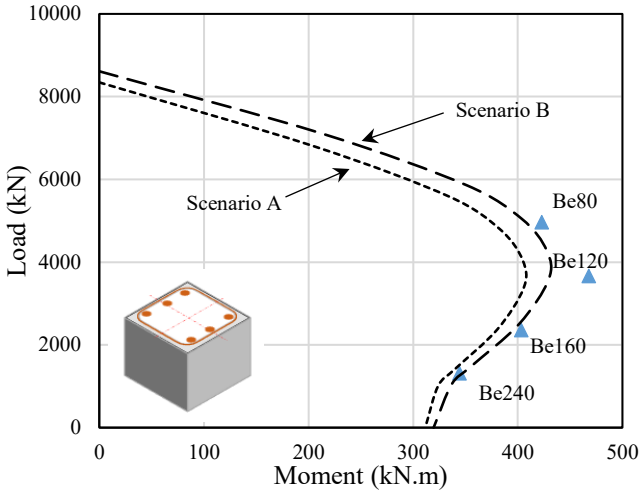

Figure 5-17 – Axial-moment interaction diagram for experimental vs predicted results.

5.8.4. Parametric Investigation

This section presents the effect of the concrete strength and reinforcement ratio as well as the contribution of the compression reinforcement (see Fig. 4.18). A sectional analysis was applied to square columns with the same cross section as the specimens tested (400 × 400 mm). Concrete strengths of 40, 60, 80, and 100 MPa were used with BFRP-reinforcement ratios ranging from 1% to 4%.

5.8.4.1. Effect of Increasing the Longitudinal-Reinforcement Ratio

The influence of changing the column's reinforcement ratio differed depending on the level of eccentricity and the contribution of the compression reinforcement (Scenarios A and B; see Fig. 4.18). In Scenario B yielded a more pronounced reinforcement effect throughout the interaction diagram, especially for low eccentricities at which most of the column's cross section was under compression. Ignoring the contribution of the compression reinforcement, Scenario A concealed any difference in values for the upper part of the interaction diagram. The upper part represents low eccentricities ($e < h/6$), where most of the cross-sectional area is under compressive stresses. In fact, by increasing the reinforcement ratio of the cross section, a larger area is subtracted from the concrete, which reduces the resultant compressive forces of the concrete.

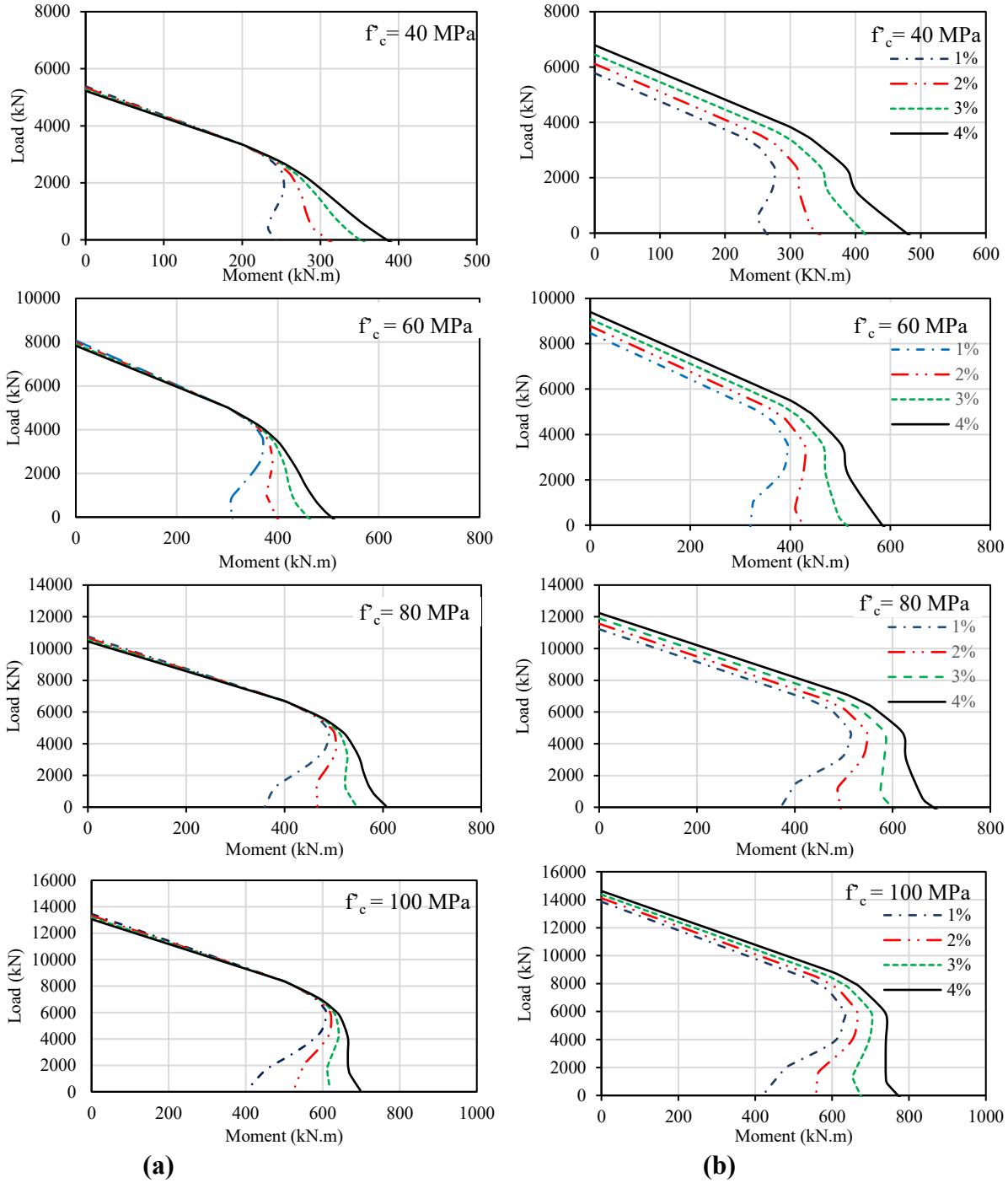

Figure 5-18 – Theoretical interaction diagram for a square section (400×400 mm) (a) ignoring the contribution of the BFRP bars in compression and (b) considering the contribution of the BFRP bars in compression.

As for high eccentricities, the difference in values for Scenario A gradually increased until the flexural strength of the cross section was reached, which represents the beam case. In contrast,

using Scenario B increased the capacity of the cross section compared to Scenario A. The difference in values between each reinforcement ratio calculated using scenario B was nearly the same throughout the lower part.

5.8.4.2. Effect of the Concrete Strength

The impact of changing the concrete strength is obvious in all the diagrams in Fig. 18. Increasing the concrete strength provided more axial resistance to the uncracked concrete. Moreover, the flexural capacity was increased by using higher-strength concrete due to the nature of BFRP reinforcement, which can sustain higher tensile strains than steel reinforcement. It should be noted that higher concrete strength reduces the contribution of the compression reinforcement. This narrows the difference in values between Scenarios A and B.

5.8.4.3. Effect of Ignoring the Contribution of Bars in Compression

The current codes and design guidelines (CSA S806-12 and ACI 440.1R-15) recommend ignoring the contribution of FRP reinforcement in compression. As Figures 4.17 and 4.18 show, ignoring the contribution of the compressive bars produced a minor change in the axial capacity of the columns under axial load or low eccentricity. This assumption might be valid for structural members under axial loads or columns with low eccentric values. In the case of columns subjected to axial loads with high eccentricity or flexural moments, the contribution of the compression reinforcement could improve the predictions. Designers can choose to ignore this contribution for a larger margin of safety.

Using HSC will provide greater compressive strength to resist external forces. The contribution of the compressive BFRP bars compared to the HSC compressive strength was relatively low due to the fact that the maximum strain reached by the BFRP bars was the same as the maximum strain of the concrete. This gap in strength increased with concrete with higher compressive strength. The assumption made by Choo et al. (2006) is sound: when performing analysis and design, ignore the contribution of FRP bars when using HSC. Another good assumption that can predict more accurate results comes from Zadeh and Nanni (2013), which replaces FRP bars in compression with an equivalent area of concrete while considering the full contribution of the bars in tension. Overall, the evidence of the relatively small compression contribution of the BFRP bars

underscores that it can be ignored in analysis. BFRP bars add slight strength; it is not overly conservative to ignore their contribution, but it is certainly a simple, conservative approach.

5.9. MOMENT–CURVATURE BEHAVIOR

When reinforced-concrete members are subjected to combined axial and bending forces, the location of the neutral axis in a cross section is different than the center of gravity. Applying axial compression loads in addition to the flexural stresses affects the cracking load and the curvature induced within the columns. As can be seen in Fig. 4.19, increasing the axial load led to a decrease in the cracking load and flexural stiffness of the member (EI_{sec}) which is represented by the slope of the curve. The curvature of the columns was calculated with Eq. 4.10. Calculating the curvature of the column after reaching the peak-load wasn't possible as some of the strain gauges were damaged due to the spalling of the concrete cover on the compression side. The results revealed the curvature at peak ranged from 0.002/d to 0.01/d for the BFRP-reinforced columns. Figure 4.19 shows the moment–curvature response for all the series tested in this study.

$$\psi = \frac{\varepsilon_t - \varepsilon_c}{d} \tag{4.10}$$

$$EI_{\text{sec}} = \frac{M}{\psi} \tag{4.11}$$

where ψ is the curvature, ε_t is the tensile strain, ε_c compressive strain, and d the depth between the centroids of the outermost bars on the compression and tension sides.

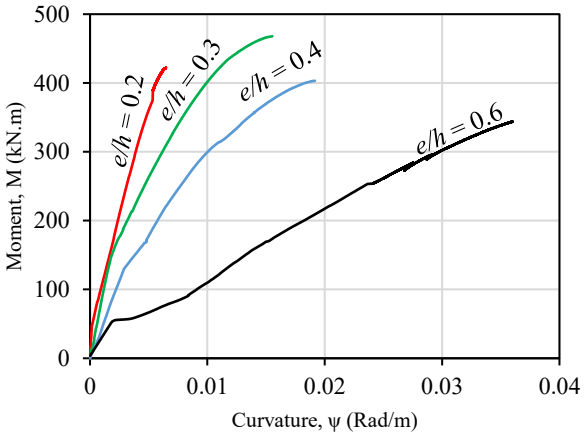

Figure 5-19 – Moment curvature for all BFRP-reinforced concrete columns at four different eccentricities.

5.10. Ductility

Acquiring higher strength by using HSC has a drawback of reducing the ductility of the structural members. Based on the energy definition, Naaman and Jeong (1995) stated that ductility can be defined as the ratio between the total energy to the elastic energy. The absorbed-energy approach was used to measure the ductility of the steel- and BFRP-reinforced columns. The calculation requires the combined strain ζ, which is the combined strain for the average strain ε_{av} at the geometric center multiplied by the curvature ψ.

$$\zeta = \varepsilon_{av} + (e + \Delta)\Psi \tag{4.12}$$

The ductility index is described as follows:

$$\mu_e = \frac{1}{2}\left(\frac{E_{tot}}{E_{el}} + 1\right) \tag{4.13}$$

where E_{tot} is the total energy computed as the area under the load–deflection curve, and E_{el} is the elastic energy released upon failure, computed as the area of the triangle formed at the failure load by the line having the weighted average slope of the two initial straight lines of the load–deflection curve. Table 5-4 provides the computed ductility indexes for the BFRP- and steel-reinforced specimens. The ductility index was nearly the same for the all the tested eccentricities as the failure was governed by yielding of the steel reinforcement. The ductility index for the BFRP-reinforced

columns changed, however, from 1.16 to 1.30 as the maximum developed strain in the tensile bars increased with the change in eccentricity without reaching the failure limit.

5.11. Effective Flexural Stiffness (EI_{sec})

The section stiffness (EI_{sec}) was determined for the BFRP-reinforced specimens to study the effect of changing the applied eccentricity and the magnitude of the axial force. Figure 4.20 shows the relationship between EI_{sec}/EI_g and P/P_o for the BFRP-reinforced columns. EI_{sec} was calculated by dividing the moment by the curvature at every load step, as shown in Equation 4.11. At an early stage of loading, the column cross section exhibited no cracking until the cracking load was reached. Increasing the applied eccentricity decreased the maximum acquired section stiffness (EI_{sec}) throughout the loading phase. As expected, the columns with the lowest applied eccentricity had the smallest loss in section stiffness, as the column had fewer cracks. In contrast, more cracks appeared when the column was subjected to the highest eccentricity, causing the column cross section to gradually lose its stiffness. It should be noted that, at e/h = 0.6, the stiffness reached a nearly horizontal plateau, indicating that no more cracks were formed, and more tensile strains were induced in the BFRP bars. This behavior can indicate that the column-failure process at this level of eccentricity was similar to the tensile failure of steel-reinforced columns, as the column experienced wide cracks and large values of lateral deformation before reaching the peak load.

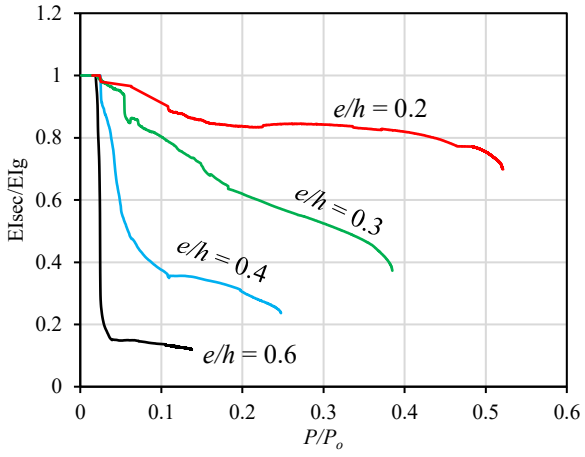

Figure 5-20 – Influence of P/P0 and e/h on the section stiffness (EI_{sec}/EI_g) for the tested BFRP-reinforced concrete columns.

5.12. Comparative Study on Different Estimations of Section Flexural Stiffness

Figure 4.21 shows the effective section stiffness at service and ultimate loads at the four applied levels of eccentricity (e = 0.2h, 0.3h, 0.4h, and 0.6h). In order to plot this relationship, the flexural stiffness was plotted at service-load and ultimate-load levels at the tested eccentricities. The ϕ factor was set to 0.65 and 0.55 for compression- and tension-controlled sections, respectively. The ultimate load was defined as 0.48P_n. The service load was taken as 0.70 of the ultimate load, as recommended in ACI 318-14M. The pattern can be described by a second-degree parabolic equation: $y = 2.6x^2 - 3.7x + 1.4$. The experimental results were then compared to equations proposed by Zadeh and Nanni (2017) and Hadhood et al. (2018) to assess the applicability of these equations when HSC is used, which is described as follows:

$$(I_e / I_g)_{col} = 0.40 + 0.15\frac{E_f}{E_s}, \text{ where } (I_e / I_g)_{col} \le 0.55 \text{ (Zadeh and Nanni, 2017)} \tag{4.14}$$

$$(I_e / I_g)_{beam} = 0.10 + 0.25\frac{E_f}{E_s}, \text{ where } (I_e / I_g)_{beam} \le 0.35 \text{ (Zadeh and Nanni, 2017)} \tag{4.15}$$

$$(I_e / I_g)_{col} = \left(0.5 + 25\rho_f \frac{E_f}{E_s}\right)\left(1 - \frac{e}{h}\right) \text{ (Hadhood et al., 2018)} \tag{4.16}$$

$$(I_e / I_g)_{beam} = \left(0.15 + 25\rho_{f-ten} \frac{E_f}{E_s}\right) \text{ (Hadhood et al., 2018)} \tag{4.17}$$

$$\frac{EI(x)}{E_c I_g} = \left(3 - 2\frac{x}{h}\right)\left(\frac{x}{h}\right)^2 + 3\gamma^2 n_s \rho_{st} \tag{4.18}$$

$$\frac{e(x)}{h} = \frac{EI(x)/E_c I_g}{6\left[\left(\frac{x}{h}\right)^2 - \left(\frac{\gamma+1}{2} - \frac{x}{h}\right)n_f \rho_f\right]} \tag{4.19}$$

where ρ_f is the FRP-reinforcement ratio; ρ_{f-t} is the FRP-reinforcement ratio in tension; ρ_{st} is the steel-reinforcement ratio; E_f is the FRP-bar Young's modulus; E_c is the concrete's Young's

modulus; n_s is the steel-bar modular ratio; n_f is the FRP-bar modular ratio; EI_{sec} is the section stiffness; I_g is the gross moment of inertia; I_e is the effective moment of inertia; and γ is the ratio of the distance between the compressive and tensile reinforcement and section height.

The equations proposed by Zadeh and Nanni were developed to determine the relative stiffness of rectangular FRP-reinforced concrete members (Eqns. 4.14 and 4.15). Equation 4.14 can be applied to columns with applied eccentricity-to-depth ratios of $0.25 \leq e/h \leq 0.50$. Equation 4.15 applies to columns with eccentricity-to-depth ratios exceeding 0.50, for which the resultant axial force is actually located outside the section, and the column acts more as a flexural member, since the axial force to applied moment is considered low. In addition, the theoretical mathematical expressions (Eqns. 4.18 and 4.19), proposed by Zadeh and Nanni (2017) were plotted against the experimental results to verify their accuracy. The derived mathematical model was used to measure the effective flexural stiffness at any applied eccentricity at the service-load level. Moreover, Eqns. 4.16 and 4.17 were proposed by Hadhood et al. (2018) to estimate the effective flexural stiffness of column cross sections reinforced with GFRP bars. The authors of these equations took into consideration the effect of changing the initial eccentricity on the corresponding flexural stiffness of the concrete cross section. As can be seen in Fig. 4.20, the equations proposed by Zadeh and Nanni (2017) gave a constant value for section stiffness as the equation doesn't take into account the change in applied eccentricity. Equation 4.14 had a mean ratio of 1.1 and 0.86 for column specimens with $0.25 \leq e/h \leq 0.50$ at the service-load and ultimate-load levels, respectively. For the beam specimens, Zadeh and Nanni's equation (Eq. 4.15) had a mean ratio of 1.68 and 0.92 for the service-load and ultimate-load levels, respectively. The theoretical model (Eq. 4.19) had a mean difference value of 0.83 at ultimate load. The model accurately predicted the section stiffness with a small mean difference of 1.1 at the service-load phase. The theoretical model accurately predicted the section stiffness at the service-load level as the derivation of the equation was based on the stress and strain induced in the column cross section at the service-load level. The equation proposed by Hadhood et al. (2018) yielded more accurate results compared to the values provided by Zadeh and Nanni's equation, as the effect of changing the applied eccentricity was taken into consideration. At the service-load level, Eq. 4.14 had a mean ratio of 0.95 for the column specimens, while Eq. 4.17 was 1.82 for beam specimens. At the ultimate-load level, the equation gave a mean ratio of 0.75 for column specimens and 1.29 for beam specimens. The overall prediction for each method was evaluated using regression analysis with an R^2 value for each method. The theoretical model (Eq. 4.19) had

an R^2 value of 0.986 and 0.994 at the service-load and ultimate-load levels, respectively. Zadeh and Nanni's equations (Eqns. 4.14 and 4.15) had an R^2 value of 0.64 and 0.56 for the service-load and ultimate-load levels, respectively, compared to 0.94 and 0.89 for the Hadhood et al. (2018) equations (Eqns. 4.16 and 4.17).

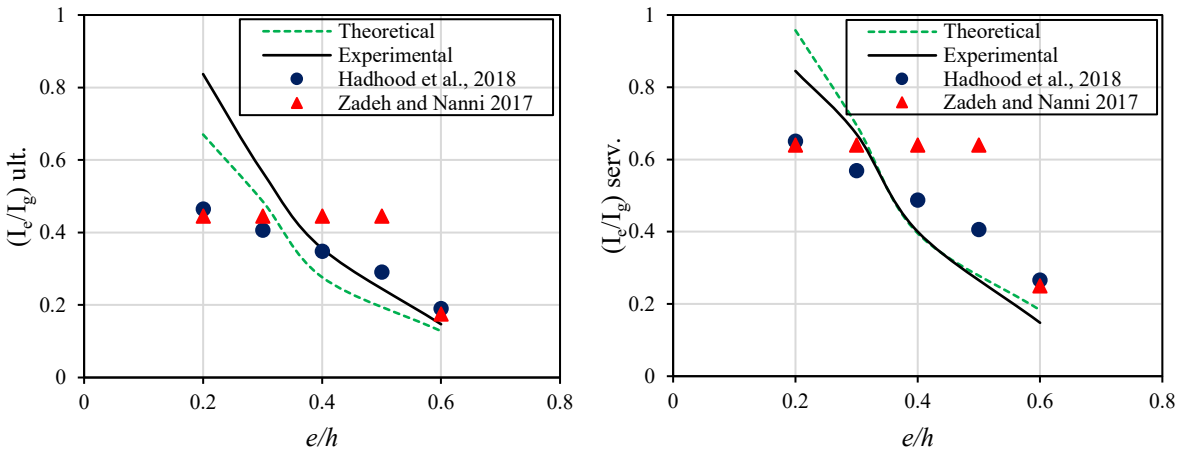

(a) (b)

Figure 5-21 – Comparing relative flexural stiffness of BFRP-reinforced concrete members using theoretical equations and experimental data (a) at the ultimate- and (b) service-load levels.

5.13. Hybrid Columns

Another interesting application is using hybrid reinforcement for HSC columns. Steel bars can be used as longitudinal bars for their axial contribution and BFRP ties serve as transverse reinforcement. Pantelides et al. (2013) found that longitudinal steel bars confined with GFRP spirals in concrete columns were not affected by corrosion. The hybrid columns in that study achieved 84% of the axial-load capacity of the concrete columns totally reinforced with steel. Hales et al. (2016) also conducted a research program for short columns made with HSC. The columns had 13 mm steel bars as longitudinal reinforcement and GFRP spirals 10 mm in diameter. The column height was 760 mm with a circular cross section of 305 mm and reinforcement ratio of 1%. The study indicated that using HSC is a viable approach with hybrid columns as long as the GFRP transverse reinforcement is used with a smaller pitch and larger cross section. Using longitudinal

steels bars with different types of FRP ties or spirals as transverse reinforcement offers the advantages of larger deflection capacity, ductility, and better corrosion resistance. The design equations in ACI 318-14M can be used to design the cross section of hybrid columns longitudinally reinforced with steel bars. Recent research included recommendations for spacing of FRP ties in hybrid columns (Fakharifar et al. 2016, and Kamakshi and Vinu 2018). More research is, however, needed to determine a recommendation for tie or spiral spacing.

5.14. CONCLUSIONS

This paper presented tests performed to investigate the axial–flexural behavior of full-scale HSC columns. Newly developed sand-coated basalt-FRP bars and ties were used. The columns were prepared to study the effect of three test parameters: eccentricity-to-depth ratio, FRP reinforcement type (basalt versus steel), and concrete strength. Theoretical analysis was conducted to develop the P–M interaction diagrams and moment–curvature behavior, and to estimate the flexural stiffness. Based on the experimental test results and analysis presented in this paper, the following conclusions can be drawn:

1- Using BFRP reinforcement in HSC columns yielded axial resistance close to that of steel-reinforced columns at eccentricity-to-depth ratios of 0.2h and 0.6h. The difference in strength did not exceed 3%, this is attributed to the yielding of the steel bars in the steel reinforced columns at these eccentricities. While, the compressive strength for BFRP-reinforced columns reinforced were 13% and 22% lower than the steel-reinforced counterparts at 0.3h and 0.4h, respectively.

2- As expected, using HSC allowed the columns to develop higher axial and flexural strengths compared using NSC. Moreover, increased eccentricity and the use of HSC enabled the tensile bars to develop higher tensile strains, which made them more effective.

3- Both types of reinforcement were able to achieve stable and ductile behavior in the pre-peak phase. The BFRP bars developed up to 4,000 με compressive strain, confirming that the BFRP bars were effective in resisting compression until concrete cover crushing.

4- The BFRP- and steel-reinforced HSC columns tested under low eccentricity (0.2*h*) failed in compression. Compression–ductile failure was the dominant failure mode of the BFRP- and steel-reinforced concrete specimens tested with an eccentricity of 0.3 and 0.4*h*. Due to the excessive

deflection, cracking, and large recorded strains in the BFRP bars in the columns tested under high eccentricity (0.6*h*, the failure could be called tension controlled.

5- Using tie spacing of $8d_b$ (half of that specified in ACI 318-14 to account for the difference in moduli of elasticity between the steel and BFRP reinforcement) for the BFRP-reinforced HSC columns provided sufficient lateral support to prevent crushing of the BFRP bars and the concrete core. Also, the concrete core was able to continue withstanding the applied load in the post-peak phase, and the BFRP bars developed maximum compressive strains and tensile strains of 6,700 με 10,900 με.

6- The interaction diagram for the BFRP-reinforced HSC columns tested shows the characteristic "knee" shape found with conventional steel-reinforced concrete columns. The failure envelope of the steel-reinforced concrete specimens was slightly larger than those of the BFRP-reinforced HSC columns.

7- Using a strip-by-strip approach predicted axial- and flexural-strength values close to the experimental results. Considering the contribution of the BFRP reinforcement in compression resulted in more reliable predictions, while it is advised to replace the BFRP with concrete when the BFRP contribution is ignored.

8- The parametric study indicates that increasing the concrete strength from 40 to 100 MPa significantly increased the failure envelopes in both scenarios (neglecting or considering the BFRP's compression contribution).

9- Using the equations proposed by Hadhood et al. (2018) provided more accurate predictions of the effective cross-section stiffness ($R^2 = 0.94$) compared to the Zadeh and Nanni (2017) equations ($R^2 = 0.64$) for both the ultimate- and service-load levels.

10- The experimental evidence from this study provides some experimental data for including design provisions that allows for the design and use of FRP reinforcement in non-prestressed compression elements in a future edition of the *AASHTO LRFD Bridge Design Specifications* and *Canadian Highway Bridge Design Code* for the use of BFRP bars and ties in reinforced-concrete members for bridge pier and pile applications.

CHAPTER 6 EFFECT OF GFRP-REINFORCEMENT RATIO ON THE STRENGTH AND EFFECTIVE STIFFNESS OF HIGH-STRENGTH CONCRETE COLUMNS: EXPERIMENTAL AND ANALYTICAL STUDY

Foreword

Authors and Affiliation:

- Ashraf Salah-Eldin: Ph.D. candidate, Department of Civil Engineering, Université de Sherbrooke, Sherbrooke, Quebec, Canada, J1K 2R1.
- Hamdy M. Mohamed: Research Associate/Lecturer, Department of Civil Engineering, Université de Sherbrooke, Sherbrooke, Quebec, Canada, J1K 2R1.
- Brahim Benmokrane: Professor, Department of Civil Engineering, Université de Sherbrooke, Sherbrooke, Quebec, Canada, J1K 2R1.

Journal Title: (Journal of Structural Engineering, ASCE)

6.1. Abstract

Fiber-reinforced-polymer (FRP) bars are considered as alternative to steel bars to avoid corrosion problems and ensure that structures lave long service lives. Using high-strength concrete (HSC) with glass-fiber-reinforced polymer (GFRP) as internal reinforcement can allow designers to reduce member size and increase the structure's life span. Given HSC's brittle nature, its use—especially in columns—should be investigated to prevent undesirable brittle failure. This is of particular concern if GFRP reinforcement is used. This paper reports the axial–flexural test results

for 12 HSC columns reinforced with GFRP to evaluate the implication of using HSC. The parameters were the influence of the longitudinal GFRP-reinforcement ratio and concrete compressive strength on the load-carrying capacity, deflection, ductility, strains in the concrete and reinforcement, failure modes, and flexural stiffness. All the columns failed in a compression failure mode due to concrete crushing. The GFRP bars developed higher tensile strains in the HSC due to the axial–flexural load. compared to columns made with normal-strength concrete (NSC). A minimum reinforcement ratio of 1% in the case of HSC proved practical. Increasing the reinforcement ratio to 2.5% improved in post-peak behavior and yielded a second peak for specimens tested at eccentricities corresponding to 30%, 40%, and 60% of the cross-sectional depth. This study integrated the results of experimentally tested specimens into a developed analytical model to establish moment–curvature and effective-stiffness relationships. The results were also evaluated for the tested specimens and compared to the theoretical expressions used for NSC.

Keywords: Compression members, columns, concrete, eccentric loading, high-strength concrete, glass-FRP (GFRP) reinforcement, axial load, flexural capacity, interaction diagram, sectional analysis, stiffness.

6.2. INTRODUCTION

The use of high-strength concrete (HSC) in building and bridge construction has increased over the last two decades. HSC delivers higher strength and improved performance than normal-strength concrete (NSC). It also gives reinforced-concrete (RC) members more durability and longer life spans than NSC. For these reasons, HSC has been used in columns for heavy structures such as bridges, low- and mid-rise buildings, and foundation piles. The strength acquired with using HSC in structural members comes at a cost: more brittle behavior at failure and lower ductility. In addition, corrosion is an issue when steel reinforcement is used. On the other hand, fiber-

reinforced-polymer (FRP) reinforcement is recommended for use in aggressive environments and to avoid corrosion problems. The advantages of FRP bars over conventional steel bars include noncorroding behavior, high longitudinal tensile strength in the direction of the fibers, nonmagnetic nature, and light weight.

Recent studies have investigated the use of FRP bars as reinforcement for columns loaded axially and eccentrically (Tobbi et al. 2012, Hadhood et al., Guérin et al. 2018a, b, Pantelides et al. 2013). Guérin et al. (2018a) reported that GFRP-reinforced columns tested under eccentric loads failed in compression failure mode. For columns tested under eccentricities higher than 40% of the member depth, the failure was described as tension-controlled due to the excessive deflection, cracking, and large recorded strains in the GFRP bars. Guérin et al. (2018b) also investigated what impact changing the reinforcement ratio would have on the overall behavior of the columns. They noted that changing the reinforcement ratio was ineffective for columns tested at small eccentricities, although the strength increase was greater under high levels of eccentricity. In addition, they introduced strain limits to aid in classifying the failure behavior of columns under different levels of eccentricity. De Luca et al. (2010) found that the GFRP reinforcing bars did not contribute significantly to column axial-load capacity. Given that, they recommended using a minimum reinforcement ratio of 1.0% of the gross sectional area, as also specified in the ACI building code for steel-reinforced columns. Zadeh and Nanni (2013) also recommended using this reinforcement ratio.

Limited research has, however, involved full-scale HSC columns with GFRP reinforcement. Hadhood et al. (2017a) tested 10 circular HSC columns under different eccentricity-to-diameter ratios. They found that GFRP can be used in HSC to enhance the stiffness of uncracked concrete sections, thereby allowing the GFRP to reach higher strains. Moreover, increasing the longitudinal reinforcement from 2.2% to 3.3% slightly enhanced the flexural behavior of the eccentrically loaded columns. Hadi et al. (2017) investigated 12 circular columns made with HSC. The testing included axial and eccentric loading of the columns. Under axial load, the HSC specimens lost half their axial-load capacity compared to the steel-reinforced columns. This was followed by a sudden loss of strength and brittle failure pattern. The researchers also found that taking the GFRP bars subjected to compression stresses into consideration led to accurate results that were quite consistent with the experimental results.

In order to better understand and judge the performance of GFRP-reinforced HSC columns, the flexural stiffness, deflection, and induced strains should be monitored and compared to NSC columns. For the sake of comparison, the structural behavior of the tested specimens herein is compared to those tested by Guérin et al. (2018b). Zadi and Nanni (2017) developed theoretical equations to measure column effective stiffness at service load as well as general and simplified equations for columns to replace the ACI equations. Hadhood et al. (2018) analytically investigated circular columns in order to plot their moment–curvature relationships and to measure and predict their effective flexural strength at different stages of loading. They also proposed an analytical model that was consistent with the experimental results because the contribution of the GFRP bars in compression was fully taken into consideration. In addition, Hadhood et al. (2018) proposed two equations for calculating the relative flexural stiffness of circular GFRP-reinforced columns that considered the effect of changing the reinforcement ratio and the applied eccentricity. The effective flexural-stiffness expressions proposed by these authors are used to compare their applicability to the results for HSC columns.

So far, limited research has been conducted on the eccentric behavior of HSC columns fully reinforced with GFRP bars. More investigations into the structural behavior and effective flexural stiffness for full-scale specimens with a square cross section are presented herein. The test results reported in this paper relate to 12 full-scale square HSC columns reinforced with GFRP bars and ties subjected to different values of eccentricity. The test parameters included longitudinal-reinforcement ratio and eccentricity-to-diameter ratio.

6.3. RESEARCH SIGNIFICANCE

There is little in the literature on the structural behavior of large-scale HSC columns tested under eccentric loading. This experimental study provides unique test results for a series of full-scale concrete columns reinforced with GFRP bars and ties. This study focused on investigating the effect of using different GFRP-bar reinforcement ratios (0.5%, 1.0%, and 2.5%) on the failure mode, acquired axial and flexural strength, and the corresponding moment–curvature and flexural stiffness. A parametric investigation was included to cover a wide range of concrete strengths and reinforcement ratios and to demonstrate their effect on flexural stiffness. This study provides greater understanding of and confidence in using GFRP bars in HSC columns. It also establishes design provisions and recommendations for engineers in designing HSC columns with GFRP

reinforcement. Moreover, the findings of this research will support the work of North American technical committees engaged in developing standards and design provisions for GFRPRC columns made with high-strength concrete subjected to eccentric load.

6.4. EXPERIMENTAL INVESTIGATION

6.4.1. Materials

Reinforcing bars **–** Sand-coated GFRP bars and ties were used to reinforce the GFRPRC column specimens in the longitudinal and transverse directions. The GFRP reinforcement was manufactured using the pultrusion process (TUF-BAR Canada, 2017). #5 (15 mm in diameter), #6 (20 mm in diameter), and #8 (25 mm in diameter) GFRP bars were used as longitudinal reinforcement for the GFRP reinforced columns. As shown in **Fig. 5.1**, #3 (10 mm in diameter) GFRP ties and cross ties were used in the transverse direction. Closed ties and C-shaped cross ties (330 mm length and 100 mm width) were used to confine the series G1 columns, while closed ties (330 mm length and 400 mm width) and closed cross ties (330 mm length and 180 mm width) were used to confine the series G2 columns. GFRP cross ties were used at the center of the cross section with tail lengths equal to $12d_b$, as shown in **Fig. 5.1**. All the GFRP reinforcement used was classified as Grade III in accordance with CSA S807. The ultimate tensile strength, f_{fu}, and the modulus of elasticity, E_f, of the longitudinal GFRP bars (#5, #6, and #8) and the straight portion of the bent GFRP bars (#3) were determined according to ASTM D7205. Nominal cross-sectional area (CSA S807) was used to calculate of the tensile properties (Table 6-1). **Table 6-1** provides details about the reinforcement.

Table 6-1– Mechanical properties of the GFRP reinforcement

Bar Size	d_b (mm)	A_f [a] (mm²)	A_{im} [b] (mm²)	E_f [c] (GPa)	f_{fu} [c] (MPa)	ε_{fu} (%)
#3	10	71	86.8	63.7	1212 [c]	2.2
#5	15	199	252	62.6	1125	2.1
#6	20	285	309	62.7	1036	2.0
#8	25	510	530	61.7	1001	1.9

[a] Nominal cross-sectional area.
[b] Immersed cross-sectional area (measured by immersion tests).
[c] Tensile strength of straight bars

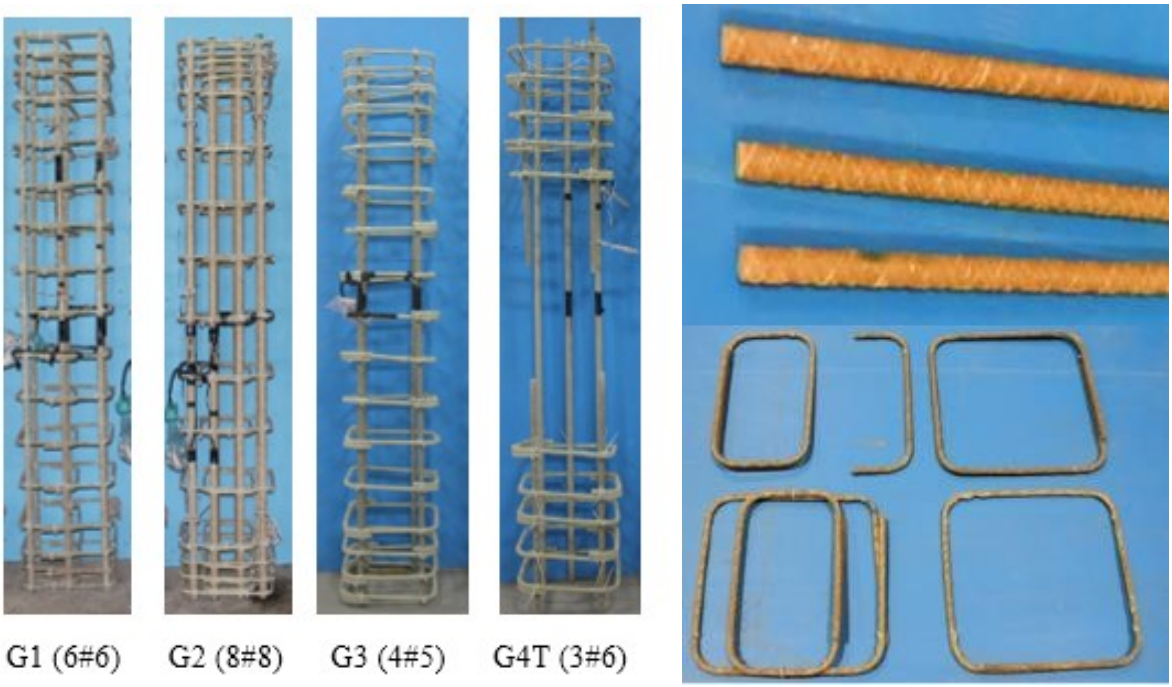

(a) (b)

Figure 6-1 – Overview of the (a) GFRP cages and (b) GFRP bars, ties, and crossties used.

HSC concrete **–** Ready-mixed HSC with a target 28-day strength of 70 MPa was used with 1 m^3 of HSC containing 490 kg of cement, 812 kg of sand, and 1032 kg of aggregate with a water-to-cement ratio (w/c) of 32%. The concrete strength for each batch was determined by testing three 150 × 300 mm cylinders on the day of testing. The average compressive strength of the tested cylinders was 71.2 MPa.

6.4.2. Specimen Design and Fabrication

The specimens were designed to investigate the performance of HSC columns under eccentric loading. Twelve full-scale specimens were prepared with a square cross section of 400 mm and height of 2000 mm (see **Fig. 5.2**). The concrete cover was kept constant at 40 mm for all specimens. The test specimens were designed and divided into four series (G1, G2, G3, and G4T) according to different reinforcement ratios: 0.5%, 1%, 2.5%. Specimen design and analysis were carried out according to the recommendations in recent research studies (Choo et al. 2006a, b; Zadeh and Nanni 2013; Hadhood et al. 2016a). The GFRP longitudinal-reinforcement ratio was determined to allow concrete crushing to occur before bar rupture, as it is the preferable mode of failure for

GFRPRC members (ACI 440.1R-15). Series G1 specimens had a minimum longitudinal-reinforcement ratio of 1% (as per ACI 318-1). CAN/CSA S806-12, however, allows for a reinforcement ratio that can be less than 1% but at least 0.5% (Clause 8.4.3.8). Series G3 specimens had a ratio of 0.5%, while series G2 specimens had a ratio of 2.5%. The results for series G1 specimens were compared to that for series G2 and G3 specimens. The series G4T specimens had three #6 GFRP bars on the tension side with no compression bars in order to evaluate their strength relative to series G1 specimens and demonstrate the importance and contribution of compression reinforcement in columns.

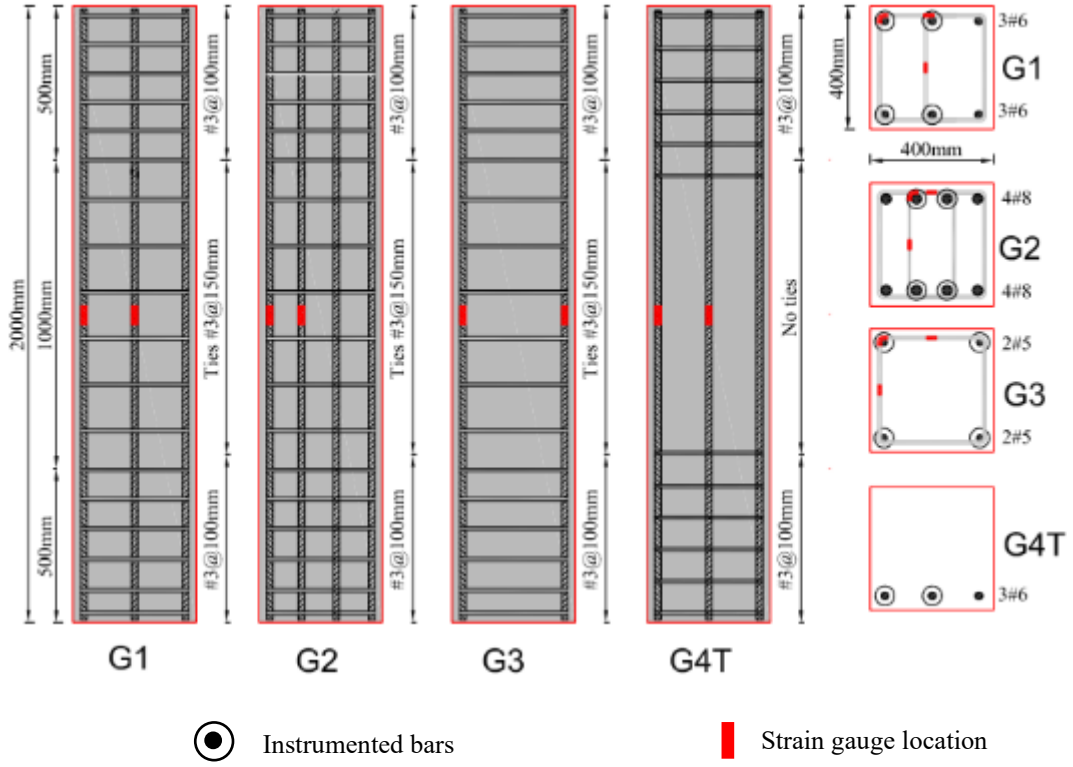

Figure 6-2– Dimension and details of four groups (G1, G2, G3, and G4T)

Four eccentricities were used to develop the experimental P–M interaction diagrams with a wide range of eccentricities from low to high. According to Zadeh an Nanni (2017), the approximate eccentricity range at which cracking and its effect is more pronounced lies in the range of $0.25 \le e/h \le 0.50$. For eccentricities $e/h > 0.5$—at which the resultant axial force is actually located outside the section—the columns simulated beam flexural behavior due to the low levels of axial load. The eccentricities were selected to cover as many points in-between under axial- and flexural-stress behavior: $e/h = 0.2$ (low eccentricity; compressive stress behavior is dominant); e/h

= 0.3–0.4 (moderate eccentricity; compressive–tensile stress behavior is the dominant transition zone); and e/h = 0.6 (high eccentricity; tensile-stress behavior is the dominant transition zone or flexural behavior). The applied eccentricity values were selected to provide data about the eccentric behavior of square HSC columns with GFRP reinforcement and draw their corresponding P–M interaction diagrams. Series G1 and G2 specimens were tested at all the chosen eccentricities. The numbers 80, 120, 160, and 240 (e/h = 0.2, 0.3, 0.4, and 0.6) after the e symbol represent the applied eccentricity in millimeters. Series G3 specimens were tested at extreme eccentricities (e = 80, and 240 mm) to subject the column to maximum compressive and tensile stresses among the selected range of testing. Series G4T specimens were tested at e = 80 and 160 mm, representing the boundaries at which the member still behaves as a column. The range of reinforcement ratios was selected to observe different potential cracking patterns and modes of failure. The columns were reinforced horizontally with #3 GFRP ties with a spacing of 150 mm ($16d_b/2$, where d_b is the bar diameter), resulting in a value of 152 mm. The tie spacing was chosen based on ACI 318-14 ($16d_b$), as per Sections 10.7.6.1.2 and 25.7.2.1 for steel-reinforced columns. The spacing was reduced to $16d_b/2$ to account for the difference in moduli of elasticity between GFRP and steel reinforcement (Nanni et al. 2014). The tie spacing for all specimens was reduced to 50 mm outside the test region over a length of 259 mm (10.2 in.) at both column ends to avoid premature failure. **Table 6-2** shows the test matrix for the tested specimens.

6.4.3. Instrumentation

Each column was instrumented with LVDTs measuring the lateral deflection at mid-height as well as at the top and bottom quarter-heights. Strains in the longitudinal reinforcing bars and transverse ties were measured with electrical resistance strain gauges with a gauge length of 6 mm. Four strain gauges were installed at the mid-height level: two for bars under compression and two for bars under tension. Three strain gauges were located at different locations on the tie at the mid-height section. Strain gauges 60 mm in length were mounted on the concrete outer surface at mid-height to measure compressive strain during testing.

Table 6-2– Test matrix

Series	Specimen ID	Test Eccentricity (mm)	Longitudinal Reinforcement	Transversal Reinforcement
G1	G1e80	80	6 #6 GFRP	#3 GFRP@150
	G1e120	120	6 #6 GFRP	#3 GFRP@150
	G1e160	160	6 #6 GFRP	#3 GFRP@150
	G1e240	240	6 #6 GFRP	#3 GFRP@150
G2	G2e80	80	8 #8 GFRP	#3 GFRP@150
	G2e120	120	8 #8 GFRP	#3 GFRP@150
	G2e160	160	8 #8 GFRP	#3 GFRP@150
	G2e240	240	8 #8 GFRP	#3 GFRP@150
G3	G3e80	80	4 #5 GFRP	#3 GFRP@150
	G3e240	240	4 #5 GFRP	#3 GFRP@150
G4T	G4Te80	80	3 #6 GFRP	N/A
	G4Te160	160	3 #6 GFRP	N/A

6.4.3.1. Testing Procedure and Test Setup

Prior to testing, all the specimens were capped at both ends with a thin layer of high-strength cement grout for leveling and to ensure uniform distribution of the applied load across the column's cross section. Rigid steel caps were fabricated and attached to both ends to allow for applying different eccentricities and prevent premature failure at both ends. The load was applied through two steel roller bearings bolted to the steel end caps. The columns were tested using a 11,400 kN MTS testing machine at the Canadian Foundation for Innovation (CFI) Structural Laboratory at the University of Sherbrooke. The machine's internal load cell was used to measure the axial applied load and machine-head displacement, respectively. The test started with load control (2.5 kN/s) up to a load level equal to 70% of the estimated peak load. Afterwards, the test continued using displacement control at a rate 0.002 mm/s to prevent sudden failure and track the failure process. Load, lateral deflection, and reinforcement and concrete strains were monitored and recorded

during testing with an automatic data-acquisition system connected to a computer. **Figure 5.3** shows the test setup, MTS testing machine, and data-acquisition system used.

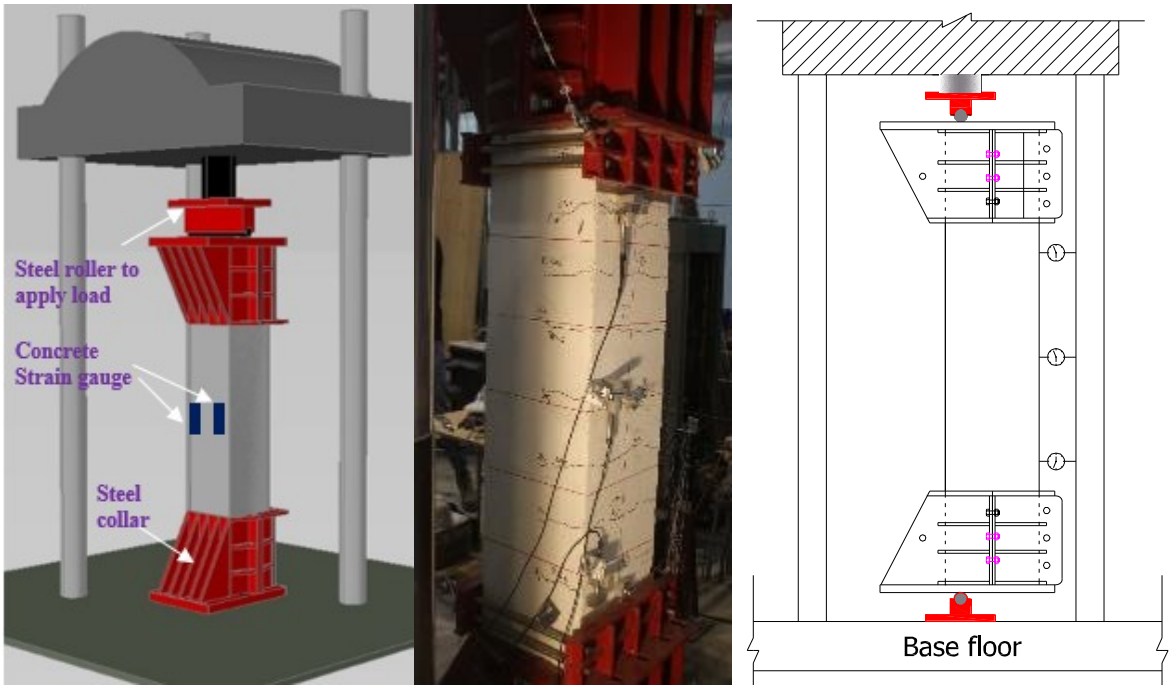

Figure 6-3 – Test setup.

6.5. OBSERVED BEHAVIOR AND TESTS RESULTS

6.5.1. Cracking and Failure Modes

The failure mode and crack pattern were more significantly affected by the level of eccentricity than the GFRP longitudinal-reinforcement ratio. As expected, the failure was located at the mid-height of all the tested column specimens. Two main failure modes were observed: (1) compression controlled in which the failure initiated by tensile cracks, followed by concrete crushing and (2) tension-controlled, which was characterized by large deflection values and high tensile strains in the GFRP bars (over 5000 $\mu\varepsilon$), and wide tensile cracks before concrete crushing.

6.5.1.1. Columns under Low Eccentricity (0.2h)

The crack patterns and failure process of specimens G1e80, G2e80, and G3e80 were similar in sequence. They first experienced narrow tensile cracks, followed by cracks on the compression side, before reaching peak load, leading to cover spalling. Once the cover spalled, the tensile cracks widened and progressed diagonally towards the middle zone. Final resistance was marked by brittle crushing of the concrete core and buckling of GFRP bars on the compression side. Such columns had limited post-peak behavior due to crushing of most of the concrete core

6.5.1.2. Columns under Moderate Eccentricity (0.3h and 0.4h)

The cracking patterns and failure modes differed from columns tested under low eccentricity. **Figure 5.4** shows the final failure mode and cracking appearance. Greater axial and deformation values were observed, leading to an increase in both the number and width of tensile cracks. As peak load was approached, vertical cracks formed on the compression side, indicating cover spalling. This failure mode can be described as compression failure with larger tensile strains developing in the GFRP rebars; the behavior was initiated by flexural cracking. The post-failure behavior was characterized by gradual degradation of the concrete core and widening of the tensile cracks as the displacement increased. Large axial and lateral deformations also occurred.

6.5.1.3. Columns under High Eccentricity (0.6h)

The behavior of the columns tested at this eccentricity (specimens G1e240, G2e240, and G3e240) was governed mainly by the applied flexural stresses. The specimens developed early tensile cracks on the tension side when the applied tensile stress equaled the concrete tensile strength. Once the cracks appeared, the tensile bars were subjected to large strain values, which increased very rapidly and resulted into a noticeable increase in the number and width of the tensile cracks along the tensile surface. At peak load, the columns showed the greatest lateral and axial deformations and lowest axial resistance. The failure was marked by cover spalling, and the columns experienced a slight decrease in maximum resistance. The failure of these columns was classified as tensile-controlled, due to the large acquired rotation and the axial and lateral deformations. Increasing the reinforcement ratio to 2.5% significantly decreased the crack widths. The post-failure behavior was characterized by crushing of the compression block, widening flexural-tensile cracks, and sudden

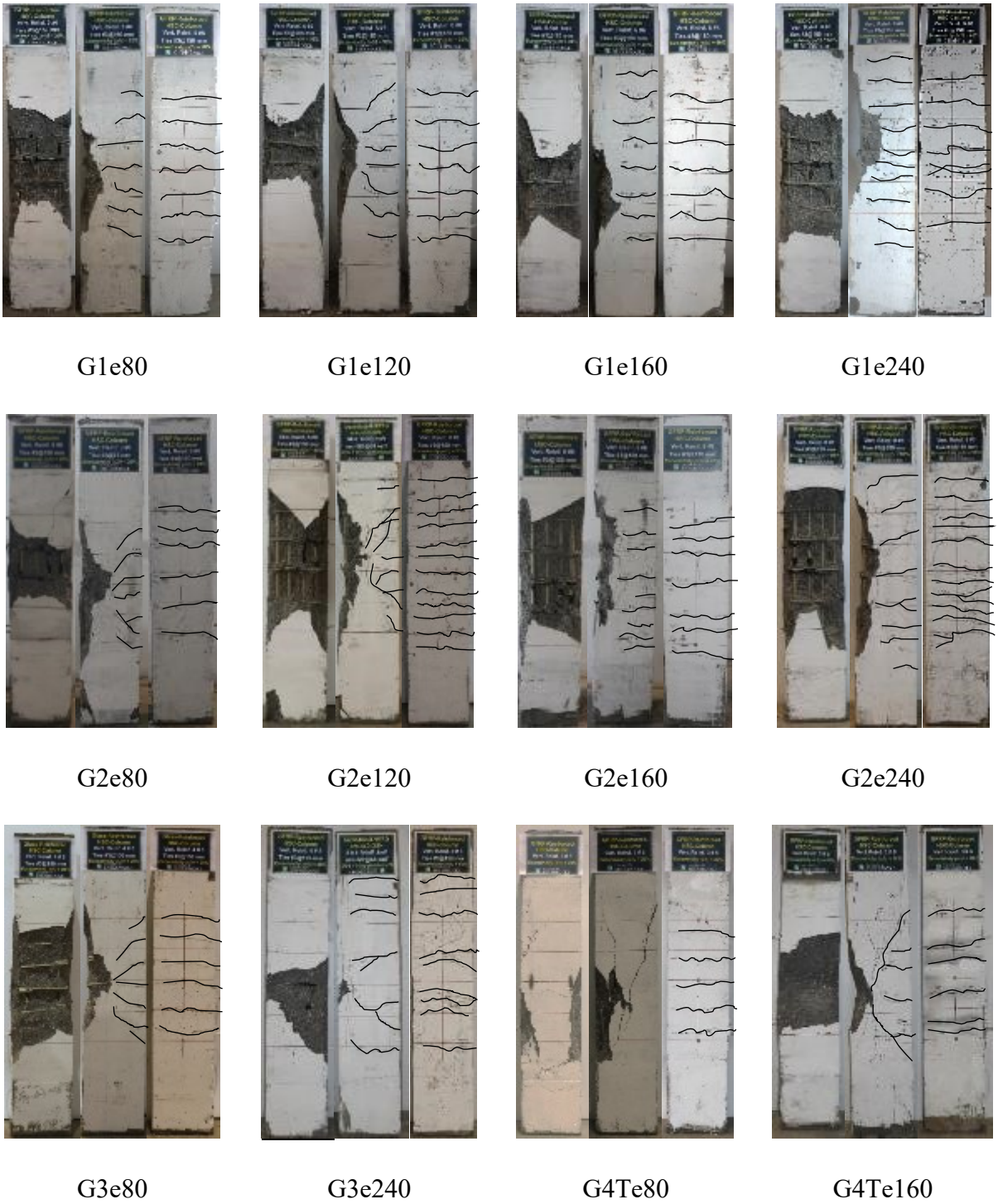

Figure 6-4 – Failure mode for all the tested specimens for compression side, side view, and tension side, respectively.

Increases in both axial and lateral displacements. Loading continued until excessive lateral deformation was observed or the tensile-bar reading approached rupture strains. In general, these columns failed in a more ductile manner than those tested under lower eccentricities. No GFRP-bar damage was observed on either the tension or compression side.

6.5.2. Concrete and GFRP-Bar Strain Behavior

Columns Tested under Low Eccentricity (20%) – The crack patterns and failure mode were the main parameters influencing the developed bar strains and the axial and lateral deformations for the tested columns. Specimens G1e80, G2e80, and G3e80 reached peak load at maximum concrete strains of -2,580, -3,313 and -2,600 $\mu\varepsilon$, respectively. Simultaneously, the recorded axial deflections (**Fig. 5.5**) were 7.35, 6.69, 7.79 mm, with corresponding lateral deflections (**Fig. 5.6**) of 4.88, 5.31, and 4.62 mm respectively. The corresponding recorded strains were -2,500, -3,100, and -2,220 $\mu\varepsilon$ for the compressive bars and 380, and 270, 330 $\mu\varepsilon$ for the tensile strains in specimens G1e80, G2e80, and G3e80 (**Figs. 5.7 (a), (b), and (c)**). Tensile cracks started to appear at a late stage of loading compared to the other columns in the same groups. The cracks appeared at nearly 35% of the peak load resisted by the columns tested with an eccentricity-to-depth ratio of *0.2h*. The general behavior of the columns is classified as compression failure as most of the concrete section was subjected to compressive stresses and, at failure, a large area was crushed on the compression side of the columns.

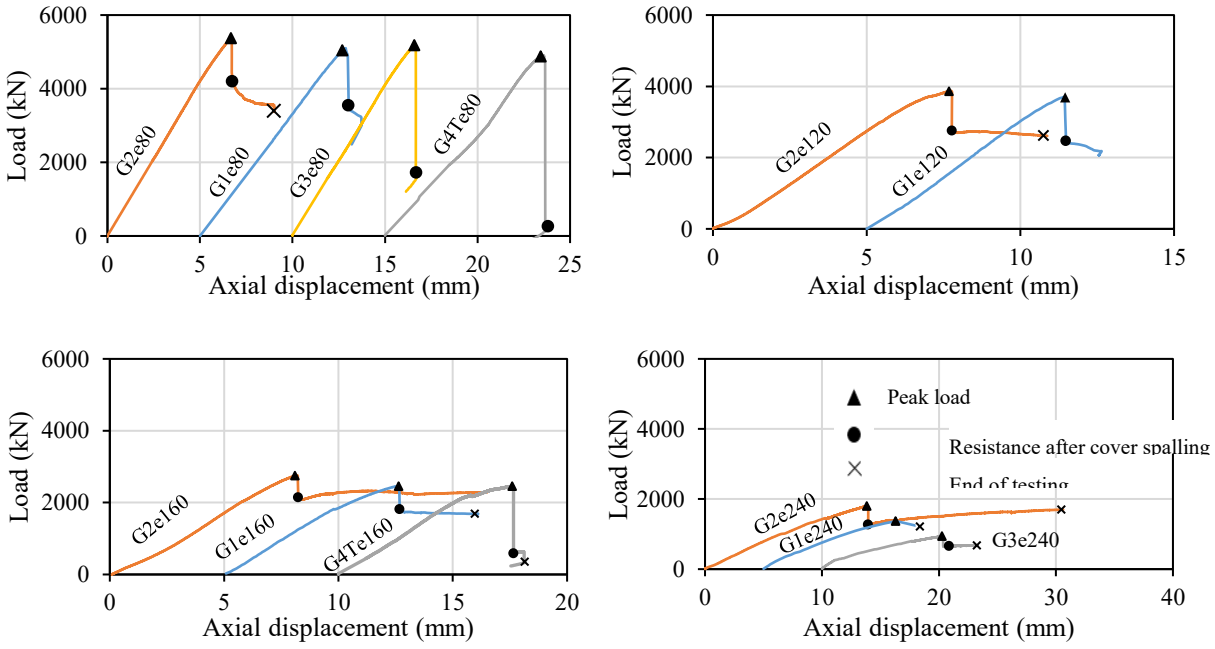

Figure 6-5 – Axial load–axial displacement at mid-height.

Columns Tested under Moderate Eccentricity (30% and 40%) – A further increase in eccentricity changed the induced strains in the compressive and tensile bars. Specimens G1e120 and G2e120 achieved maximum peak-load resistances of 3,700 and 3,900 kN, respectively, recording concrete strains of -3,100 and -2,600 $\mu\varepsilon$. Simultaneously, the compressive bars had compressive strains of -3,400 and -2,800 $\mu\varepsilon$, tensile strains of 2,900 and 2,300 $\mu\varepsilon$, and lateral deflections of 7.62 and 8.03 mm for columns G1e120 and G2e120, respectively. Once the peak load was reached, the columns experienced estimated strength decreases of 34% and 28%, respectively, due to spalling of the concrete cover.

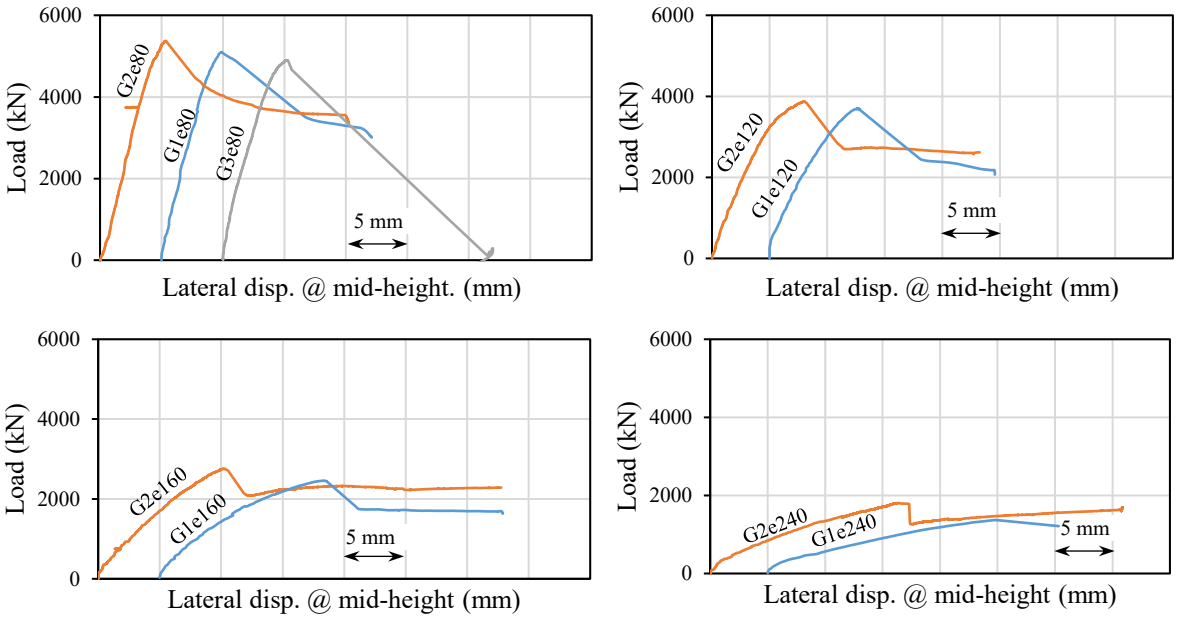

Figure 6-6 – Axial load–lateral displacement at mid-height.

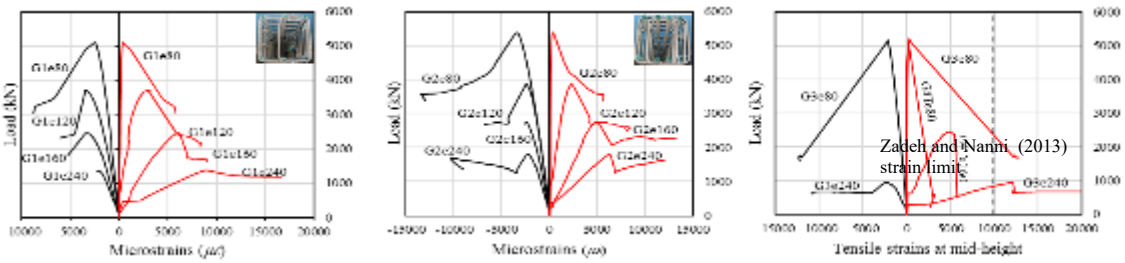

(a) (b) (c)

Figure 6-7 – Axial load–reinforcement strain @ mid-height for series (a) G1, (b) G2, and (c) G3, and G4T.

Similar overall behavior was observed for the columns tested with eccentricity equal to 40% of the depth. As expected, lower peak resistance was achieved and more axial and lateral deflections were observed. Column G1e160 exhibited axial deformation of 11.3 mm and lateral deformation of 15.1 mm. The concrete reached ultimate compressive strains of -3,400 and -3,100 $\mu\varepsilon$ at the extreme compression surface in specimens G1e160 and G2e160 as well as maximum axial-load resistances of 2,400 and 2,700 kN, respectively. Consequently, the recorded compressive strains for the GFRP bars were equal -3,300 and -2,400 $\mu\varepsilon$ and the corresponding tensile strains were 6,000 and 4,900 $\mu\varepsilon$ for specimens G1e160 and G2e160, respectively. The columns lost 29% and 54% of their strength, respectively. As a result of cover spalling, both columns experienced sudden increases in the axial and lateral deformations due to the loss of column stiffness. The tensile cracks also increased in width and depth. The measured strains in the GFRP bars before the end of testing of specimen G1e160 were -8,200 and 9,600 $\mu\varepsilon$ for the bars under compression and tension, respectively, compared to 13,300 $\mu\varepsilon$ for the tension bars in specimen G2e160.

Columns Tested under High Eccentricity (60%) **–** The behavior of columns under this level of eccentricity is considered to be similar to flexural beams. Three columns were tested with initial eccentricity values of 240 mm (G1e240, G2e240, and G3e240). Tensile cracking initiated at an early stage of loading in the case of all three groups. As loading progressed, the cracks grew wider and more tensile strains developed in the GFRP tensile bars, associated with excessive lateral and axial deformation. The maximum axial resistance sustained by specimens G1e240, G2e240, and G3e240 were 1367, 1800, and 945 kN, respectively. At peak load, the axial deflection was 11.3, 13.9, and 10.3 mm, while the lateral deflection was 15.1, 16.4, and 15.3 mm for specimens G1e240, G2e240, and G3e240, respectively. As a result of these deflection values, these specimens recorded the greatest tensile strains among all the tested columns. At peak load, the tensile strains were 9,100, 6,300, and 12,000 $\mu\varepsilon$. In contrast, the compression-bar strain values were 2,100, 2,200, 2,200 $\mu\varepsilon$ for specimens G1e240, G2e240, and G3e240, respectively. The concrete-strain values at the compression surface were 3,100, 3,150, and 2,600 $\mu\varepsilon$. In the post-peak phase, the columns experienced strength losses of 11%, 30%, and 32%, respectively. No signs of anchorage problems were observed in any of the specimens. Test observations revealed no tensile or compression rupture in any of the GFRP bars. The columns also reached peak load without any premature failure in the GFRP bars or large deformations; neither was there any deep cracking before the full tensile capacity of the bars was reached. **Figure 5.8** shows the strain profile for the tested columns at the

peak load, and the location of the neutral depth for series G1, G2, and G3 under different eccentricities.

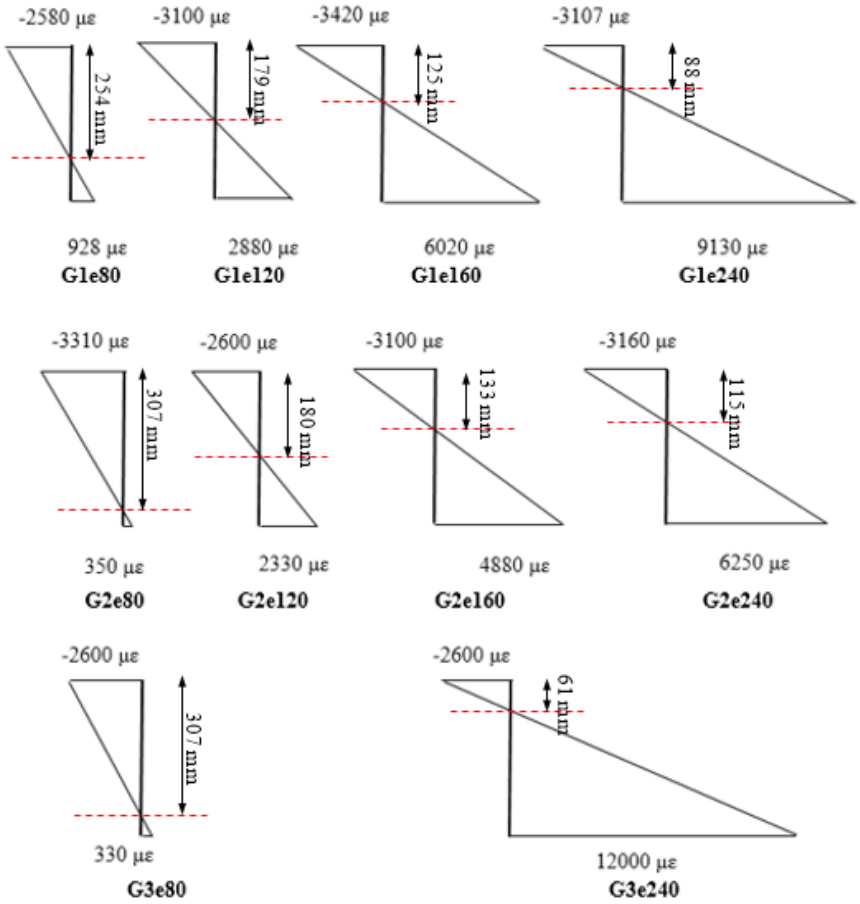

Figure 6-8 – Strain profile for all the tested columns at peak load.

6.6. DISCUSSION

6.6.1. Effect of Reinforcement Ratio

Three different GFRP reinforcement ratios were used (0.5%, 1%, and 2.5%). The test results indicate that increasing the reinforcement ratio slightly increased the maximum axial load resisted by the columns tested under an eccentricity value of 80 mm (see **Fig. 5.9 (a) and (b)**). As the applied eccentricity increased, the strength difference between the three reinforcement ratios increased.

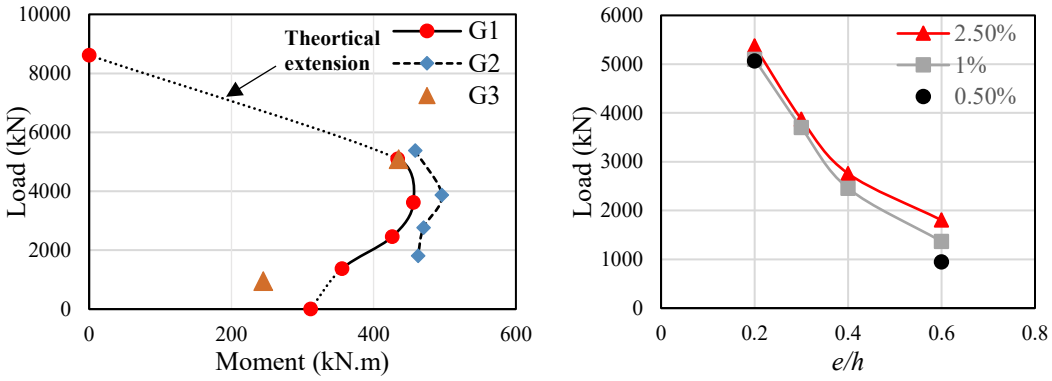

(a) (b)

Figure 6-9 – Strength of the tested columns for series G1, G2, and G3 (a) Axial–flexural strength of columns; (b) axial load versus eccentricity-to-depth ratio.

Increasing the reinforcement ratio from 1% to 2.5% increased the axial strength of the columns by 5.0%, 4.6%, 12.0%, and 32% at eccentricity values of 80, 120, 160, and 240 mm, respectively. Increasing the reinforcement ratio from 0.5% to 1% yielded similar levels of axial resistance for columns with e/h = 0.2 and increased by 45% when tested at e/h = 0.6. These percentages clearly indicate that the effect of reinforcement is more pronounced at higher levels of eccentricity, while having negligible effect at low levels of eccentricity. This could be attributed to the difference in the modes of failure and the location of the neutral axis within the concrete section, as shown in **Fig. 5.8**. For the columns controlled by concrete crushing, tested at a low e/h ratio, the axial resistance was mainly governed by the area of concrete. For the columns tested at a high level of eccentricity, the failure was marked by large lateral deflections, accompanied by wide and deep tensile cracks, and governed by the maximum developed tensile strains in the GFRP bars. Using higher reinforcement ratios decreased the maximum tensile strains in each bar. After cover spalling, the columns typically lost some axial strength. The percentage of strength loss after cover spalling decreased as the reinforcement ratio increased, since a greater area of GFRP bars was available in compression to compensate for the strength loss resulting from cover spalling. This is more obvious for columns tested under a low level of eccentricity. At a reinforcement ratio of 2.5%, the columns could reach a second peak after the strength loss. This behavior was obvious in the columns tested at eccentricity-to-depth ratios of 0.3, 0.4, and 0.6h. For the columns tested with a reinforcement ratio of 0.5%, specimen G3e80 behaved similarly to the other two columns (G1e80 and G2e80) and achieved approximately the same axial strength. The GFRP bars in specimen G3e240,

however, developed very high tensile strains of 12,000 $\mu\varepsilon$, which is more than the maximum recommended level (10,000 $\mu\varepsilon$) according to Zadeh and Nanni, (2013). Thus, the minimum reinforcement ratio of 1% cannot be reduced for HSC, although HSC has less creep and shrinkage than NSC.

6.6.2. Effect of Compression Reinforcement

The effect and necessity of compression reinforcement can be demonstrated by comparing the structural behavior of series G1 and G4T specimens. Specimen G4Te80 achieved a maximum axial resistance of 4,900 kN, compared to 5,100 kN for specimen G1e80. At an eccentricity level of 160 mm, G4Te160 and G1e160 had maximum axial-resistance values of 2,452 and 3,107 kN, respectively. Based on these results, the assumption of replacing GFRP bars with an equivalent area of concrete can be considered valid. The main difference between the two groups can be seen in the distinct failure pattern. The failure pattern of series G4T specimens was characterized by sudden and brittle failure at both levels of eccentricity. Moreover, the columns lost their axial-resistance capacity once the peak axial value had been reached. The failure was also due to the combined effect of flexure (minimal for specimen G4Te80) and shear. This can be attributed to the lack of the longitudinal bars, which act as dowels to resist sliding and provide an inner core in the columns. That would provide axial resistance after cover spalling and post-peak behavior. As a result, the tensile bars in specimen G4Te80 recorded negligible tensile strains until the peak load was reached. while those in G4Te160 had a maximum tensile strain of 4,900 $\mu\varepsilon$ at peak load.

6.6.3. Effect of Using HSC

To demonstrate the effect of using HSC, the test results presented herein were compared to results in the literature for NSC columns reinforced with GFRP ties and bars tested at the University of Sherbrooke by Guérin et al. (2018b). Their research involved square columns of similar dimensions (400 mm square and a concrete strength of 42.3 MPa). The columns were tested at eccentricity levels of 40, 80, 160, and 320 mm. For valid comparison, columns tested under the same eccentricity-to-depth ratios were chosen: 0.2 and 0.4h (specimens G1e80*, G1e160*, G3e80*, and G3e160* made with NSC) tested by Guérin et al. 2018b were compared to the results of the counterpart specimens tested in this study as presented in Table 6-3. It should be noted that ACI Committee 363 (363R-10) defines high-strength concrete as having a specified compressive

strength of 55 MPa or greater. The columns behaved similarly with both types of concrete. The axial capacity of HSC columns with reinforcement ratio of 1% increased by 52% and 26%, while the tensile strains increased by 115% and 100% when applied to eccentricity-to-depth ratio of 0.2 and 0.4*h*, respectively. Moreover, the lateral deflection recorded for column G1e80*(NSC) at its peak-load level was 4.8 mm, compared to 2.88 mm for specimen G1e80. At an eccentricity level of 160 mm (eccentricity-to-depth ratio of 0.4*h)*, the lateral displacement of column G1e160 was 8.9 mm at ultimate load, and the lateral displacement for specimen G1e80 at the same load level was 8.2 mm. Their capacities increased by 40% and 25%, respectively, when a reinforcement ratio of 2.5% was used. The increase in the flexural capacity also led to a 36% increase in the developed tensile strains in the GFRP bars at loading with an eccentricity value of 160 mm. The lateral deflection decreased from 5.2 and 9.6 mm for columns G3e80* (NCS) and G3e160* (NCS) to 3.24 and 7 mm when the concrete strength was 41.2 and 71 MPa, respectively.

Table 6-3 – Summary of results

Series	*e/h*	P_{peak} (kN.m)	e (mm)	Δ (mm)	ε tension (με)	ε comp. (με)	M_{tot} (kN.m)	Curvature/*d*	*μ*
G1	0.2	5100	80	4.89	380	-2490	433	0.0029/d	1.04
	0.3	3621	120	5.84	2880	-3390	455	0.0063/d	1.14
	0.4	2457	160	13.35	6100	-3300	426	0.0094/d	1.18
	0.6	1367	240	19.71	8830	-2100	355	0.0109/d	1.27
G2	0.2	5137	80	3.8	348	-3400	411	0.0037/d	1.07
	0.3	4213	120	7.03	2800	-2800	506	0.0056/d	1.15
	0.4	3019	160	8.12	4880	-1980	483	0.0069/d	1.16
	0.6	1338	240	15.21	6250	-2140	321	0.0084/d	1.17
G3	0.2	5068	80	5.6	330	-2400	455	0.0027/d	N/A
	0.6	944	240	15.3	12000	-2200	427	0.0142/d	N/A
G4T	0.2	4900	80	5.6	310	N/A	455	N/A	N/A
	0.4	2450	160	14.1	4900	N/A	427	N/A	N/A
G1(NSC)*	0.2	3357	80	4.48	430	-2000	283	0.0024/d	N/A
	0.4	1942	160	8.88	3200	-2900	328	0.0061/d	N/A
G3(NSC)*	0.2	3790	80	5.22	650	-2600	323	0.0033/d	N/A
	0.4	2110	160	9.40	3600	-2500	358	0.0061/d	N/A

Notes: *e* is eccentricity; *h* is column width; P_{peak} is peak axial load; Δ is the lateral deflection due to the second-order effect; *ε* tension is the developed tensile strains at peak load; *ε* tension is developed compressive strains at peak load; *μ* is the ductility index; and * specimens reported by Guérin et al. (2018b)

The effect of increasing the concrete strength can be seen in the decreased column ductility, which is expected to occur when the concrete strength is increased. The developed tensile strains in the GFRP reinforcement also increased significantly. These conclusions are consistent with those of Yost and Gross (2003) and El-Nemr et al. (2013), but the HSC significantly increased the axial capacity of the columns with the same cross section. Designers can also use smaller cross sections to withstand the same load resisted by NSC.

6.7. MOMENT–CURVATURE RELATIONSHIP

Curvature is an important feature for eccentric columns and beams. The curvature can be calculated using the recorded strain for the GFRP longitudinal reinforcement on the compression and tension sides. Thus, the curvature values for all the tested specimens were calculated with Eq. 1 by subtracting the strains on the outermost compression and tension bars and dividing by the distance between them. **Table 6-3** provides the recorded strains and calculated curvature. The curvature of the columns can be used to judge the type of failure. ACI 318-14 (Section R21.2.2) considers that failure is tension-controlled whenever the net tensile strain in the extreme tension reinforcement is sufficiently high ($\varepsilon \geq 0.005$) or the curvature is greater than $0.008/d$, for which warning of failure in the form of excessive deflection and cracking can be expected. In addition, the test results indicate that the curvatures of typical GFRP-reinforced concrete beams at failure would vary between $0.0138/d$ and $0.0176/d$ for tension-controlled failures (Shield et al. 2011; El-Nemr et al. 2013; Kassem et al. 2011). This curvature range is close to the curvature of specimens G1e240 and G2e240. Accordingly, the failure of these columns can be called tension-controlled. By calculating the curvature from the experimental results of the tested columns, the M_{exp}–ψ_{exp} response was plotted in **Fig. 5.10** for series G1 and G2 specimens as solid lines; the dotted line represents the analytical results (discussed below).

$$\psi = \frac{\varepsilon_t - \varepsilon_c}{d} \tag{5.1}$$

$$EI_{\text{sec}} = \frac{M}{\psi} \tag{5.2}$$

The secant stiffness was determined for each of the tested specimens in series G1 and G2 by dividing the moment by the corresponding calculated curvature. **Figure 5.11** shows the change in the section stiffness with loading up until peak load. It should be obvious that increasing the applied

eccentricity greatly affected column stiffness. The columns tested at *e/h* = 0.6 experienced sharp drops in stiffness before reaching a plateau. This behavior clearly shows that the columns subjected to such eccentricities were dominated by flexural stresses and behaved similarly to flexural beams. Based on these diagrams, the flexural stiffness at the service- and ultimate-load levels can be determined. The ultimate load was defined as $0.48P_n = 0.80 \times 0.60P_n$ for all specimens in series G1 and G2.

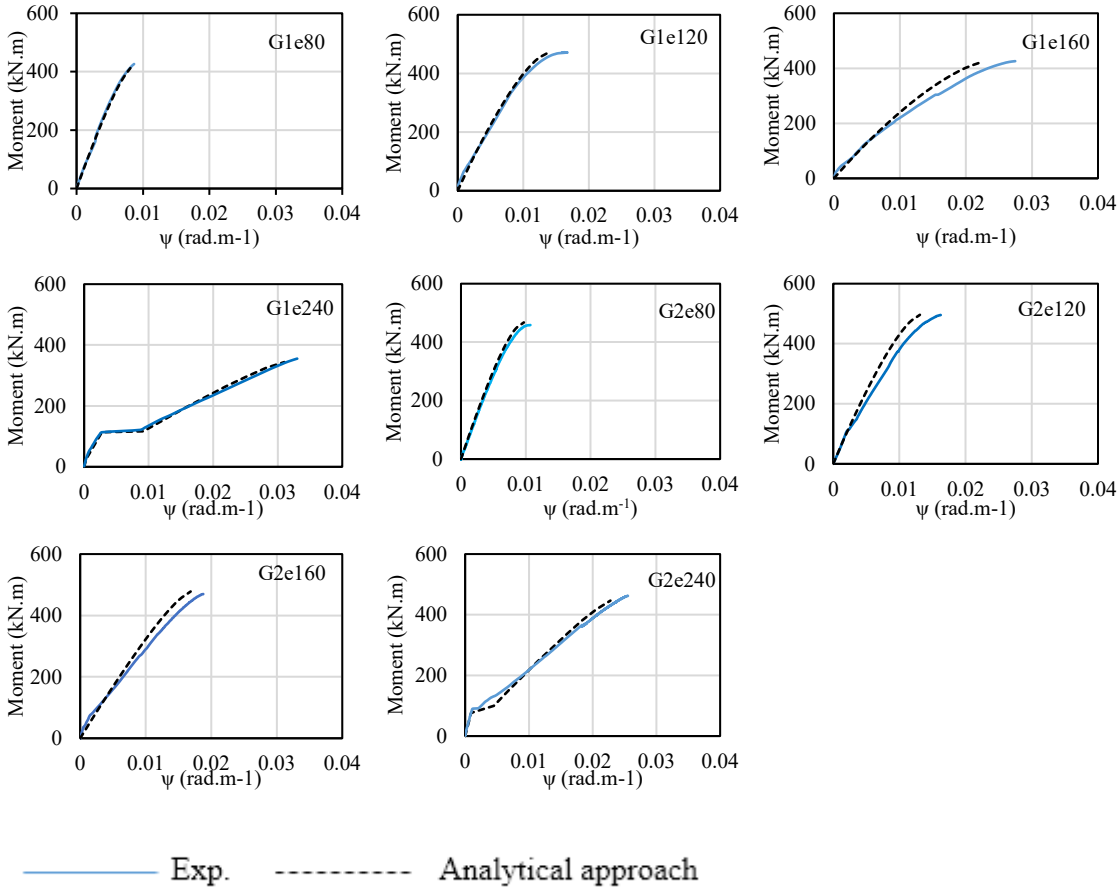

Figure 6-10 – Comparison of the experimental and analytical *M-ψ* for series G1 and G2.

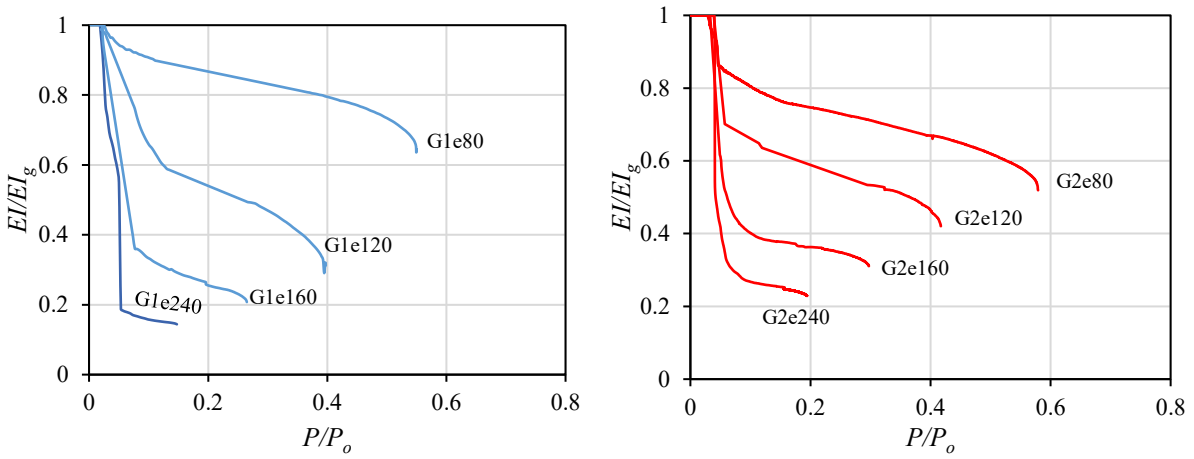

Figure 6-11 – Influence of changing the applied eccentricity and P/P_o on EI/EI_g for series G1 and G2.

6.8. DUCTILITY

HSC's higher strength comes at the cost of reducing the ductility of the structural members. Naaman and Jeong (1995) used the energy-based definition to define ductility as the ratio between the total energy and the elastic energy. The absorbed-energy approach (Naaman and Jeong, 1995) was used to measure the ductility of the GFRP-reinforced columns. The calculation requires the combined strain ζ, which is the combined strain for the average strain ε_{av} at the geometric center multiplied by the curvature ψ.

$$\zeta = \varepsilon_{av} + (e + \Delta)\Psi \tag{5.3}$$

The ductility index is described as follows:

$$\mu_e = \frac{1}{2}\left(\frac{E_{tot}}{E_{el}} + 1\right) \tag{5.4}$$

where E_{tot} is the total energy computed as the area under the load–deflection curve, and E_{el} is the elastic energy released upon failure, computed as the area of the triangle formed at the failure load by the line having the weighted average slope of the two initial straight lines of the load–deflection curve. **Table 6-3** provides the computed ductility indexes for the GFRP-reinforced specimens, which shows that increasing the applied eccentricity increased the measured ductility of the tested columns. This increase in the ductility index resulted from the increased developed tensile strains

in the tensile bars and the linear elastic nature of the GFRP bars. In the case of steel-reinforced columns, failure is governed by the yielding strain of the steel bars, which make the ductility index nearly constant despite the applied eccentricity.

6.9. Analytical approach

6.9.1. Modeling of the Materials

GFRP reinforcing bars – It is well known that GFRP bars in tension have a linear elastic behavior until failure and that they are elastic in nature and do not yield (ACI 440.1R-15). Regarding the compression behavior of GFRP bars, the design guides and recent studies have yet to determine whether their contribution in compression should be taken into consideration as a certain percentage, ignored, or replaced with an equivalent area of concrete (ACI 440.1R-15; CSA S806-12; Zadeh and Nanni 2013; Choo et al., 2006). The results presented herein and in other recent studies (Hadhood et al. 2017, Guérin et al. 2018 a, b) demonstrate that GFRP bars can be considered effective up to the maximum strain of the concrete cover, which governs the failure of GFRP-reinforced elements. The authors therefore decided that the compression contribution of GFRP longitudinal bars should be considered in the analysis.

High-strength concrete – The stress–strain relationship of concrete is influenced by many parameters, such as aggregate type, loading rate, and concrete strength (Popovics 1973). Many studies have proposed different concrete models to accurately represent the behavior of HSC. The main aspect that needs to be considered is HSC's different Young's modulus, the maximum concrete strain, and the descending branch of the HSC for confined and unconfined concrete. The maximum concrete strain considered is 3,000 $\mu\varepsilon$ in ACI 440.1R-15. The following equations were used to model the properties of the HSC:

For the ascending branch:

$$f_c = f_c' \frac{\varepsilon_c}{\varepsilon_c'} \frac{n}{n-1+(\varepsilon_c / \varepsilon_c')^n} \tag{5.5}$$

For the descending branch of the unconfined concrete, the following equation suggested by Theorenfeldt et al. (1987) was used. The equation suggested adding the factor k to accurately predict the descending part, as follows:

$$f_c = f_c' \frac{\varepsilon_c}{\varepsilon_c'} \frac{n}{n-1+(\varepsilon_c / \varepsilon_c')^{nk}}, \quad (5.6)$$

$$n = 0.8 + \frac{f_c'}{17} \text{ (MPa)}, \quad (5.7)$$

$$k = 0.67 + \frac{f_c'}{62} \text{ (MPa)}, \quad (5.8)$$

$$\varepsilon_c' = \frac{f_c'}{E_c} \frac{n}{n-1}, \quad (5.9)$$

$$E_c = 6900 + 3320\sqrt{f_c'}, \quad (5.10)$$

where ε_c is the axial concrete strain at any concrete stress; f_c' is the unconfined concrete's maximum stress at 28 days; ε_c' is the strain when f_c reaches the maximum stress f_c'; n is a curve-fitting factor responsible for the ascending slope; k is the factor for the descending branch's slope; and E_c is the elastic modulus of concrete (ACI 318-14).

Since the value of ε_c' is usually 2,700 $\mu\varepsilon$, the confined model for concrete was used to complete the needed iteration for modeling in order to reach the predetermined maximum compressive strain. The model described by Legeron and Paultre (2003) was used to describe the ascending part of the confined stress–strain model of HSC, specifically, the following equations:

$$f_{cc} = f_{cc}' \left[\frac{k(\varepsilon_{cc} / \varepsilon_{cc}')}{k-1+(\varepsilon_{cc} / \varepsilon_{cc}')^k} \right], \text{ where } \varepsilon_{cc} \le \varepsilon_{cc}' \quad (5.11)$$

$$k = \frac{E_c}{E_c - (f_{cc}' / \varepsilon_{cc}')} \quad (5.12)$$

6.10. DEVELOPMENT OF THE M–ψ RELATIONSHIP

An analytical model was developed using the concepts of strain compatibility and force equilibrium. The model was used to predict the moment–curvature responses of the series G1 and G2 specimens. In order to validate the model, the experimental and analytical moment–curvature was compared. This model used a layer-by-layer approach to sum up the stresses developed in the

cross section due to the concrete and GFRP reinforcing bars. The stresses in the concrete and reinforcing bars were based on the constitutive model described in **Fig. 5.12**. The following assumptions were considered for the analytical model:

- The plane section of the column remains plane under bending, so that the strains in the concrete and reinforcing bars remain linear and proportional to their distance from the neutral axis.
- The stresses at the centroid of each strip are assumed constant throughout its thickness.
- No slippage is assumed between the GFRP reinforcement and surrounding concrete.
- The tensile strength of concrete is neglected.
- The concrete cover is considered as unconfined, while the concrete inside the ties is considered confined.
- The second-order effect is neglected as this study focused on columns with low slenderness ratios.

A numerical program was used to perform the integration analysis of all the cross-section layers. The program uses a certain procedure to obtain the M–ψ response for eccentric columns GFRPRC with a square cross section.

6.10.1. Procedure to Determine Moment and Curvature

In order to calculate the full M–ψ plot for a concrete cross section, the following procedure was repeated for each incremental increase of concrete strain in the top compression fibers. The maximum concrete strain was divided by the desired number of steps (n) to generate many points on the M–ψ plot. The procedure for a single point is summarized below:

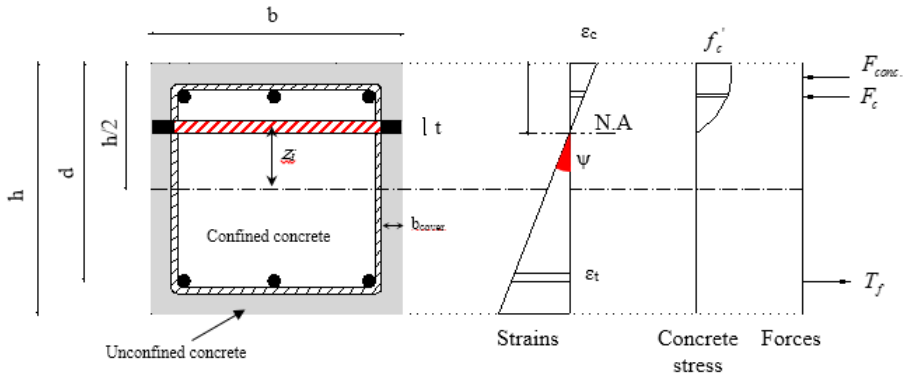

Figure 6-12 – Stress and strain profiles of FRP-RC square cross section.

1. Define the section geometry; concrete cylinder strength; concrete cover; and reinforcing-bar size, mechanical properties, and distribution in the top and bottom layers of the concrete section. Divide the concrete cross section into equal finite numbers of (n) strips and thickness t.
2. Set the target initial eccentricity (e_{in}).
3. Set a value for concrete strain in the extreme top fiber $\left(\varepsilon_1 = \varepsilon_{conc} / i\right)$ and assume a reasonable value for the neutral depth $\left(c_1\right)$.
4. Calculate the area, strain, stress, and force at the center of each strip i, as shown in **Fig. 5.12** (note that A_{ci} and f_{ci} must be calculated for the core and cover segments separately).

$$z_i = i \times t - t/2 \tag{5.13}$$

$$A_{conf} = b\text{-}2b_{cover} \tag{5.14}$$

5. Calculate distances (z_{fi}), area (A_{fi}), strain $\left(\varepsilon_{fi}\right)$, and force ($F_{fi}$) for the top reinforcement.
6. When considering the contribution of FRP bars in compression, the strips at the level of the compressed reinforcing bar should be displaced to ensure accurate modeling and results. For these strips, the strip area and force should be calculated as follows:

$$A_{ci}^{'} = b_i \times t \tag{5.15}$$

$$F_{ci} = [f_{ci} \times A_{ci}^{'}]_{core} + [f_{ci} \times A_{ci}]_{cover} \tag{5.16}$$

7. Compute the summation of all concrete strips and reinforcing bars
8. Satisfy the equilibrium and calculate the moment at the geometrical centroid (M_1), total force (P_1), and the resultant eccentricity of this point (e_1).

$$P_n = P_c - T_f = \sum_{n=1}^{n=t} tbf_i - \varepsilon_{fj} E_f A_f \tag{5.17}$$

$$M_n = M_c \pm M_t = \sum_{n=1}^{n=t} f_i \left(\frac{h}{2} - (n - \frac{t}{2})t\right) \pm \varepsilon_{fj} E_f A_f \tag{5.18}$$

9. Check if $e_1 = e_{in}$. If equal, find ψ_1

$$\psi_1 = \varepsilon_{c1} / c_1 \tag{5.19}$$

Find the successive points (M_2, ψ_2, M_3, ψ_3, M_4, ψ_4, and so on until the number of increments is reached for each point) by increasing ε_{c1} by an increment $\Delta\varepsilon_c$ and assume a reasonable value for

the neutral-axis depth (ε_{c1} and $\Delta\varepsilon_c$ in the model were set to 0.003 and 0.0003, respectively) until reaching ε_{cu}.

6.11. COMPARISON BETWEEN THE ANALYTICAL MODEL AND THE EXPERIMENTAL RESULTS

Figure 5.10 plots the experimental and analytical relationships of the moment–curvature for the four eccentricities. The plots include specimens from series G1 and G2, which had reinforcement ratios of 1%, and 2.5%, respectively. The comparison with analytical approach revealed very good correlation for the ascending branch up to peak load. The analytical model successfully predicted the maximum flexural strength in comparison to the experimental results. Both plots were very consistent for the low eccentricities (80 and 120 mm). As the applied eccentricity increased, the analytical predictions diverged from the experimental results. This is due to the nonlinear behavior of the GFRPRC specimens. At e/h = 0.6, there was clear bilinear behavior representing the flexural behavior of concrete: the concrete resisted the tensile stresses until the maximum tensile stresses were reached. Then, the tensile cracks started to develop, initially resisted by the GFRP bars instead of the concrete. This is well-known behavior for flexural beams and columns loaded at high eccentricities. More research on models considering the change in strain gradient should be undertaken. Overall, the prediction was in good agreement with the experimental results and can be used effectively for estimating the column stiffness at the service- and ultimate-load levels. Moreover, a parametric study could be established to further investigate the influence of reinforcement ratio and concrete strength.

6.11.1. Effect of Reinforcement Ratio and Concrete Strength on the Column Effective Stiffness

Two parameters were analytically investigated to study their effect upon the resultant effective stiffness at the service-load limit. Four different reinforcement ratios (from 1.0% to 4%) and four different concrete strengths were used (70, 90, 110, and 130 MPa) in the analytical study (see **Figs. 5.13 (a), and (b)**). In the case of low eccentricities—0.2h and 0.3h—the difference in the resultant effective stiffness of the column was small. Increasing the reinforcement ratio had a more pronounced effect on the EI/EI_g as the eccentricity increased. It should be noted that the effect of

increasing the reinforcement ratio is expected to increase when the effective stiffness is measured at higher load levels (i.e., ultimate load or peak load). In contrast, increasing the concrete strength insignificantly increased the effective stiffness up to peak load. Thus, it can be concluded that increasing the reinforcement ratio is more effective in enhancing column stiffness than increasing the concrete strength, especially at high levels of eccentricity.

6.11.2. Comparative Study on I_e/I_g

The relative stiffness I_e/I_g of the tested specimens was experimentally determined at the service and ultimate loads. The relative stiffness was determined by calculating the effective stiffness by applying Eq. 5.2 and dividing by EI_g for the uncracked column section. Alternatively, the secant stiffness (EI_{sec}) of each specimen can be determined through the M–ψ relationships at either the ultimate or service load. The ultimate load for all the specimens was defined as 0.48 P_n= $(0.80\times0.60P_n)$. The service load was taken as 0.70 of the ultimate load, as recommended in ACI 318-14. The experimental pattern for the relative stiffness at ultimate load can be described by a second-degree parabolic equation: $y = 3.8x^2 - 4.35x + 1.4$ for series G1 specimens with a reinforcement ratio of 1%, and $y = 2.53x^2 - 3.16x + 1.25$ for series G2 specimens.

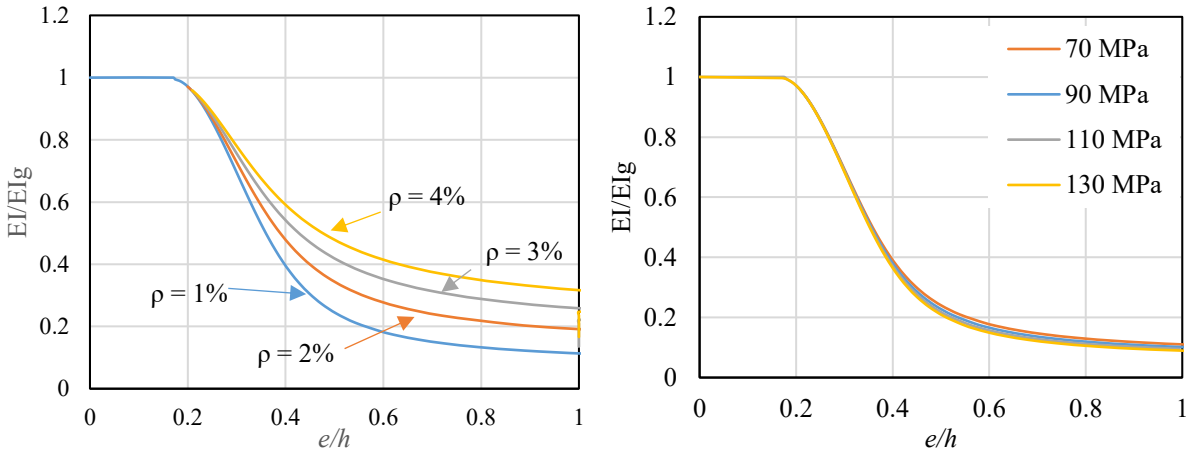

Figure 6-13 – Analytical study showing the effect of changing (a) reinforcement ratio ρ, and (b) concrete strength (f_c') on the relative flexural stiffness of FRPRC members as a function of eccentricity-to-depth ratio.

The experimental results were then compared to equations proposed by Zadeh and Nanni (2017), which included theoretical derivation and general expression for the relative stiffness, and Hadhood et al. (2018), which are described as follows:

$$(I_e / I_g)_{col} = 0.40 + 0.15\frac{E_f}{E_s}, \text{ where } (I_e / I_g)_{col} \le 0.55 \text{ (Zadeh and Nanni, 2017)} \quad (5.20)$$

$$(I_e / I_g)_{beam} = 0.10 + 0.25\frac{E_f}{E_s}, \text{ where } (I_e / I_g)_{beam} \le 0.35 \text{ (Zadeh and Nanni, 2017)} \quad (5.21)$$

$$(I_e / I_g)_{col} = \left(0.5 + 25\rho_f \frac{E_f}{E_s}\right)\left(1 - \frac{e}{h}\right) \text{ (Hadhood et al., 2018)} \quad (5.22)$$

$$(I_e / I_g)_{beam} = \left(0.15 + 25\rho_{f-ten} \frac{E_f}{E_s}\right) \text{ (Hadhood et al., 2018)} \quad (5.23)$$

$$\frac{EI(x)}{E_c I_g} = \left(3 - 2\frac{x}{h}\right)\left(\frac{x}{h}\right)^2 + 3\gamma^2 n_s \rho_{st} \quad (5.24)$$

$$\frac{e(x)}{h} = \frac{EI(x)/E_c I_g}{6\left[\left(\frac{x}{h}\right)^2 - \left(\frac{\gamma+1}{2} - \frac{x}{h}\right)n_f \rho_f\right]} \quad (5.25)$$

where ρ_f is the FRP-reinforcement ratio; ρ_{f-t} is the FRP-reinforcement ratio in tension; ρ_{st} is the steel-reinforcement ratio; E_f is the FRP bar's Young's modulus; E_c is the concrete's Young's modulus; n_s is the steel-bar modular ratio; n_f is the FRP-bar modular ratio; EI_{sec} is the section stiffness; I_g is the gross moment of inertia; I_e is the effective moment of inertia; and γ is the ratio of the distance between the compressive and tensile reinforcement and section height.

Figures 5.14 (a), and (b) compare the experimental results with the above expressions. It should be noted that, at $e/h \geq 0.5$, specimens achieved small nominal loads ($P/P_o < 0.10$ at the service and ultimate loads) and they were, therefore, considered as beams. Other specimens represented columns in this study. The equations proposed by Zadeh and Nanni (2017) were developed to determine the relative stiffness of rectangular FRP-reinforced concrete members (Eqns. 5.20 and 5.21).

Equation 5.20 can be applied to columns with applied eccentricity-to-depth ratios of $0.25 \leq e/h \leq 0.50$. Equation 21 applies to columns with eccentricity-to-depth ratios exceeding 0.50, for which the resultant axial force is actually located outside the section, and the column acts more as a flexural member, since the axial force to applied moment is considered low. In addition, the driven mathematical expressions (Eqns. 24 and 25) proposed by Zadeh and Nanni (2017) were plotted against the experimental results to verify their accuracy. The derived mathematical model was used to measure the effective flexural stiffness at any applied eccentricity at the service-load level. To compare it to ultimate-load level, the relative stiffness was multiplied by 0.7. Moreover, Eqns. 5.22 and 5.23 were proposed by Hadhood et al. (2018) to estimate the effective flexural stiffness of column cross sections reinforced with GFRP bars. The authors of these equations took into consideration the effect of changing the initial eccentricity on the corresponding flexural stiffness of the concrete cross section. As can be seen in **Fig. 5.14**, the equations proposed by Zadeh and Nanni (2017) gave a constant value for section stiffness as the equation doesn't take into account the change in applied eccentricity.

A regression analysis was made with R^2 values to measure the accuracy and compare the relative stiffness measured from the experimental results with the above-mentioned expression at both the service and ultimate loads. The theoretical derivation made by Zadeh and Nanni (2017) had equal R^2 values at the service and ultimate loads of 0.97 and 0.99 for series G1 and G2 specimens, respectively. The general equation proposed by Zadeh and Nanni (2017) had R^2 values of 0.45 and 0.44 at the ultimate- and service-load levels, respectively. The general equation does not consider the effect of change of the applied eccentricity, which resulted in the low accuracy value. The equation proposed by Hadhood et al. (2018) had R^2 values of 0.83 and 0.82 for series G1 specimens and 0.854 and 0.851 for series G2 specimens at the ultimate- and service-load levels, respectively.

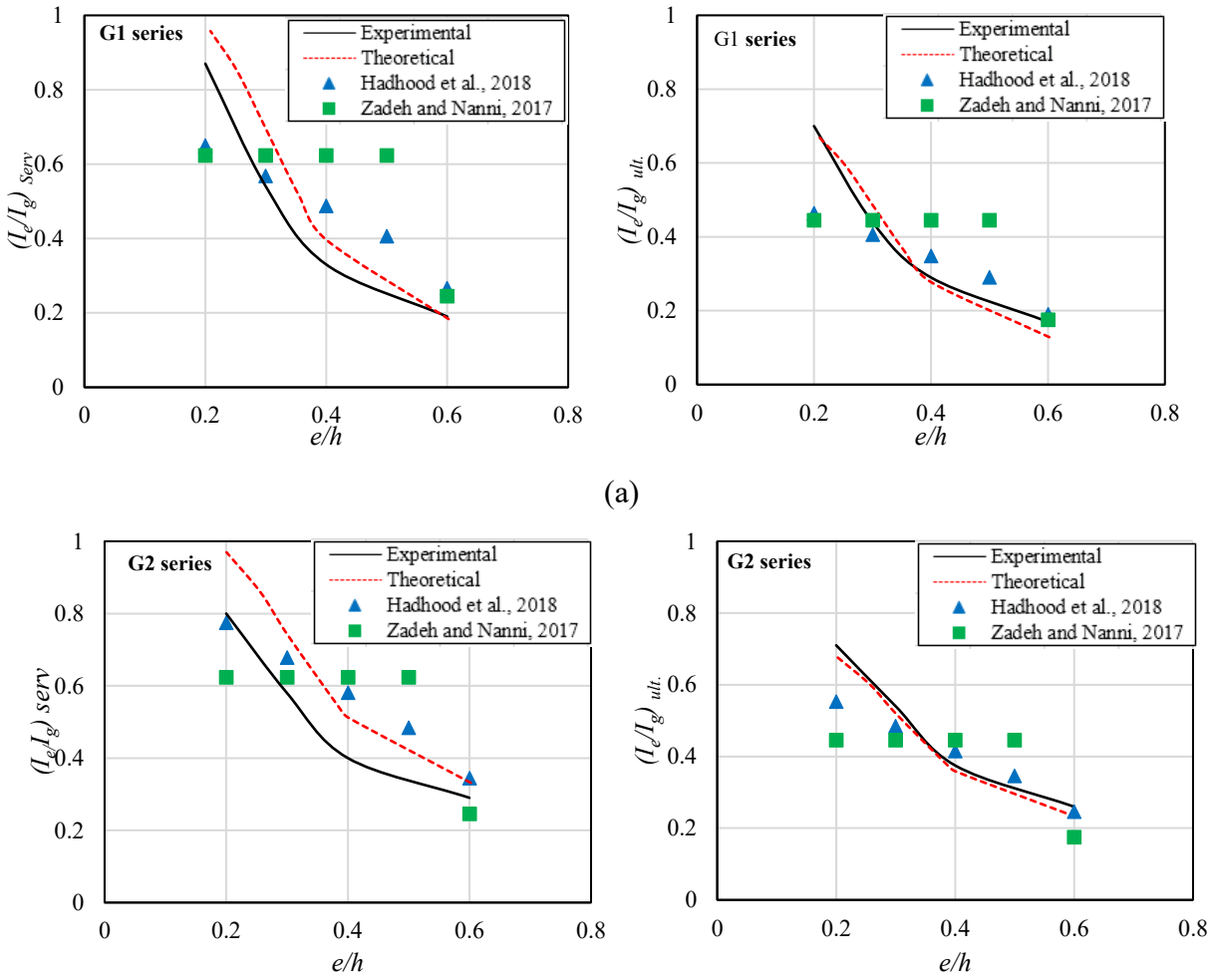

Figure 6-14 – Influence of changing the applied eccentricity and P/P_o on EI/EI_g for series G1 and G2.

6.12. CONCLUSION

This paper presented tests performed to investigate the axial–flexural behavior of full-scale HSC columns with different GFRP reinforcement ratios. The columns were prepared to study the effect of three test parameters: eccentricity-to-depth ratio, GFRP reinforcement ratio (0.5%, 1% and 2.5%), and concrete strength. Theoretical analysis was conducted to develop the moment–curvature behavior, and to estimate the flexural stiffness. Based on the experimental test results and analysis presented in this paper, the following conclusions can be drawn:

1- Increasing the reinforcement ratio had little effect on column strength tested at lower eccentricity-to-depth ratios. The effect was more pronounced for columns tested at high levels of eccentricities as more tensile strains developed in the GFRP bars under tension.
2- All the columns failed due to concrete crushing. No failure of GFRP bars or ties was observed at any of the reinforcement ratios.
3- A minimum reinforcement ratio of 1% for GFRP bars can be used for HSC up to 70 MPa. The minimum reinforcement ratio for compression members cannot be reduced for HSC compared to NSC.
4- The columns with a GFRP reinforcement ratio of 2.5% showed an increase in column strength after reaching the peak load for $e/h > 0.3$. This is due to enhanced concrete-core strength provided by the increase in reinforcing-bar diameter and the reduced bar spacing.
5- The columns tested at $e/h = 0.6$ and higher can be classified as having tension-controlled failures due to the excessive axial and lateral displacements and the wide cracks that developed. The calculated curvature was $0.0109/d$ and $0.0084/d$ for columns G1e240 and G2e240, respectively.
6- The analytical modeling presented herein accurately predicted the M-ψ response of the tested GFRPRC columns.
7- The equation proposed by Hadhood et al. (2018) can accurately predict the effective stiffness for GFRPRC columns made with HSC.

CHAPTER 7 SUMMARY, CONCLUSIONS AND RECOMMENDATIONS

7.1. Summary

The current research addressed the structural performance of the eccentrically loaded Square concrete columns entirely reinforced with FRP bars using high-strength concretes. This research included testing of full-scale specimens under four different levels of eccentricity. The test variables were chosen to examine the glass and basalt FRP rebar efficiency at different load intensities. The experimental results of FRP-RC specimens were analyzed and discussed in a comparison to the reference steel-RC specimens. All specimens measured 400 mm × 400 mm square cross section and 2000 mm height. The experimental results were compared to results of columns with same dimensions made with NSC columns tested by Guérin et al. 2018. Stresses were integrated over the section by adopting the layer-by-layer approach considering proper constitutive models for materials which was used to develop moment-curvature relationships. This research additionally conducted several parametric studies, based on the validated models, to generate sets of **P-M** interaction diagrams and guide charts considering the mechanical properties of the GFRP and Basalt bars provided in the ACI 440.1R (2015). Finally, the flexure stiffness of FRP-RC columns was investigated and discussed in the light of the recommendation provided by the ACI 318 (2014) and recent research. Previous expressions from literature were, therefore, compared with experimental results to reflect the validity and accuracy of using obtained from the experimental database and the analysis of this research. The results of this research work were presented by three articles.

7.2. Conclusions

Based on the experimental and analytical results obtained in this research considering the previous parameters associated with this research program, the following general conclusions are drawn.

7.2.1. Strength, General Behavior and Failure Mode

GFRP

a) Integrating GFRP reinforcement with HSC columns achieved close axial resistance to columns with steel reinforcement for eccentricity to depth ratio of 0.2*h* and 0.6*h*. No appreciable difference was observed in terms of column's strength. The GFRP reinforced columns was more ductile and experienced more lateral and axial deformation when compared to steel reinforced columns under the same eccentricity.

b) As expected, increasing the concrete compressive strength increased the column's axial and flexural strength. Higher tensile strains were developed in the GFRP bars at the peak load levels which increased the axial and flexural strength of HSC columns when compared to NSC columns.

c) Both types of reinforcement (steel and GFRP) showed stable and ductile behavior for the post-peak descending branch. The GFRP reinforced columns have a longer post peak and smaller loss in strength compared to steel reinforced columns for all the tested eccentricities. This is mainly due to the nature of GFRP to sustain higher strains compared to the yielding strain of the steel bars. The steel reinforced columns suffered loss strength ranging from 43% to 67% for eccentricity to depth ratio of 0.3h and 0.6h. GFRP reinforced columns had post-peak losses ranging from 14% to 34% for 0.2h and 0.6h respectively.

d) The range of concrete strain achieved in steel reinforced columns was 2,090 to 3,140 με, while for GFRP reinforced columns was 1,870 to 3,420με.

e) Loading with small to medium eccentricity, 0.2h,0.3h, and 0.4h, the failure of GFRP RC columns failed due to crushing of the concrete cover at the peak load under all the tested eccentricities. Similar failure mode was observed for the steel reinforced counterpart, columns under the same eccentricity levels. For high eccentricity level, *e/h*=0.6, the GFRP reinforced column experienced deep and wide cracks and experienced 30 % increase in lateral deformation compared to the steel reinforced column at the peak load. At the same level of eccentricity to depth ratio, the steel bars on the tensions side reached yielding strain which caused the cracks to grow excessively wide and the columns to exhibit large lateral deflection. Similar failure process and behavior for both GFRP and steel reinforced columns were observed at e = 0.6h.

f) Increasing the reinforcement ratio had little effect on column strength tested at lower eccentricity-to-depth ratios. The effect was more pronounced for columns tested at high levels of eccentricities as more tensile strains developed in the GFRP bars under tension.
g) A minimum reinforcement ratio of 1% for GFRP bars can be used for HSC up to 70 MPa. The minimum reinforcement ratio for compression members cannot be reduced for HSC compared to NSC.
h) The columns with a GFRP reinforcement ratio of 2.5% showed an increase in column strength after reaching the peak load for $e/h > 0.3$. This is due to enhanced concrete-core strength provided by the increase in reinforcing-bar diameter and the reduced bar spacing.
i) The columns tested at $e/h = 0.6$ and higher can be classified as having tension-controlled failures due to the excessive axial and lateral displacements and the wide cracks that developed. The calculated curvature was $0.0109/d$ and $0.0084/d$ for columns G1e240 and G2e240, respectively.

BFRP

Using BFRP reinforcement in HSC columns yielded axial resistance close to that of steel-reinforced columns at eccentricity-to-depth ratios of 0.2h and 0.6h. The difference in strength did not exceed 3%, this is attributed to the yielding of the steel bars in the steel reinforced columns at these eccentricities. While, the compressive strength for BFRP-reinforced columns reinforced were 13% and 22% lower than the steel-reinforced counterparts at 0.3h and 0.4h, respectively.

j) As expected, using HSC allowed the columns to develop higher axial and flexural strengths compared using NSC. Moreover, increased eccentricity and the use of HSC enabled the tensile bars to develop higher tensile strains, which made them more effective.
k) Both types of reinforcement were able to achieve stable and ductile behavior in the pre-peak phase. The BFRP bars developed up to 4,000 με compressive strain, confirming that the BFRP bars were effective in resisting compression until concrete cover crushing.
l) BFRP- and steel-reinforced HSC columns tested under low eccentricity ($0.2h$) failed in compression. Compression–ductile failure was the dominant failure mode of the BFRP- and steel-reinforced concrete specimens tested with an eccentricity of 0.3 and $0.4h$. Due to the excessive deflection, cracking, and large recorded strains in the BFRP bars in the columns tested under high eccentricity ($0.6h$, the failure could be called tension controlled.

m) Using tie spacing of $8d_b$ (half of that specified in ACI 318-14 to account for the difference in moduli of elasticity between the steel and BFRP reinforcement) for the BFRP-reinforced HSC columns provided sufficient lateral support to prevent crushing of the BFRP bars and the concrete core. Also, the concrete core was able to continue withstanding the applied load in the post-peak phase, and the BFRP bars developed maximum compressive strains and tensile strains of 6,700 με 10,900 με.

n) The interaction diagram for the BFRP-reinforced HSC columns tested shows the characteristic "knee" shape found with conventional steel-reinforced concrete columns. The failure envelope of the steel-reinforced concrete specimens was slightly larger than those of the BFRP-reinforced HSC columns.

7.2.2. Flexural Stiffness

GFRP

o) The equation proposed by Hadhood et al. (2018) can accurately predict the effective stiffness for GFRPRC columns made with HSC with ($R^2 = 0.97$) compared to ($R^2 = 0.44$) for both the ultimate- and service-load levels.

BFRP

p) Using the equations proposed by Hadhood et al. (2018) provided more accurate predictions of the effective cross-section stiffness ($R^2 = 0.94$) compared to the Zadeh and Nanni (2017) equations ($R^2 = 0.64$) for both the ultimate- and service-load levels.

7.2.3. Analytical Modelling

GFRP

q) Using layer by layer approach predicted axial and flexural strength values close to the experimental results. Considering the contribution of the GFRP bars in compression resulted in more reliable predictions, while it's advised to replace the area of GFRP bars with concrete in case their contribution is accounted for.

BFRP

r) Using a strip-by-strip approach predicted axial- and flexural-strength values close to the experimental results. Considering the contribution of the BFRP reinforcement in compression resulted in more reliable predictions, while it is advised to replace the BFRP with concrete when the BFRP contribution is ignored.

7.2.4. Parametric Investigations

The parametric study indicates that increasing the concrete strength from 40 to 100 MPa significantly increased the failure envelopes in both scenarios (neglecting or considering the FRP's compression contribution).

7.3. Recommendations for Future Work

Results of the current research consider a promising step toward implementing FRP bars in axially loaded members. Due to lack of research on columns, low elastic modulus, variable mechanical properties among other reasons, GFRP and CFRP contributions are ignored in compression zones of flexural members and beam columns. Additional research on column design is recommended based on the findings of the current study to cover the following points:

- Ultra high-performance concrete has been being well-known in research domains. Investigating the effect of using other types of concrete, such as self-consolidated concrete, light weight concrete, and high-performance concrete, should be investigated more deeply.
- Equivalent stress block parameters and strength reduction factor should be modified to be used for high strength concrete.
- Further investigation needed to establish the minimum required spacing for transverse reinforcement to improve and the ductility of high strength concrete members.

The french version of this section is presented below

Résumé

Le présent projet de recherche porte sur l'étude des performances structurales de poteaux de section carrée, en béton à haute résistance armé entièrement d'armatures en polymère renforcé de fibres

(PRF), sous charges excentrées. Le projet de recherche comprenait des essais sur des spécimens pleine grandeur suivant quatre différents niveaux d'excentricité. Les paramètres d'essais ont été choisis pour examiner l'efficacité des armatures en polymère renforcé de fibres de verre (PRFV) et de fibres de basalte (PRFB) sous différentes intensités de charge. Les résultats expérimentaux des spécimens en béton armé de PRF ont été analysés et discutés en comparaison aux spécimens de référence en béton armé d'acier. Tous les spécimens avaient une section transversale de 400 mm x 400 mm et une hauteur de 2000 mm. Les résultats expérimentaux ont été comparés aux résultats d'essais de poteaux de mêmes dimensions, fabriqués en béton de résistance normale et testés par *Guérin et al. 2018*. L'intégration des contraintes sur la section a été effectuée en adoptant une approche couche par couche, qui prend en compte les modèles constitutifs appropriés des matériaux utilisés, ce qui a permis de développer les relations moment-courbure. De plus, plusieurs études paramétriques basées sur des modèles validés ont été réalisées, afin de générer des diagrammes d'interaction P-M et des guides en prenant en compte les propriétés mécaniques des barres d'armature de PRFV et de PRFB fournies dans l'ACI 440.1R (2015). Enfin, la rigidité en flexion des poteaux en béton armé de PRF a été examinée et discutée à la lumière des recommandations formulées par l'ACI 318 (2014) et des études récentes. Les équations de la littérature ont donc été comparées aux résultats expérimentaux afin de refléter la validité et la précision des résultats de la base de données expérimentale et de l'analyse du présent projet de recherche. Les résultats de ces travaux de recherche ont été publiés dans trois articles.

7.4. Conclusions

Sur la base des résultats expérimentaux et analytiques obtenus dans cette étude et en tenant compte des paramètres précédents associés à ce programme de recherche, les conclusions générales suivantes sont tirées.

7.4.1. Résistance, comportement général et modes de rupture

Armatures de PRFV

a) L'utilisation des armatures en PRFV dans les poteaux en béton à haute résistance a permis d'obtenir une résistance axiale proche des poteaux en béton armé d'acier, pour des excentricités de 0,2 h et 0,6 h. Aucune différence notable n'a été observée du point de vue de

la résistance du poteau. Les poteaux avec armatures en PRFV avaient un comportement plus ductile et présentaient davantage de déformations latérales et axiales que les poteaux avec armatures en acier testés pour les mêmes excentricités.

b) Comme on pouvait s'y attendre, l'augmentation de la résistance à la compression du béton a conduit à l'augmentation de la résistance axiale et en flexion du poteau. Les barres d'armature en PRFV ont présenté des déformations en traction plus élevées au pic de la charge appliquée, ce qui a conduit à une augmentation de la résistance axiale et en flexion des poteaux en béton à haute résistance comparée aux poteaux en béton de résistance normale.

c) Les deux types d'armatures (acier et PRFV) ont montré un comportement stable et ductile pour la réponse post-pic des poteaux. Les poteaux en béton armé de PRFV ont présenté une réponse post-pic supérieure et une perte de résistance inférieure à celle des poteaux avec armatures en acier pour toutes les excentricités considérées. Cela est principalement dû à la nature des barres d'armature de PRFV qui permet de supporter des contraintes plus élevées par rapport aux déformations de plastification des barres d'acier. Les poteaux avec armatures en acier ont subi une perte de résistance allant de 43 % à 67 % pour des excentricités de 0,3 h et de 0,6 h. Les poteaux avec armatures en PRFV ont eu des pertes de résistances post-pic comprises entre 14 % et 34 % pour des excentricités de 0,2 h et 0,6 h respectivement.

d) La plage de déformation du béton dans les poteaux avec armatures en acier variait de 2 090 à 3 140 μdef, alors que pour les poteaux en PRFV, elle variait de 1 870 à 3 420 μdef.

e) Pour les excentricités faibles à moyennes de 0,2 h, 0,3 h et 0,4 h, la rupture des poteaux avec armatures en PRFV était due à l'écrasement du béton, dès l'atteinte de la charge au pic, pour toutes les excentricités appliquées. Un mode de rupture similaire a été observé dans les poteaux avec armatures en acier, pour les mêmes excentricités. Pour des excentricités élevées (e/h = 0,6), le poteau avec armatures en PRFV a présenté des fissures profondes et larges avec une augmentation de la déformation latérale de 30 % dès l'atteinte de la charge maximale, par rapport au poteau avec armatures en acier. Pour cette même excentricité, les barres d'acier du côté en tension ont atteint la déformation de plastification qui a entraîné une augmentation excessive des fissures et une déflexion latérale importante des poteaux. Des modes de rupture et comportement similaires ont été observés dans les poteaux en béton armé de PRFV et d'acier pour une excentricité de 0,6 h.

f) L'augmentation du taux d'armature n'a eu que peu d'effet sur la résistance des poteaux testés pour de petits rapports excentricité/largeur de la section. L'effet de l'augmentation du taux d'armature était plus prononcé dans les poteaux testés à des niveaux d'excentricités élevés, du fait que davantage de contraintes de traction se sont développées dans les barres d'armature en PRFV en tension.

g) Un taux d'armature de PRFV minimum de 1 % peut être utilisé avec du béton de résistance allant jusqu'à 70 MPa. Le taux d'armature minimum pour les membrures en compression ne peut pas être limité pour le béton à haute résistance comparé au béton de résistance normale.

h) Les poteaux ayant un taux d'armature de PRFV de 2,5 % ont présenté une augmentation de résistance après avoir atteint la charge maximale pour $e/h > 0,3$. Ceci est dû à l'augmentation de la résistance du noyau de béton confiné en raison de l'augmentation du diamètre et de la réduction de l'espacement des barres d'armature.

i) Les poteaux testés pour e/h = 0,6 et plus peuvent être classés comme ayant des ruptures en tension en raison des déplacements axiaux et latéraux excessifs et des fissures larges qui se sont développées. La courbure calculée était de 0,010 9/d et de 0,008 4/d pour les poteaux Gle240 et G2e240 respectivement.

Armatures de PRFB

j) L'utilisation d'armatures en PRFB dans les poteaux en béton à haute résistance (BHR) a permis d'obtenir des résistances axiales proches de celle des poteaux avec armatures en acier pour des excentricités de 0,2 h et 0,6 h. La différence de résistance n'excédait pas 3 %, et est due à la plastification des barres d'acier des poteaux en béton armé d'acier, testés sous les mêmes excentricités. De plus, la résistance à la compression des poteaux en béton armé de PRFB était de 13 % et 22 % inférieure à celle de leurs homologues avec armatures en acier pour des excentricités de 0,3 h et 0,4 h, respectivement.

k) Comme on pouvait s'y attendre, l'utilisation du béton à haute résistance a permis aux poteaux de développer des résistances axiales et en flexion supérieures à celles des poteaux en béton de résistance normale. De plus, l'augmentation de l'excentricité et l'utilisation de béton à haute résistance ont permis aux barres d'armature en traction de développer des déformations plus élevées, ce qui les rendait plus efficaces.

l) Les deux types d'armatures ont eu un comportement stable et ductile dans la phase précédant le pic. Les barres d'armature en PRFB ont développé des déformations en compression pouvant atteindre 4 000 μdef, ce qui confirme que les barres d'armature en PRFB ont résisté efficacement à la compression jusqu'à ce l'écrasement du béton.

m) Les poteaux en béton à haute résistance avec armatures en PRFB et en acier testés sous faible excentricité (0,2 h) ont subi une rupture en compression. La rupture ductile en compression était le mode de rupture dominant pour les poteaux en béton armé de PRFB et d'acier testés avec une excentricité de 0,3 et 0,4 h. En raison de la flèche excessive, de la fissuration et des grandes déformations enregistrées dans les barres d'armature en PRFB des poteaux testés avec une excentricité élevée (0,6 h), la rupture de ces poteaux pourrait être qualifiée de rupture en tension.

n) Un espacement des cadres égal à $8d_b$ (la moitié de celui spécifié dans l'ACI 318-14 pour tenir compte de la différence de module d'élasticité entre l'acier et l'armature de PRFB) dans les poteaux en béton à haute résistance avec armatures en PRFB a permis de fournir un support latéral suffisant pour empêcher l'écrasement des barres d'armature de PRFB et du noyau de béton. En outre, le noyau de béton a continué à supporter la charge appliquée dans la phase post-pic et les barres d'armature en PRFB ont développé des déformations en compression et des déformations en traction maximales de 6 700 μdef à 10 900 μdef respectivement.

o) Le diagramme d'interaction des poteaux en béton à haute résistance avec armatures en PRFB testés montre la forme caractéristique du « genou » spécifique aux poteaux conventionnels en béton armé d'acier. L'enveloppe de rupture des poteaux de béton armé d'acier était légèrement supérieure à celle des poteaux en béton à haute résistance avec armatures de PRFB.

7.4.2. Rigidité en flexion

Armatures de PRFV

p) L'équation proposée par Hadhood et al. (2018) peut prédire avec précision la rigidité effective des poteaux en béton armé de PRFV fabriqués avec du béton à haute résistance avec un coefficient de détermination $R^2 = 0,97$ comparé à $R^2 = 0,44$ pour les charges ultimes et de service.

Armatures de PRFB

q) Les équations proposées par Hadhood et al. (2018) ont fourni de meilleures prévisions de la rigidité de la section ($R^2 = 0,94$) comparées aux équations de Zadeh et Nanni (2017) ($R^2 = 0,64$) pour les charges ultimes et de service.

7.4.3. Modélisation analytique

Armatures de PRFV

r) En utilisant une approche couche par couche, les valeurs de la résistance axiale et en flexion calculées étaient proches des résultats expérimentaux. La prise en compte de la contribution des barres d'armature PRFV en compression a conduit à des prévisions plus fiables, même s'il est conseillé de remplacer la zone occupée par les barres d'armature de PRFV par du béton dans le cas où leur contribution serait prise en compte.

Armatures de PRFB

s) L'utilisation d'une approche bande par bande a permis de prédire des valeurs de résistance axiale et en flexion proches des résultats expérimentaux. La prise en compte de la contribution des armatures de PRFB en compression a conduit à des prévisions plus fiables, bien qu'il soit conseillé de remplacer la zone occupée par les armatures de PRFB par du béton lorsque leur contribution est ignorée.

7.4.4. Études paramétriques

L'étude paramétrique a montré que le fait d'augmenter la résistance du béton de 40 à 100 MPa a conduit à l'augmentation considérable des enveloppes de rupture dans les deux cas (négliger ou prendre en compte la contribution des barres d'armature de PRF en compression).

7.5. Recommandations pour les travaux futurs

Les résultats du présent projet de recherche représentent un pas de plus prometteur pour l'utilisation des armatures en PRF dans des éléments sous charges axiales. En raison du manque de données expérimentales sur les poteaux, du faible module d'élasticité, des propriétés mécaniques variables, entre autres raisons, la contribution des armatures en PRFV est ignorée dans les zones en compression des membrures en flexion et dans les poteaux-poutres. Des études supplémentaires

sur le dimensionnement des poteaux sont recommandées sur la base des résultats de la présente étude, pour couvrir les points suivants:

- Le béton à haute résistance est bien connu dans les domaines de la recherche. Il convient d'étudier davantage les effets de l'utilisation d'autres types de béton, tels que le béton autoplaçant, le béton léger et le béton haute performance.
- Les paramètres du bloc rectangulaire équivalent et le facteur de réduction de la résistance doivent être modifiés pour être utilisés avec un béton à haute résistance.
- Des recherches supplémentaires sont nécessaires pour déterminer l'espacement minimal requis pour les armatures transversales afin d'améliorer la ductilité des éléments en béton à haute résistance.

REFERENCES

ACI (American Concrete Institute). (2014). "Building code requirements for structural concrete." ACI 318-14M, Farmington Hills, MI.

ACI (American Concrete Institute). (2015). "Guide for the design and construction of concrete reinforced with FRP bars." ACI 440.1R-15, Farmington Hills, MI.

ACI Committee 318. Building code Requirements for Structural Concrete (ACI 318M-14) and Commentary (ACI318RM-14). Farmington Hills, MI: American Concrete Institute; 2014.

ACI Committee 363 (2010). Report on high-strength concrete (ACI 363R-10), American Concrete Institute, Farmington Hills, Mich.

ACI-ASCE Committee (1997). "High Strength Concrete Columns: State of the Art." Report No. ACI- 441R-96, ACI Structural Journal, 94 (5), 323-335.

Afifi, M. Z., Mohamed, H. M., and Benmokrane, B. (2014). "Axial Capacity of Circular Concrete Columns Reinforced with GFRP Bars and Spirals." *Journal of Composite for Construction*, 18(1), 1–10.

Alsayed, S. H., Al-Salloum, Y. A., Almusallam, T. H., Amjad, M. A. (1999). "Concrete columns reinforced by GFRP rods." Fourth Int. Symp. on Fiber-Reinforced Polymer Reinforcement for Reinforced Concrete Structures, SP-188, C. W. Dolan, S. H. Rizkalla and A. Nanni, eds., American Concrete Institute, Farmington Hills, MI, 103–112.

American Association of State Highway and Transportation Officials (AASHTO). (2009). *AASHTO LRFD bridge design guide specifications for GFRP-reinforced concrete bridge decks and traffic railings*, 1st Ed., AASHTO, Washington, D.C.

American Association of State Highway and Transportation Officials (AASHTO). (2019). *AASHTO LRFD bridge design guide specifications for GFRP reinforced concrete*, 2nd Ed., AASHTO, Washington, D.C.

ASCE. (2017). "Bridges." Infrastructure Report card: A comprehensive assessment of America's infrastructure, Reston, VA, 30–35.

ASTM A615/A615M-14, (2014). "Standard Specifcation for Deformed and Plain Carbon-Steel Bars for Concrete Reinforcement," ASTM International, West Conshohocken, PA.

ASTM C39/C39M-12, (2012) . "Standard Test Method for Compressive Strength of Cylindrical Concrete Specimens, " American Society for Testing and Materials, West Conshohocken, PA, 2012

ASTM D695-15, (2015). "Standard Test Method for Compressive Properties of Rigid Plastics", ASTM International, West Conshohocken, PA.

ASTM D7205/D7205M-06(11), (2011). "Standard Test Method for Tensile Properties of Fiber Reinforced Polymer Matrix Composite Bars," ASTM International, West Conshohocken, PA.

Carrasquillo, R.L., Nilson, A. H., and Slate, F.O. (1981). "Properties of High Strength Concrete Subject to Short-Term Loads. " ACI Structural Journal, (78) 3, 179-186.

Choo, C. C., Harik, I. E., and Gesund, H. (2006a). "Minimum reinforcement ratio for fiber-reinforced polymer reinforced concrete rectangular columns." *ACI Structural Journal*, 103(3), 460–466.

Choo, C. C.; Harik, I. E.; and Gesund, H., (2006b), "Strength of Rectangular Concrete Columns Reinforced with Fiber-Reinforced Polymer Bars," *ACI Structural Journal*, 103(3), 452-459.

Collins, M. P., Mitchell, D., and MacGregor, J. G. (1993). "Structural design considerations for high-strength concrete." Concrete International, 15(5), 27–34.

CSA (Canadian Standards Association). (2010). “Specification for fibre- reinforced polymers.” CAN/CSA S807-10, Rexdale, ON, Canada.

CSA (Canadian Standards Association). (2012). “Design and construction of building structures with fibre reinforced polymers.” CAN/CSA S806-12, Rexdale, ON, Canada.

CSA (Canadian Standards Association). (2014a). “Design of concrete structures.” CAN/CSA A23.3-14, Rexdale, ON, Canada.

CSA (Canadian Standards Association). (2014b). “Canadian Highway Bridge Design Code.” CAN/CSA S6-14, Rexdale, ON, Canada.

CSA (Canadian Standards Association). (2019). “Canadian Highway Bridge Design Code.” CAN/CSA S6-19, Rexdale, ON, Canada.

De Luca, A., Matta, F., and Nanni, A. (2010). “Behavior of full-scale GFRP reinforced concrete columns under axial load.” ACI Structural Journal, 107(5), 589–596.

Dolan, C. W., and LaFraugh, R. W. (1993). "High Strength Concrete in the Precast Concrete Industry," *PCI Journal*, 38(3), 16-19.

Ehsani, M. R. (1993) “Glass-Fiber Reinforcing Bars,” Alternative Materials for the einforcement and Pre- stressing of Concrete, J. L. Clarke, Blackie Academic & Professional, London, pp. 35-54.

Mallick, P. K., 1988, Fiber Reinforced Composites, Materials, Manufacturing, and Design, Marcell Dekker, Inc., New York, 469 pp.

Sonobe, Y.; Fukuyama, H.; Okamoto, T.; Kani, N.; Ki- mura, K.; Kobatashi, K.; Masuda, Y.; Matsuzaki, Y.; Mochizuki, S.; Nagasaka, T.; Shimizu, A.; Tanano, H.; Tanigaki, M.; and Teshigawara, M. (1997b). “Design Guidelines of FRP Reinforced Concrete Building Struc- tures,” ASCE Journal of Composites for Construction, V. 1, No. 3, pp. 90-115.

Wu, W. P., 1990, “Thermomechanical Properties of Fi- ber Reinforced Plastic (FRP) Bars,” PhD dissertation, West Virginia University, Morgantown, W.Va., 292 pp.

El Refai, A., Ammar, M.-A., and Masmoudi, R. (2015). "Bond Performance of Basalt Fiber-Reinforced Polymer Bars to Concrete." *Journal of Composites for Construction*, 19(3), 04014050.

Elchalakani M., Ma G., "Tests of glass fibre-reinforced polymer rectangular concrete columns subjected to concentric and eccentric axial loading", Eng. Struct. 151 (2017), 93–104.

Elgabbas, F., Ahmed, E. A., and Benmokrane, B. (2015). "Physical and mechanical characteristics of new basalt-FRP bars for reinforcing concrete structures." *Construction and Building Materials*, Elsevier Ltd, 95, 623–635.

Elgabbas, F., Ahmed, E. A., and Benmokrane, B. (2016). "Experimental Testing of Concrete Bridge-Deck Slabs Reinforced with Basalt-FRP Reinforcing Bars under Concentrated Loads." *Journal of Bridge Engineering*, 21(7), 04016029.

El-Nemr, A.; Ahmed, E. A.; and Benmokrane, B., 2013, "Flexural Behavior and Serviceability of Normal- and High-Strength Concrete Beams Reinforced with Glass Fiber-Reinforced Polymer Bars," *ACI Structural Journal*, 110(6), 1077-1087.

Fakharifar, M., Dalvand, A., Sharbatdar, M.K., Chen, G., and Sneed, L. (2016). "Innovative hybrid reinforcement constituting conventional longitudinal steel and FRP stirrups for improved seismic strength and ductility of RC structures." *Frontiers of Structural and Civil Engineering*, 10(1), 44-62.

Fan, X., and Zhang, M. (2016). "Behaviour of inorganic polymer concrete columns reinforced with basalt FRP bars under eccentric compression: An experimental study." *Composites Part B: Engineering*, Elsevier Ltd, 104, 44–56.

Fan, X., Zhang, M. "Behaviour of inorganic polymer concrete columns reinforced with basalt FRP bars under eccentric compression: an experimental study", Compos. B Eng. 104 (2016) 44–56

Foster, S. J. (2001). "On Behavior of High-Strength Concrete Columns : Cover Spallling, Steel

Fibers, and Ductility." ACI Structural Journal, 98(4), 583–589.

Gribniak, V., Arnautov, A. K., Kaklauskas, G., Tamulenas, V., Timinskas, E., and Sokolov, A. (2015). "Investigation on application of basalt materials as reinforcement for flexural elements of concrete bridges." *The Baltic Journal of Road and Bridge Engineering*, 10(3), 201–206.

Guérin, M., Mohamed, H. M., Benmokrane, B., Nanni, A., and Shield, C. K. (2018a). "Eccentric Behavior of Full-Scale Reinforced Concrete Columns with Glass Fiber-Reinforced Polymer Bars and Ties." *ACI Structural Journal*, 115(2), 489–500.

Guérin, M., Mohamed, H. M., Benmokrane, B., Shield, C. K, and Nanni, A. (2018b). "Effect of glass Fiber-Reinforced Polymer Reinforcement Ratio on Axial-Flexural Strength of Reinforced Concrete Columns." *ACI Structural Journal*, 115(4), 1049–1061.

Hadhood, A., Mohamed, H. M., and Benmokrane, B. (2016a). "Axial Load–Moment Interaction Diagram of Circular Concrete Columns Reinforced with CFRP Bars and Spirals: Experimental and Theoretical Investigations." Journal of Composites for Construction, 21(2), 1-12.

Hadhood, A., Mohamed, H. M., and Benmokrane, B. (2016b). "Experimental Study of Circular High-Strength Concrete Columns Reinforced with GFRP Bars and Spirals under Concentric and Eccentric Loading." Journal of Composites for Construction, 21(2), 1-12.

Hadhood, A., Mohamed, H. M., and Benmokrane, B. (2017a). "Strength of circular HSC columns reinforced internally with carbon-fiber-reinforced polymer bars under axial and eccentric loads." *Construction and Building Materials*, Elsevier Ltd, 141, 366–378.

Hadhood, A., Mohamed, H. M., and Benmokrane, B. (2017b). "Failure envelope of circular concrete columns reinforced with glass fiber-reinforced polymer bars and spirals." *ACI Structural Journal*, 114(6), 1417–1428.

Hadhood, A., Mohamed, H. M., and Benmokrane, B. (2018). "Flexural Stiffness of GFRP- and CFRP-RC Circular Members under Eccentric Loads Based on Experimental and Curvature Analysis." *ACI Structural Journal*, 115(4), 1185-1198.

Hadi, M. N. S. and Youssef, J. (2016). “Experimental investigation of GFRP-reinforced and GFRP-encased square concrete specimens under axial and eccentric load, and four-point bending test.” J. Compos. Constr., ASCE, 20(5), 04016020.

Hadi, M. N. S., Hasan, H. A., and Sheikh, M. N. (2017). “Experimental Investigation of circular igh-Strength Concrete Columns Reinforced with Glass Fiber-Reinforced Polymer ars and Helices under Different Loading Conditions.” Journal of Composites for onstruction, 21(4),1-13.

Hadi, M. N. S., Karim, H., and Sheikh, M. N. (2016). “Experimental Investigations on Circular Concrete Columns Reinforced with GFRP Bars and Helices under Different Loading Conditions.” J. Compos. Constr., ASCE; 20(4). 10.1061

Hales, T. A., Pantelides, C. P., Asce, M., and Reaveley, L. D. (2016). “Experimental Evaluation of Slender High-Strength Concrete Columns with GFRP and Hybrid Reinforcement.” Journal of Composites for Construction, 20(6),1-10.

Issa, M. S., Metwally, I. M., E. S. N. (2011). “Structural Performance of Eccentrically Loaded GFRP Reinforced Concrete Columns.” International Journal of Civil and Structural Engineering, 2(1), 395–406.

Kaar, P. H., Hanson, N. W., and Capell, H. T. (1977). ‘‘Stress-strain characteristics of high-strength concrete.’’ Research and Development Bulletin RD051.01D, Portland Cement Association, Skokie, Ill.

Kamakshi, S., and Vinu, S.K. (2018). “Structural Behavior of Hybrid Reinforced Concrete Exterior Beam Column Joint.” *Applied Mechanics and Materials*, 877, 254-263.

Karim, H., Sheikh, M. N., and Hadi, M. N. S. (2016). “Axial load-axial deformation behaviour of circular concrete columns reinforced with GFRP bars and helices.” Constr. and Build. Mat., Elsevier, 112, 1147-1157.

Karim, H., Sheikh, M. N., and Hadi, M. N. S. (2017a). “Load and Moment Interaction Diagram for Circular Concrete Columns Reinforced with GFRP Bars and GFRP Helices.” J. Compos. Constr., ASCE; 21(1).

Karim, H., Sheikh, M. N., and Hadi, M. N. S. (2017b). “Longitudinal Reinforcement Limits for Fiber-Reinforced Polymer Reinforced Concrete Members.” ACI Struct. J., 114(3), 687- 696.

Khorramian, K., Sadeghian P., “Experimental and analytical behavior of short concrete columns reinforced with GFRP bars under eccentric loading”, Eng. Struct. 151 (2017), 761–773.

Lee, J. H., and Son, H. S. (2000). “Failure and strength of high-strength concrete columns subjected to eccentric loads.” ACI Structural Journal, 97(1), 75–85.

Leite, L., Bonet, J. L., Pallares, L., Miguel, P. F., and Fernandez-Prada, M. A. (2013). Experimental research on high strength concrete slender columns subjected to compression and niaxial bending with unequal eccentricities at the ends.” Eng. Struct., 48, 220–232.

Mahroug, M. E. M., Ashour, A. F., and Lam, D. (2014). “Experimental response and code modelling of continuous concrete slabs reinforced with BFRP bars.” *Composite Structures*, Elsevier Ltd, 107, 664–674.

Mallick, P. K., (1988), “Fiber Reinforced Composites, Materials, Manufacturing, and Design, Marcell Dekker”, Inc., New York, 469 pp. Sonobe,

Maranan, G., Manalo, A., Benmokrane, B., Karunasena, W., Mendis, P.,” Behavior of concentrically loaded geopolymer-concrete circular columns reinforced longitudinally and transversely with GFRP bars”, Eng. Struct. 117 (2016) 422– 436

Mirza, S., Ali ,M.S. (2017). “ Infrastructure crisis — a proposed national infrastructure policy for Canada.” *Canadian Journal of Civil Engineering*, 44(7), 539-548.

Mohamed, H. M., Afifi, M. Z., and Benmokrane, B. (2014). “Performance Evaluation of

Concrete Columns Reinforced Longitudinally with FRP Bars and Confined with FRP Hoops and Spirals under Axial Load." Journal of Bridge Engineering, 19(7), 1-12.

Mokhtarzadeh, A., and French, C. (2000). "Mechanical Properties of High- Strength Concrete with Consideration for Precast Applications," *ACI Materials Journal*, 97(2), 136-147

Naaman, A. E., and Jeong, S. M., 1995, "Structural Ductility of Concrete Beams Prestressed with FRP Tendons," Proceedings of the 2nd International RILEM Symposium on Non Metallic (FRP) Reinforcement for Concrete Structures, RILEM, Bagneux, France, pp. 379-386.

Nanni, A.; De Luca, A.; and Jawaheri Zadeh, H., 2014, Reinforced Concrete with FRP Bars: Mechanics and Design, CRC Press, Boca Raton, FL, 384 pp.

Ovitigala, T., Ibrahim, M. A., and Issa, M. A. (2016). "Serviceability and ultimate load behavior of concrete beams reinforced with basalt fiber-reinforced polymer bars." *ACI Structural Journal*, 113(4), 757–768.

Palmieri, A., Matthys, S., and Tierens, M. (2009). Basalt fibers: Mechanical properties and applications for concrete structures, Taylor and Francis, London, 165–169.

Pantelides, C. P., Gibbons, M. E., and Reaveley, L. D. (2013). "Axial load behavior of concrete columns confined with GFRP spirals." Journal of Composites for Construction, 17(3), 305–313.

Popovics,S. (1973). "A Numerical Approach to the Complete Stress-Strain Curve of Concrete." *Cement and Concrete Research Journal*, 3(5), 583-599.

Pultrall (2017). www.pultrall.com.

Shield, C.; Galambos, T.; and Gulbrandsen, P., 2011, "On the History and Reliability of the Flexural Strength of FRP Reinforced Concrete Members in ACI 440.1R," Proceedings of the 10th International Symposium on Fiber-Reinforced Polymer Reinforcement for Concrete Structures (FRPRCS-10), SP-275, R. Sen, R. Seracino, C. Shield, and W. Gold, eds., American Concrete Institute, Farmington Hills, MI, 18 pp.

Sim, K., Park, C., and Moon, D. Y. (2005). “Characteristics of basalt fiber as a strengthening material for concrete structures.” *Composites Part B: Engineering*, Elsevier Ltd,, 36(6–7), 504–512

Smadi, Mohammed M., Slate, Floyd O. and Nilson, Arthur H. (1987), “Shrinkage and creep of high, medium, and low strength concretes, including overloads.” *ACI Materials Journal*, 84(3), 224-234.

Sun, L., Wei, M., Zhang, N. ,“Experimental study on the behavior of GFRP reinforced concrete columns under eccentric axial load”, Constr. Build. Mater. 152 (2017) 214–225.

Thorenfeldt, E., Tomaszewicz, A., and Jensen, J. J. (1987). “Mechanical properties of high strength concrete and application to design.” Proceedings of the Symposium: Utilization of High-Strength Concrete, Tapir, Trondheim, Norway, 149–159.

Tobbi, H., Farghaly, A. S., and Benmokrane, B. (2014). “Behavior of concentrically loaded fiber-reinforced polymer reinforced concrete columns with varying reinforcement types and ratios.” *ACI Structural Journal*, 111(2), 375–385.

Tomlinson, D., and Fam, A. (2015). “Performance of Concrete Beams Reinforced with Basalt FRP for Flexure and Shear.” *Journal of Composites for Construction*, 19(2), 04014036.

TUF-BAR Canada (2017). https://www.tuf-bar.com/

Wei, B., Cao, H., and Song, S. (2010). “Environmental resistance and mechanical performance of basalt and glass fibers.” J. Mater. Sci. Eng. Part A, 527(18–19), 4708–4715.

Whittaker, A. S. (2012). "CIE 525: Concrete Design Class Notes."University at Buffalo, NY.

Wight, J. K., and MacGregor, J. G. (2009). "Reinforced concrete: Mechanics and design (5th edition)." Pearson Prentice Hall, Upper Saddle River, NJ.

Wu, Z., Wang, X., Iwashita, K., Sasaki, T., and Hamaguchi, Y. (2010). “Tensile fatigue behavior ofFRP and hybrid FRP sheets.” *Composites Part B: Engineering*, Elsevier Ltd,

41(5), 396–402.

Xue, W., Hu, X., and Fang, Z. (2014). “Experimental studies of GFRP re- inforced concrete columns under static eccentric loading.” Proc., 7th Int. Conf. on FRP Composites in Civil Engineering (CICE 2014), International Institute for FRP in Construction, Vancouver, Canada.

Xue, W., Peng, F., Fang, Z., “Behavior and design of slender rectangular concrete columns longitudinally reinforced with fiber-reinforced polymer bars”, ACI Struct. J. 115 (2) (2018) 311–322

Yost, J. R.; Gross, S. P.; and Dinehart, D. W., 2003, “Effective Moment of Inertia for Glass Fiber-Reinforced Polymer-Reinforced Concrete Beams,” *ACI Structural Journal*, 100(6), 732-739.

Zadeh, H. J., and Nanni, A. (2013). “Design of RC Columns Using Glass FRP Reinforcement.” Journal of Composites for Construction, 17(3), 294–304.

Zadeh, H. J., and Nanni, A., 2017, “Flexural Stiffness and Second Order Effects in Fiber-Reinforced Polymer-Reinforced Concrete Frames,” *ACI Structural Journal*, 114(2), 533-544.